SILICOFCM

Project Title: *In Silico* trials for drug tracing the effects of sarcomeric protein mutations leading to familial cardiomyopathy

Project acronym: SILICOFCM

Grant Agreement number: 777204

Coordinating Institution:
Bioengineering Research and Development Center BioIRC doo Kragujevac, BIOIRC

Start date: 1st June 2018

Duration: 42 months

WP number, Deliverable number and Title	**WP5** Integration of modelling and simulation platform **D5.2** Software: Upgrade FE simulation
Related Task	**Task 5.2** - Upgrade FE biomechanical simulation
Lead Beneficiary	BSC
Deliverable Type	Report
Distribution Level	Public
Document version	v.1.0
Contractual Date of Delivery	31/05/2019
Actual Date of Delivery	31/05/2019

Authors	Jazmin Aguado-Sierra (BSC), Mariano Vázquez (BSC), Miljan Milosevic (BioIRC), Vladimir Geroski (BioIRC), Milos Kojic (BioIRC), Nenad Filipovic (BioIRC)
Contributors	Smiljana Djorovic (BioIRC)
Reviewers	Boban Stojanovic (BioIRC), Nikolaos Tachos (UOI)

This project has received funding from the European Union's Horizon 2020 research and innovation programme under grant agreement No 777204

Version history

Version	Description	Date of completion
0.1	ToC preparation (BSC, BioIRC)	03/05/2019
0.2	BSC first draft (BSC)	13/05/2019
0.3	Restructuring & section update (UOI)	14/05/2019
0.4	BSC second draft	15/05/2019
0.5	BioIRC – draft version	21/05/2019
0.6	Sections redistribution (BSC, BioIRC)	28/05/2019
0.7	BSC and BioIRC – final revision and refinement	29/05/2019
0.1	Final document – submission at the EC portal	31/05/2019

Disclaimer

Executive summary

Modelling the heartbeat is a highly complex task that involves several scales and different tightly coupled problems. A large number of spatial orders of magnitude are linked, from the microscopic cell arrangement into a volumetric description, to the macroscopic shape of the cardiac chambers. In the same way, several temporal scales coexist, from the fast intracellular chemical reactions to the long term remodeling of the heart.

The activity involves the work on the preparation of the Finite Element Analysis codes, Alya and PAK to habilitate the coupling of the excitation-contraction model into a full biventricular human heart simulation. Deep discussions and agreements have been made in respect to the coupling of different codes:

1. A direct coupling of MUSICO with Alya and PAK will remain a big challenge, given the multi-scale nature of the two different codes, therefore the approach to such challenge will be to create a reduced version of MUSICO that can capture the required myofilament dynamics, using the parameterisation of a single run of MUSICO.
2. The desired coupling method remains in discussions, namely, where each code will reside and the communication protocols between them.

Alya has two different excitation-contraction-coupling models already implemented, namely the model published by Hunter et al. [1], and the one published by Land et al. in [2]. The relevance of this, simply resides on the already-existing ability to create tightly coupled simulations of electro-mechanics of the ventricles in highly efficient, manner using high performance computing resources.

The work performed to upgrade the finite element simulations using Alya within the initial months of the project included the programming of appropriate boundary conditions, since one of the most important aspects of biomechanic simulations are the setup of the appropriate boundary conditions required. Mechanic simulations are highly dependent on the boundary conditions. They determine the overall motion of the heart. The most important boundary conditions are:

Pericardium:

It modulates the ventricular motion. The pericardial boundary condition within our simulations is represented as dashpots throughout the ventricular walls. The existence of the atria and great vessels generally produce better results regarding the mechanical boundary conditions because the furthest we constrain the motion, the less artificial effects are seen in the heart, however this is generally non feasible to acquire from clinical MRI protocols.

Hemodynamic boundary conditions:

The heart exerts it's motion against the flow of blood through the arteries, therefore appropriate hemodynamic boundary conditions are necessary to reproduce a physiological heart function. A ventricular pressure curve can be used as a boundary condition to the overall mechanics problem, on an uni-directional boundary condition approach to model a heart beat. This technique will rely on a non-invasive approach for the estimation of intraventricular pressure both for RV and LV, which is not plausible to obtain from patients. In any case an arterial hemodynamics model is required, either 0D or 1D that has to be parameterised for each ventricle.

We are currently implementing a 1D model of arterial circulation within our code, Alya to provide the appropriate patient-specific boundary conditions required by the mechanics model.

Future work involves the coupling of the reduced MUSICO model to Alya, the validation of heart full organ simulations along with the appropriate hemodynamic boundary conditions to the patient-specific data.

In these initial months of the project, the main upgrade of the PAK software is based on the original formulation of the Composite smeared finite element model (CSFEM) [3-6] and its generalization to include electrophysiology and ionic transport in biological tissue [7]. Cell internal ionic transport is calculated uses the smeared concept for physical fields, while the Ionic cell membrane currents and Ca^{+} concentration is based on the framework given in [8,9]. A 1D FE element model for Purkinje network in heart ventricles is implemented, while the smeared formulation and accuracy of the CSFEM is currently tested and verified on 2D examples of small samples of the heart wall tissue. As in Alya, the PAK software is upgraded with the model for coupling of electrophysiology and muscle mechanics according to Hunter et al. [1]. The in-house interface software CAD for pre- and post-processing is upgraded to facilitate all new features listed above.

We are using Alya and PAK in parallel due the following reasons:

- Two groups of developers of computational methods and software have been working over decades with internationally recognized achievements.
- Alya and PAK have their own specificities (Alya has been used for heart modeling with original and verified procedures; while, recently developed smeared models implemented in PAK offer a new concept of modeling electrophysiology, drug transport and electromechanical coupling).
- The models implemented in Alya and PAK will be compared with respect to produced results, which will be important for verification of accuracy and ultimate implementation in clinics.

Table of Contents

List of Figures

List of Tables

List of Abbreviations

Abbreviation	Explanation
API	application program interface
B.C.	boundary conditions
REST	representational state transfer
HPC	high performance computing
EP	electrophysiology
CSM	computational solid mechanics
CFD	computational fluid mechanics
FEM	finite element method
FSI	fluid structure interaction
PDEs	partial differential equations
DTI	diffusion tensor imaging
CAD	computer aided design
ODE	ordinary differential equation
CSFE	composite smeared finite element
CCFE	composite cable finite element

1. Introduction

Although experimental research is essential to improve diagnosis and treatment techniques, computational tools are gradually gaining importance. Biomechanical simulations provide a powerful tool to understand heart function and its behaviour under congenital and acquired pathologies. Besides this, and as happens in other disciplines, simulations can become a key tool in designing surgical procedures, techniques, or devices. However, modelling the beating heart and its pumping action is a highly complex task. Cardiac function involves a considerable range of spatial scales and different tightly coupled multi-physics problems. Several orders of magnitude are linked, from the microscopic cell arrangement into a volumetric arrangement, to the macroscopic shape of the cardiac chambers. Also, different types of physical problems are involved. In the muscle, the electrical stimuli propagates through the cardiac myocytes causing the cardiac muscle contraction, which in turn exerts work upon the blood inside the cavities. Therefore, from the computational mechanics standpoint, the heartbeat is a tightly coupled fluid-electro-mechanical problem.

Within the next parts of the deliverable, a full description of the fluid-electro-mechanical problem of the cardiac function will be described, along with the upgrades and developments of the last year on the software Alya, the in-house tool employed by BSC.

A detailed description of upgrades and developments in software PAK, the in-house tool developed by BioIRC, will be also provided below.

Two main studies to create patient-specific applications scenarios have been developed:

1. Multi-modal ventricular tachycardia analysis: Towards the accurate parameterisation of predictive high performance computing (HPC) electrophysiological computational models.
2. Fluid-electro-mechanical simulations of the human heart using supercomputers.

These patient-specific studies will be described in the following parts of this deliverable, with the specific connection towards the upgrading of finite element computer simulations to create accurate simulations for clinical requirements for hypertrophic cardiomyopathy, patient-specific scenarios. Some of this work includes the verification of the Code Alya for each physics problem involved.

2. Alya

Alya is the Barcelona supercomputing center (BSC) in-house tool used in this project to solve cardiac electro-mechanics models. This software is designed from scratch to run efficiently in high performance computers, with a tested scalability up to 100.000 cores [10, 11, 12, 13, 14].

The code is programmed in a modular way, with a kernel in charge of generic input/output subroutines, solvers, mathematical functions and services like parallelisation or other complementary tools. Then, there are several modules, allowing to solve a wide range of coupled problems such as radiation, compressible and incompressible fluids, excitable media and solid mechanics. The software is written in Fortran 90/95. The time dependent partial differential equations (PDEs) are solved using, mainly, finite element method (FEM), but finite volumes can also be used for some problems. The platform is designed to be multiphysics and flexible for coding and running in high performance computing (HPC) machines.

To model the heart, the problem is divided into three main coupled physics: electrophysiology, solid mechanics and fluid dynamics as shown in Figure 1.

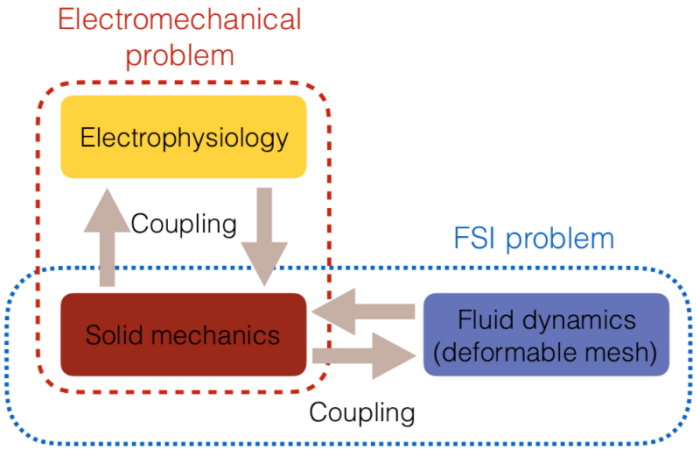

Fig. 1. A three physics problem.

The system can be decomposed in two bidirectionally coupled problems: the electro-mechanical and the fluid- mechanical one. These two problems can be decomposed in sub-problems leading to three systems of equations to solve: electrophysiology, solid mechanics, and fluid mechanics in deformable mesh.

2.1. Programming framework

Alya is prepared to run in a multi-code environment. With a built-in library, our simulation tool can be coupled with other modelling software, or with other(s) Alya instance(s). Generally a multi-code approach is used. Two Alya instances are coupled to solve the fluid-electro-mechanical model, splitting the whole domain in two parts: the fluid sub-problem (blood) and the solid sub-problem (tissue). Each part is solved in one of the instances of the code. Each instance works in a sandbox manner, being completely independent from the other, with their own input configuration and mesh files. Both instances communicates with a black-box approach, knowing only the coupling points and the variables to be transferred. **This approach is the one that will be employed with the reduced MUSICO software to be coupled within SILICOFCM.**

The fluid-electro-mechanical problem is solved in a multi-code approach. The most integrative cases solved up until now are the fluid-electromechanical cases. As said before, this multiphysics problem can be naturally decomposed in two sub-problems: solid and fluid. Using the multi-code approach available in the simulation tool, we can distribute the involved physics, depending on the sub-problem where they are being solved. With this approach, the solid domain runs in one Alya instance, computing the electrophysiology (EP) model and the computational solid mechanics (CSM) equations under the same mesh. The fluid domain runs in another instance of Alya computing the ALE deformable domain and the computational fluid dynamics (CFD) (detailed in Section 5) problem, in another mesh. Both codes communicate through a set of integrated adhoc Message Passing Interface (MPI) subroutines in specific coupling points.

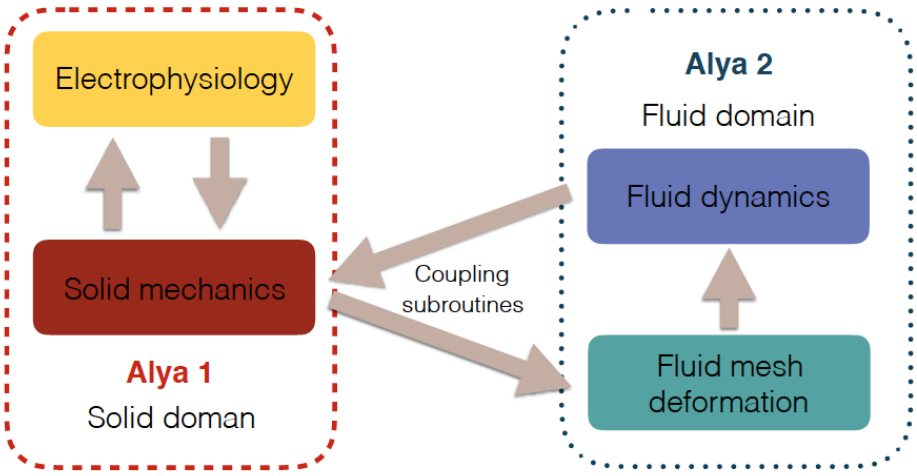

Fig. 2. Alya Framework. Scheme of the multi-code implementation solving the EP and CSM in one Alya instance and another instance solving the ALE and CFD problems in another mesh.

This coupled multi-physics problem is then solved in a staggered way. Each Alya instance solves two problems: on one side, electrophysiology and tissue mechanics; and on the other side, fluid mechanics and mesh deformation. In turn and for each iteration, each of the four physical problems is solved independently. This strategy has its benefits and drawbacks. Among the benefits is its flexibility, because each physical problem can be programmed independently of the other, with smaller problem matrices and its own best-suited solution strategy, allowing to solve the problems in a standalone way if required or adding more and more problems to solve. The drawback is that the coupling strategy must be robust and efficient enough to take real profit of the advantages. The efficiency issue is important not only from the algorithmic viewpoint but also from the parallel implementation one, especially when the two instances are coupled. In this work we show at what extent these drawbacks are overcame.

Domain partition and communication points: Both of the multicode approach sub-problems are potentially very large, requiring in turn parallel runs. Each sub-problem is then partitioned using a mesh partitioner such as METIS [15] and distributed to many MPI parallel threads, every thread with its corresponding sub-domain. If both sub-problems are parallelized, then an efficient MPI point-to-point communication scheme is required for the interface surface Γ_c,

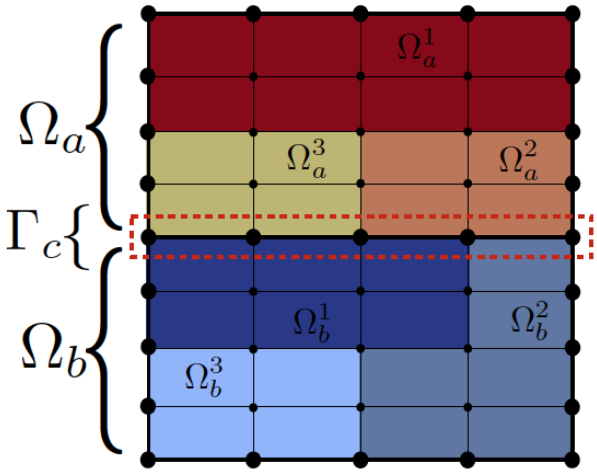

Fig. 3. Physical sub-problems. Ω_a and Ω_b in contact with the interface surface Γ_c. Each physical sub-problem is subdivided in three computational sub-domains. To be efficient in parallel, communications for the contact surface Γ_c between the sub-problems must be carefully designed.

2.2. Modelling pipeline

The pipeline used to obtain the fluid-electro-mechanic simulations is shown in Figure 4.

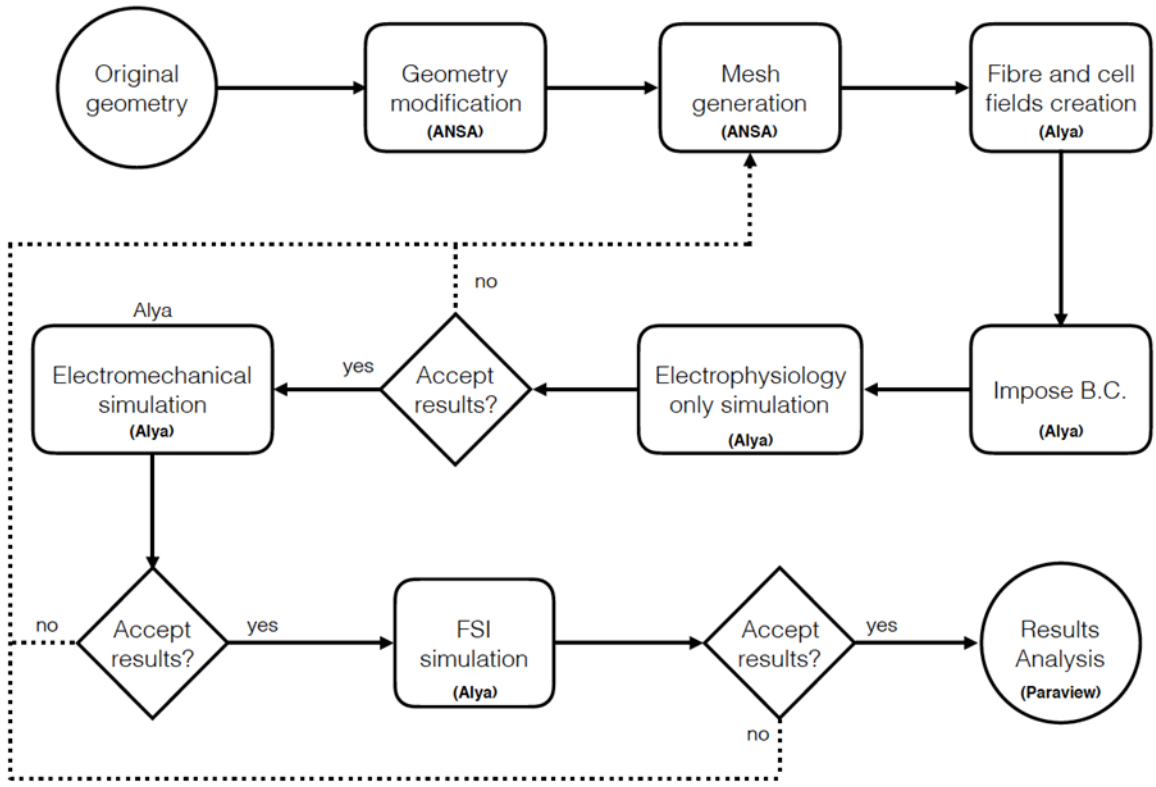

Fig. 4. Modelling pipeline. From pre-processing, simulation and post-processing for a fluid-electro-mechanic case including the software employed at each stage.

As a first step, an initial CAD geometry is modified, and the mesh is created with a pre-processing software. Then, the fibre and cell distribution are computed through a rule-based method, and the boundary conditions (B.C.) are imposed for each physics problem. After, each one of the problems is

incrementally added to the model, starting with EP, following with CSM and finishing with the coupled Fluid-Structure Interaction (FSI) problem that includes the CFD formulation. Once each physics problem is added, the simulations results are analysed to look for convergence problems and physical consistency with the originally defined problem. The most common encountered issue was after including the FSI formulation. Often, the intracavitary space contracts in such a manner that the elements of the fluid domain get extremely skewed and the CFD problem can diverge or the elements are inverted. In that case, the mesh should be rebuilt taking special care in the conflictive region.

2.3. Geometry and spatial discretisation for a fluid-electro-mechanic simulation

The whole heart geometry used to test the fluid-electro-mechanic simulation comes from the Zygote Solid 3D heart model [16] shown in Figure 5.

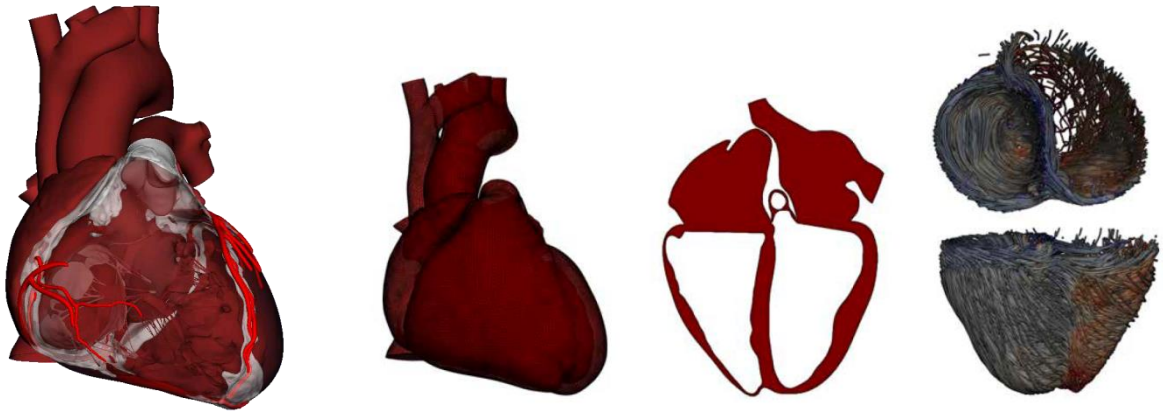

A) B)

Fig. 5. A) Heart geometry for a fluid-electro-mechanic model. Complete geometry of the original Zygote human heart model [16]. B) Volumetric mesh for simulations with the rule-based fiber orientations.

To modify the geometry and create the mesh, the commercial ANSA pre-processing software was used. This is a very handcrafted job that took several trial and error iterations until the mesh was good enough for modelling. The main modifications of the Zygote geometry were: (shown in Figure 5B).

- The non-specific structures were removed (i.e. fat and vessels).
- The valvular leaflets were removed, closing the space with a plane surface in the atrioventricular case.
- The geometry surfaces were modified to make them fit between each other.
- The atria was filled with an isotropic lineal solid material, with a density of ρ= 1.04 (g/cm^3), a young modulus of E = 5 [Ba] and a Poisson ratio of ν= 0.0005. This allows a physiological dynamic of the structure without modelling the atrial inner fluid dynamics.
- The inner surface of the endocardium were smoothed to reduce possible mesh inverting problems in the fluid mesh.
- The inner cavities volumes were created.

Spatial discretisation: The most common approach so far has been to use [17, 18, 19, 20] different meshes to simulate electrophysiology and solid mechanics, even though they are virtually the same domain. This approach is generally motivated by two reasons. On one hand, is generally observed that while the electrophysiology problem is eventually well parallelised, solid mechanics is not. On

the other hand, it is generally stressed that electrophysiology needs a finer mesh definition that solid mechanics. It is worth to remark that the use of different mesh sizes do not represent a problem per se (it is well known that solving in different mesh sizes and interpolating fields can arise stability problems). However, Alya is highly efficient to solve in parallel all of its programmed models. Therefore, we use the same mesh for the electrical and the solid mechanical problems. For this work, an average element size of 250 [m] is used. Both meshes are enforced to have matching nodes in the contact boundary, therefore the fluid domain mesh results almost as fine as the solid mesh.

2.4. Fibre orientation and cell heterogeneity

Fibre and cell distribution are critical for the electrical depolarisation and mechanical deformation of the myocardium. The fibre distribution can be experimentally recovered from animal or ex-vivo organs with diffusion tensor imaging magnetic resonance (DTI) [21, 22], allowing to have fibre distribution from biological tissues. This technique measures water molecules diffusion to reveal microscopic detail about fibre architecture. Currently, obtaining DTI measurements from clinical data is challenging, therefore fibre distribution can be also generated with rule-based methods [23, 24, 25, 26, 27]. These techniques find the relative position for each node in the domain with respect to the endocardium and the epicardium and assigns a fibre direction and cell tag. This is the state of the art methodology when DTI information is unavailable.

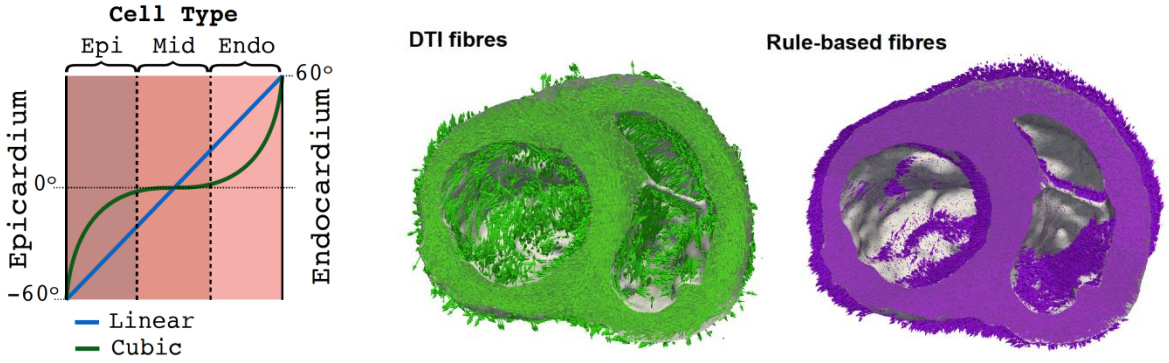

Fig. 6. Left: Fibre [27] and cell distributions from endocardium to epicardium. Center: DTI fibre orientations of an ex-vivo experimental study. Right: Rule-based fibres on the same ex-vivo experimental geometry.

2.5. Diffusion Tensor MRI

Diffusion Tensor Imaging (DTI) is an emerging technique for non-invasive reconstruction of the cardiac fiber architecture based on water diffusion properties [29,30]. In fact, ex-vivo DTI has been proven to be greatly reproducible in the assessment of myocardial microstructure [29, 30, 31, 32] as shown in Figure 6, whereas in-vivo implementation remains a challenge affected by technical difficulties, including intrinsic motion and poor resolution [33]. In-vivo limitations to integrate fiber organization with scar distribution using CMR and further assessment of ventricular arrhythmia risk and VT features can be overcome using a well-described pig model of infarct-related VT [28].

2.6. Electrophysiology

Ion channel dynamics are modelled by fitting ODEs to experimentally measured transmembrane currents. Today most complex cell models include a wide range of transmembrane ionic currents measured in dog [35] or human [36] tissue. These complex models are used to simulate the electrical activity of the heart in normal conditions and under complex chaotic depolarisation patterns like re-entry [37, 38, 39].

Despite cell models are preferred due to the high detail of the transmembrane currents, these are more computationally expensive and rely on a large set of parameters difficult to personalise. Due to this, phenomenological models are still popular. In this way, the electrophysiological models used nowadays can be classified in phenomenological and cell models. An extensive review on electrophysiology models can be found in [40].

2.6.1.Electrophysiology module in Alya

Human ventricular electrophysiology biophysically-detailed models and simulations have replicated experimental and clinical recordings in a range of healthy and disease conditions, and also under drug action. Their maturity has triggered interest and impact beyond academia, such as the adoption of the state-of-the-art OHara-Rudy model [36] for industrial and regulatory purposes, within the CiPA initiative sponsored by the US Food and Drug Administration. Studies have shown prediction of drug-induced clinical arrhythmic risk in human with 89% accuracy while data obtained from previously conducted animal studies for similar datasets showed up to 75% accuracy [41].
Simulation of propagation of electrical excitation was achieved through the monodomain equations [42,43] in the form:

$$\chi C_{\mathrm{m}} \frac{\partial V}{\partial t} - \nabla_{\mathbf{X}} \cdot (\mathbf{D}_0 \nabla_{\mathbf{X}} V) + \chi I_{\mathrm{ion}}(V, \mathbf{w}, \mathbf{c}) = \chi I_{\mathrm{app}}(\mathbf{X}, t), \tag{1}$$

$$\frac{\mathrm{d}\mathbf{w}}{\mathrm{d}t} = \mathbf{m}_{\mathbf{w}}(V, \mathbf{w}, \mathbf{c}), \tag{2}$$

$$\frac{\mathrm{d}\mathbf{c}}{\mathrm{d}t} = \mathbf{m}_{\mathbf{c}}(V, \mathbf{w}, \mathbf{c}), \tag{3}$$

where ***V*** is the transmembrane potential, ***w*** are the gating variables that regulate the transmembrane currents, ***c*** are the ionic concentrations inside of the cell, $\boldsymbol{m_x}$ is the right-hand side of the system of ODEs corresponding to the generic sate variable vector ***x***,***X*** is the surface to volume ration, $\boldsymbol{C_m}$ is the membrane capacitance per unit area, $\boldsymbol{I_{ion}}$ ae the ionic currents, and $\boldsymbol{I_{app}}$ is the applied current triggering the electrical depolarisation acting on specific anatomical locations. The orthotropic tensor of local conductivities in the reference configuration is defined as

$$\mathbf{D}_0 = \sigma_{\mathrm{f}}\, \mathbf{f}_0 \otimes \mathbf{f}_0 + \sigma_{\mathrm{s}}\, \mathbf{s}_0 \otimes \mathbf{s}_0 + \sigma_{\mathrm{n}}\, \bar{\mathbf{n}}_0 \otimes \bar{\mathbf{n}}_0, \tag{5}$$

Where σ_f, σ_s and σ_n are, respectively, the conductivities in the fibre, sheet and normal directions. These equations describe the membrane kinetics as well as the local transport of ions within cells. The human cell model consists of a system of ODEs with 41 state variables, and it exhibits a highly stiff behaviour, mainly due to the activation of sodium ionic current, which causes a sudden spike in the transmembrane potential V. This is the model that shows closer agreement with experimental recordings in a range of conditions and that has been adopted as the basis for the CiPA initiative for drug assessment, sponsored by the Food and Drug Association (FDA).

2.6.2. Discretisation

The linear diffusive terms can be integrated by parts using either open or closed rules. Closed integration is used in the ionic current term Iion(ϕ) to preserve the nodal character. This strategy used for the non-linear part produces a trivially invertible diagonal mass matrix. The discrete equations are solved using a first order Yanenko operator splitting where the Cell Model is explicitly solved using a Forward Euler scheme and the Tissue Model is solved implicitly with either a Backward

Euler or a Crank-Nicolson scheme. From numerical experiments we observed that as the main critical time limitation comes from the Tissue Model, the proposed scheme is both efficient and accurate enough.

2.6.3.Electrophysiology model verification

Numerical verification is essential to know if the model is correctly implemented in our code. For electrophysiological models, the main verification test was published by Niederer et al [44]. Mesh convergence of electrophysiological models was evaluated by multiple codes with the N-version verification test proposed in [44]. We have replicated the test, using the same geometry, boundary conditions and mesh, but using the O'Hara-Rudy cell model [36]. Results were compared against the presented in the cited publication.

The slab described in Figure 7 was employed to create the computational mesh. A mesh subdivision was employed to refine the grid and perform a mesh convergence test. On the refinement, each tetrahedral element of the original mesh is divided into eight subtetrahedrons. When the mesh was refined ones we denote the new mesh by div1. In the case that the refinement algorithm was applied two or three times, the resulting meshes were denoted by div2 or div3, respectively. We employed a monodomain O'hara-Rudy cell model instead of the original the ten-Tusscher [35] model used in the test. A sensitivity analysis of the model to the spatial and the time discretization was performed.

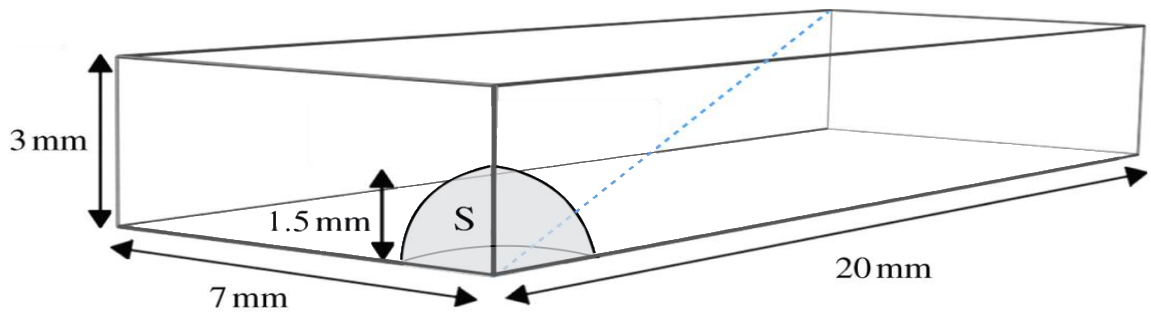

Fig. 7. Electrophysiological model verification. Scheme of the simulation domain. The stimulus applied was in the partial sphere S. Modified from (35).

Longitudinal fibre orientation was defined in the long axis of the slab direction. All boundaries had zero-flux condition. A stimulus of -50 mV was imposed during 2 ms on the slab corner of point (0; 0; 0) for the O'Hara- Ruddy model. A cycle length of 857 ms was imposed and the diffusion longitudinal and transversal were defined as 0.0009529 and 0.000125757 (cm^2/s), respectively. The cell model initial variables are described in Table 1.

Table 1. Cell model initial conditions

Membrane potential	-85.23 mV	L-type Ca current d gate	3.373×10^{-5}
Rapid K current X_{r1} gate	0.00621	L-type Ca current f gate	0.7888
Rapid K current X_{r2} gate	0.4712	L-type Ca current f2 gate	0.9755
Slow K current X_s gate	0.0095	L-type Ca current fCass gate	0.9953
Fast Na current m gate	0.00172	Transient outward current s gate	0.999998
Fast Na current h gate	0.7444	Transient outward current s gate	2.42×10^{-8}
Fast Na current j gate	0.7045	Ryanodine receptor R_{prime}	0.9073
Sarcoplasmatic reticulum Ca	3.64 mM	Intracellular Ca	0.000126 mM
Intracellular Na	8.604 mM	Subspace Ca	0.00036 mM
Intracellular K	136.89 mM		

The electrical depolarisation velocity was measured along the major diagonal of the slab, from the stimulation corner to the opposite one (Figure 7). Plotting the activation time as a function of the distance on the diagonal, shows a curve which has a slope equal to the inverse of the propagation velocity. The time discretisation employed on the analysis were Δt = 0.05, 0.01 and 0.005 ms. In the case of spatial discretisation, for each Δt several Δx are described in Table 2.

Table 2. Mesh characteristics

	Elements	Volume $[\mathrm{cm}^3]$	Edge length range $[\mathrm{cm}]$
Original mesh	20664	2.032×10^{-5}	$(0.05, 0.07)$
div1	165312	2.540×10^{-6}	$(0.025, 0.035)$
div2	1322496	3.176×10^{-7}	$(0.0125, 0.0175)$
div3	10579968	3.970×10^{-8}	$(0.00625, 0.00875)$

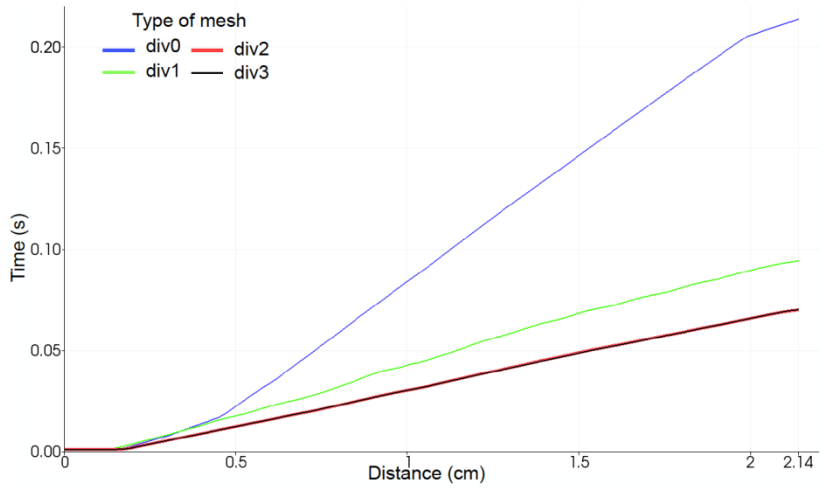

Fig. 8. Electrophysiological model verification. Activation time vs distance along the diagonal. A time discretization of Δt = 0.05 s and Δx defined by the refinements (div1, div2, div3) applied to the original mesh (div0). The curves corresponding to div2 and div3 were coincident.

The results are comparable to those presented in [44]. In meshes with larger elements, the wave velocity is slower. If we refine the mesh, the curves showed on Figure 8 converge. Moreover, the curves from simulations using div2 and div3 meshes are almost identical and the activation patterns are also similar (Figure 7.3). The corresponding to simulations on the meshes where divisor was applied 2 and 3 time are almost identical. The corresponding wavefront velocities are 26.936 cm/s and 27.262 cm/s, for div2 and div3 respectively (Table 7.3). This means that for volumetric elements equal or smaller than $3.176x10^{-7}$ the results were converged at Δt = 0.05. The electrical depolarisation patterns are equal for elements smaller than this value.

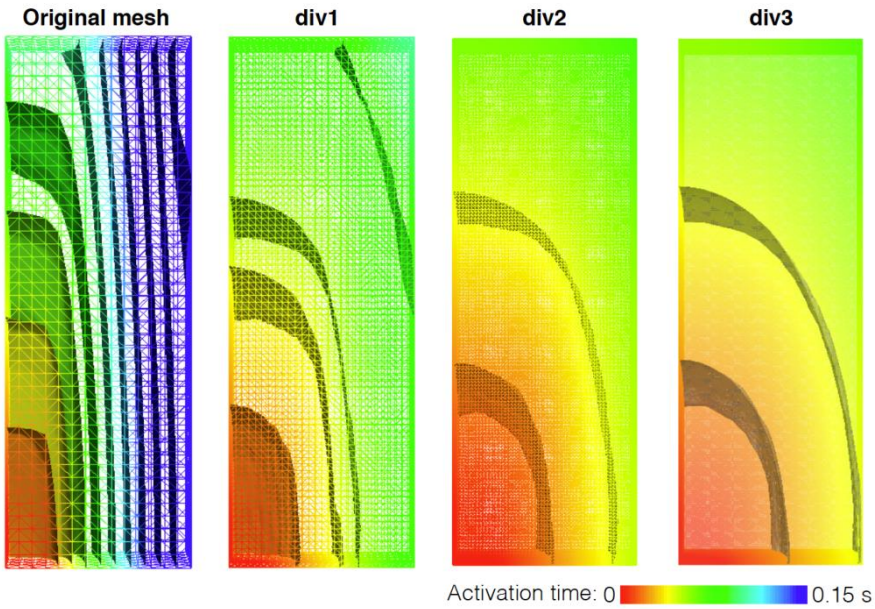

Fig. 9. Electrophysiological model verification. Activation time of the four simulations of the original mesh and one (div1), two (div2) or three times (div3) refined, the isochrones or the activation times are plotted every 0.02 s.

Time convergence. We have run the simulations employed at three different time discretizations of the meshes and refinements described above up div2, where mesh was converged. The variations on the time step size Δt did not substantially affect the conduction velocity.

Table 3. Conduction Velocity dependent on the element size and Δt

	$\Delta_t = 0.05$ms	$\Delta_t = 0.01$ms	$\Delta_t = 0.005$ms
Original mesh	8.0465	8.014	8.034
div1	19.630	19.330	19.209
div2	26.9367	26.626	26.364

2.6.4. Sensitivity analysis of the diffusion coefficient

The electrophysiological models depend on several parameters, which include diffusion, that cannot directly be extracted from experimental data. The diffusion tensor D was defined as a 3x3 diagonal matrix. Values on the diagonal correspond to the fibres longitudinal, normal and sheet plane diffusion. We considered a transversely isotropic material medium and we assumed that the normal and sheet plane diffusion are the same. We define a longitudinal fibres diffusion Dl and a transversal to fibres diffusion Dt. The diffusion is related to the depolarisation wave velocity. We aim to describe how variations in the diffusion affect the propagation velocity. To do so, we have performed a sensitivity analysis of the model to the diffusion parameters and after we have quantified the velocity changes. The objective is to be able to approximate diffusion values based on the depolarisation velocity given by electro-anatomic activation maps.

The slab, employed on the test verification in Section 3.3, was also chosen to perform the diffusion sensitivity analysis. We imposed a uniform time discretization of Δt = 0.05 ms and several spatial discretization Δx were evaluated refining the mesh.

The cell model employed was an adaptation of the O'Hara-Rudy model for pig tissue. The main difference on the swine model was the elimination of the transient outward K+ current (Ito), in pigs

this currents is inexistent. To define the cell model initial variables at the desirable cycle length of 400 ms, a cell simulation was previously run in Matlab. The O'Hara-Rudy without Ito was employed to run the cell simulation where a stimulus was imposed every 400 ms and the cell model was run up to a steady state, 1000 ms. The resulting cell currents were saved and incorporated to the tissue simulations as initial variables. We made the assumption that there was a cellular homogeneity and all the cells were considered as endocardial cells.

On the slab simulation the cycle length was defined at 400 ms, the same as on the experimental electrophysiological procedure. The diffusion Dl and Dt were set to 0.001171 and 0.00039033, respectively. First, a mesh convergence was performed. We have evaluated the wave velocity in the diagonal vd, longitudinal vl and transversal vt direction. The velocities along the slab diagonal were calculated as in the verification test described in Section 3.3. The propagation velocity along the longitudinal fibre direction coincides with the long direction of the slab and defines the maximum propagation velocity. In the case of the transversal direction, it is coincident with the velocity in the direction the small edges of the slab and defines the minimum propagation velocity. The maximum and the minimum propagation velocities were calculated by plotting the activation time along the longitudinal and transversal fibre direction, respectively. The velocities calculated on the mesh convergence analysis of this problems are summarised in Table 3.

Table 4. Velocities along the slab diagonal and the longitudinal and transversal direction to fibres to evaluate mesh convergence.Taking as a reference the velocities.

	Edge length [cm]	**Velocity** [cm/s]		
		$\mathbf{v_d}$	$\mathbf{v_l}$	$\mathbf{v_t}$
Original mesh	(0.05, 0.07)	21.569	23.310	9.488
div1	(0.025, 0.035)	27.582	29.070	15.014
div2	(0.0125, 0.175)	32.537	34.247	19.967
div3	(0.00625, 0.00875)	34.187	36.900	22.284

Table 4 shows the results of the simulations using different values of diffusion. The references values for Dl and Dt were the ones employed on the mesh convergence performed during the problem definition of this section. This reference diffusion were multiplied by a range of values from 1 to 20 times in the slab simulations for the sensitivity test. Three different spatial discretisations were employed for each diffusion set.

The results from the different simulations are summarised in Table 5 and Figure 10. The longitudinal and transverse propagation velocities obtained on meshes where the divisor was applied once or twice were comparable. Also, it was observed that the ratio between the longitudinal and transversal velocities was approximately 2 in all cases.

Table 5. Wave Velocity of different diffusions.

Diffusion (D_l, D_t)	**Original mesh**	**div1** (v_l, v_t)	**div2** (v_l, v_t)
$\times 1$	9,488, 23.310	15.014, 29.070	19.967, 34.246
$\times 2.5$	18.533, 42,508	26.258, 50.891	33.240, 56.497
$\times 5$	28.571, 65.146	39.933, 76.046	80.645, 46.377
$\times 7.5$	37.037, 83.507	50.000, 94.340	55.299, 98.039
$\times 10$	44.486, 98.765	58.968, 111.111	64.603, 112.359
$\times 12.5$	54.115, 118.3432	68.866, 129.870	73.733, 131.579
$\times 15$	60.530, 131.147	76.677, 140.845	79.867, 142.857
$\times 17.5$	66.667, 143.369	83.333, 153.846	87.114, 156.250
$\times 20$	71.429, 153.846	87.114, 162.602	91.255 166.667

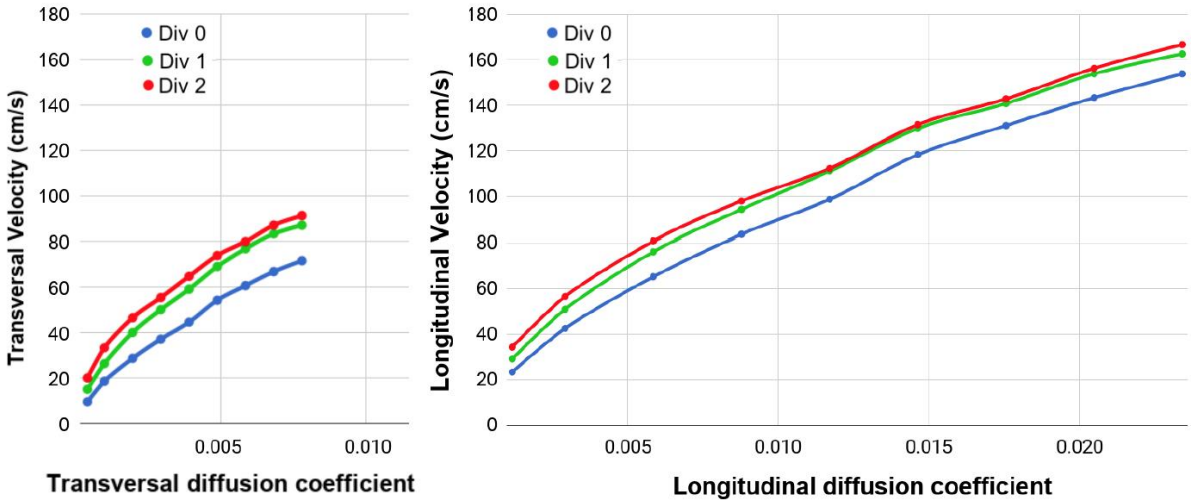

Fig. 10. Sensitivity analysis to diffusion. Transversal and longitudinal velocities change with the transverse and longitudinal diffusion coefficient respectively.

We have described how propagation velocity change with the diffusion coefficient for an experimental pig cell model parameterisation. The main application of these results is that if we know a priori the conduction velocity desirable for our computational model, we can employ the curves in Figure 10 to approximate the diffusion parameters required to run electrophysiological simulations. This is useful to reduce the parameterisation process on complex geometries that run under the same cell model conditions as required.

2.6.5. Subject-specific control simulations

The biventricular electrophysiological simulations were run to evaluate their capabilities when reproducing the beat of a healthy pig heart. The results were compared against experimental data from a control subject. The computational scenario was built based on the experimental data of one of the control cases. In general, cardiac electrophysiological simulation must include a Purkinje activation system in the model. However, the experimental scenario that we want to simulate includes pacing, so the electrical activation begins in the catheter tissue interface. As a consequence, and assuming that Purkinje network cannot be retrogradely activated by the pacing stimulus, we can neglect the Purkinje network for our simulation during pacing. The cell model properties were equal to the ones imposed on the diffusion sensitivity analysis in the slab (Section 3.4). Based on mentioned diffusion analysis, the following diffusion coefficients were chosen: 0.0231858 cm^2/s for the longitudinal diffusion and 0.007728534 cm^2/s for the longitudinal diffusion to obtain the desirable propagation velocity. The computational mesh was built from segmented CMR images obtained from an experimental protocol of monomorphic ventricular tachycardia in the pig.
The simulation mesh had an average element volume of 2.7055 $x10^{-5}$ cm^3. This element size is comparable with the one of the original slab mesh (2.032$x10^{-5}$ cm^3). To ensure that the simulation results are accurate, we applied the divisor once. A subdivision technique was used to obtain a 53.530.448 elements mesh with an averaged elements volume of 3.3819x 10^{-6} cm^3, similar to element side length of the div1, slab mesh (2.540 $x10^{-6}$ cm^2).
The following simulations were run on the refined mesh composed by 53 millions of elements. On this mesh, 10000 times steps were needed to run simulation of 500 ms in 196 cores, with a total calculation time of 30 minutes.In this section we have first performed two type of simulations: one including DTI fibre orientation and another including synthetic fibre orientation described by a mathematical rule-based model. Both simulations were compared against the activation maps from the experimental protocol. The main objective was to evaluate the power of simulations when

reproducing the beats of a healthy heart and describe the sensitivity of the model to the fibre distribution. Then, we have introduced two types of cells, endocardial and epicardial cells, on the model with DTI fibre orientation. We have evaluated the action potential in both types of cells and we have performed a S1S2 protocol to calculate the electrical restitution curves and compare them against the experimental ones. The main objective was to evaluate the cell model and compare it with the experimental data and build a reference case for future parameterisation of the cell properties on the model.

2.6.6. Numerical and experimental description of a heart beat

A cardiac beat starting with an external stimulus on a point in the RV endocardium was created using computational models including different fibre orientations (DTI and synthetic) to be compared to experimental activation maps. The activation time described the moment in which the activation wave pass through each node of the myocardium. The activation times, its gradients and the wavefront propagation velocity were calculated and compared. These comparisons between experimental and numerical data were done to analyse the accuracy of the computational models, as a first step towards validation of computational models.

Total activation time of the simulation with DTI fibres is similar to experimental data and larger than the simulation with synthetic fibres. The total activation time on the two computational models are different. The one resulting from the simulation including DTI fibres is 83.85 ms and 105.55 ms in the case of the simulation including rule-based fibres.

In the case of the experimental activation maps of the control case, the total activation time is 71.9 ms; closer to the one of the simulation using DTI fibres. The total activation time differences between the experimental and computational models, including both rule-based and DTI fibre orientations, are mostly due to differences of the basal geometry as shown in Figure 11. At 71 ms (the total activation time for experimental DTI data), the epicardium is almost completely activated in the simulation (Figure 11). The areas of the computational model that take longer to be activated, are marked in grey in the figure; which correspond to areas of geometrical differences. These differences exist because the accuracy of the ex vivo CMR imaging tool is larger than electrophysiological experimental studies.

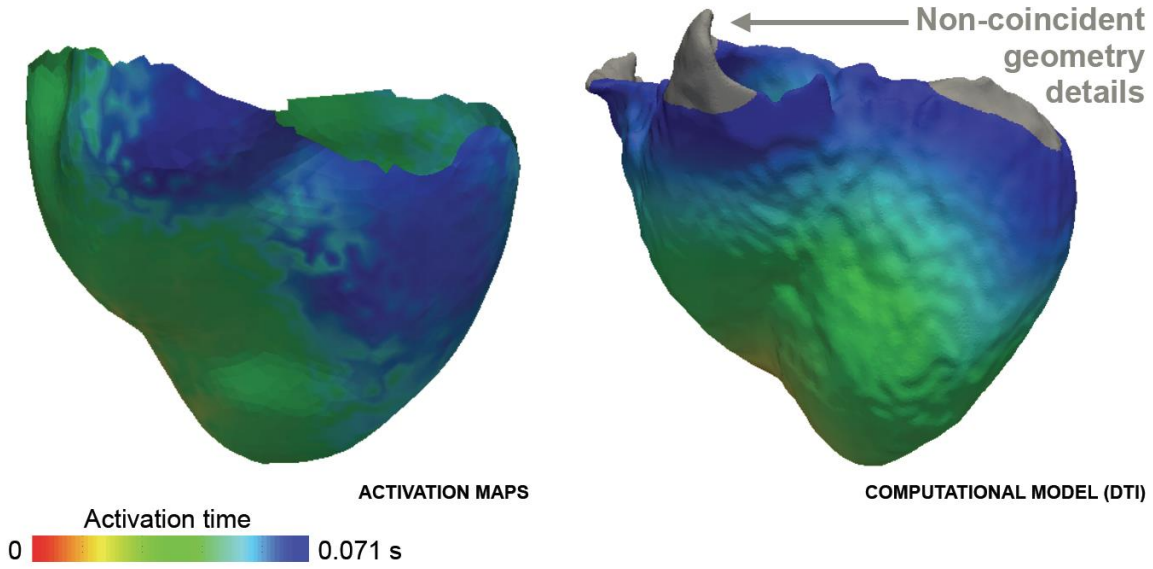

Fig. 11. Control case. Epicardial activatiom map geometry and the simulation including DTI fibres. For a local activation time of 0.071 s, the differences on the simulation case were due to geometrical details.

The fact that the depolarisation is slower in the simulation of the rule-based fibres is related with the different activation patterns (Figure 12).

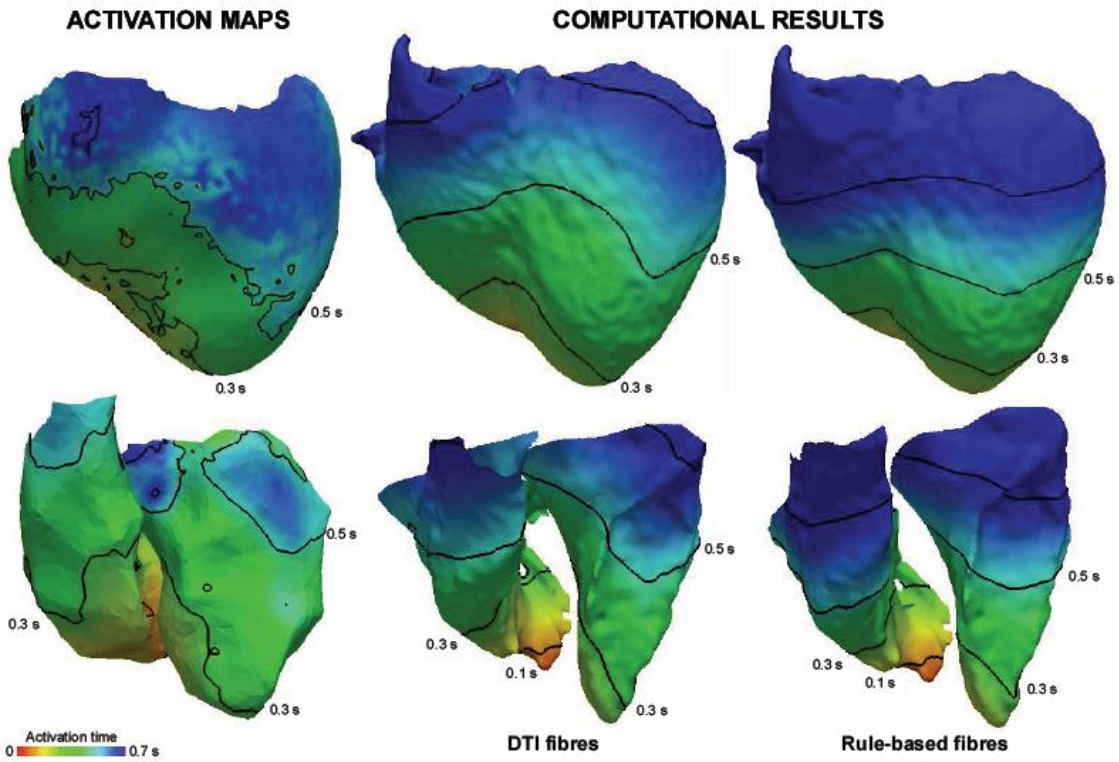

Fig. 12. Control case. Activation maps including isochrones of the epicardium and the endocardium from experimental and simulation data

Endocardial wavefront velocities are well reproduced. The median experimental conduction velocities are: 69.289 cm/s (epicardium), 119.855 cm/s (LV endocardium) and 152.795 cm/s (RV endocardium). The same algorithm was applied to the activation maps from electrophysiological simulations. We obtained that the median velocity for the simulations including DTI fibres were 116.870 cm/s in the endocardium and 137.94 cm/s in the epicardium. Similar velocities were found in the simulations including synthetic fibres. The median propagation velocity was 100.94 in the endocardium and 116.018 in the epicardium.

It is remarkable that the propagation wavefront is faster in the endocardium for experimental data and on the epicardium for computational models. However, velocities in the LV endocardium from experimental data and from simulations including DTI fibres were similar.

2.7. Excitation-Contraction-Coupling

Bidirectional electro-mechanical models with excitation-contraction-coupling (ECC) are two side problem. Electrical activity induces mechanical deformation but, also, mechanical stimulus can also induce transmembrane currents that develop in electrical activity. E.g. it has been proven [45] that ventricular filling slows down epicardial conduction and increases action potential duration. Also, in [46], the authors demonstrate that mechanical deformation could affect complex electrophysiological phenomena like spiral wave breakup. This effect, where mechanical stimulus induce electrical activity, is called mechano-electric feedback. This is a complex phenomena and only a few models exist for such behavior [47, 48, 49].

Recent work in Alya has been able to create a bidirectional excitation contraction coupling using the model published by Land et al. [49] Using this model, a sensitivity analysis was performed to assess the effect of mechanical and ECC parameters on physiologically relevant biomarkers. The publication is being written and should be published within the next couple of months. A brief description follows:

Coupling of the electrophysiology to the contractile machinery of the cardiomyocytes is represented through the human-based model of excitation-contraction coupling and active tension by Land et al. [49] The model is based on sets of ODEs describing the local dynamics of a vector of state variables q, which represents the contractile mechanisms in cardiomyocytes (see a detailed discussion about these models in [48]). The corresponding system of ODEs reads as (note the dependencies on stretch and stretch-rate).

$$\frac{dq}{dt} = m_q(q, c, \lambda_f, \dot{\lambda}_f). \tag{6}$$

where $\lambda_f = \sqrt{I_{4f}} = \sqrt{f_0 \cdot Cf_0}$ is the stretch in the fibre direction. The Land et al. [49] model consists of six state variables $q = \{S, W, CaTRPN, B, \zeta_s, \zeta_w\}$: S and W are variables associated with the crossbridge binding, respectively being the post-powerstroke and pre-powerstroke states, $CaTRPN$ represents the fraction of troponin C units with calcium bound to their regulatory binding site, B represents the fraction of blocked myosin binding sites on actin, and the state variables ζ_w, ζ_s dictate the pre-powerstroke and post-powerstroke distortion in a distortion-decay model.

The right-hand side terms defining m_q in assume the following form

$$m_q = \begin{pmatrix} k_{ws}W - k_{su}S - \gamma_{su}S \\ k_{uw}(1 - B - S - W) - k_{wu}W - k_{ws}W - \gamma_{wu}W \\ k_{TRPN}[(\frac{[Ca^{2+}]_{int}}{[Ca^{2+}]_{T50}})^{n_{TRPN}}(1 - CaTRPN) - CaTRPN] \\ K_u CaTRPN^{-\frac{n_{Tm}}{2}}(1 - B - S - W) - k_u CaTRPN^{\frac{n_{Tm}}{2}} B \\ A_s\dot{\lambda}_f - c_s\zeta_s \\ A_w\dot{\lambda}_f - c_w\zeta_w \end{pmatrix}, \tag{7}$$

where the state variable-dependent parameters are defined as

$$\begin{aligned} \gamma_{su} &= \begin{cases} \gamma_s(-\zeta_s - 1) & if \zeta_s + 1 < 0 \\ \gamma_s\zeta_s & if \zeta_s + 1 > 1, \\ 0 & otherwise \end{cases} \\ \gamma_{wu} &= \gamma_w|\zeta_w|, \\ [Ca^{2+}]_{T50} &= [Ca^{2+}]^{ref}_{T50} + \beta_1[min(\lambda_f, 1.2) - 1]. \end{aligned} \tag{8}$$

When the solution of the system of ODEs is achieved, the expression for the active tension in the fibre direction T_{act} can be retrieved as

$$T_{act}(q, \lambda_f) = \hat{h}(\lambda_f)\frac{T_{ref}}{r_s}[(\zeta_s + 1)S + \zeta_w W], \tag{9}$$

where

$$\hat{h}(\lambda_f) = \begin{cases} 0 & if \lambda_f < \dfrac{1.87\beta_0 - 1}{2\beta_0} \\ 1 + \beta_0(2\lambda_f - 1.87) & if \dfrac{1.87\beta_0 - 1}{2\beta_0} \le \lambda_f < 0.87 \\ 1 + \beta_0(\lambda_f - 1) & if 0.87 \le \lambda_f < 1.2 \\ 1 + 0.2\beta_0 & \lambda_f \ge 1.2 \end{cases} \quad (10)$$

and the remaining parameters are constant.

This system is coupled bidirectionally, and such that it now becomes

$$\frac{dc}{dt} = m_c(V,w,c,q). \quad (11)$$

Particularly, the calcium bound to troponin needed by the cell electrophysiology model is obtained from the excitation-contraction coupling model, which means that $\{c\}$ depends on $\{q\}$ as (a more complete derivation, following [49].

$$\frac{d[Ca^{2+}]_{int}}{dt} = \frac{1}{1 + \frac{[\overline{CMDN}]K_{CMDN}}{([Ca^{2+}]_i + K_{CMDN})^2}}(-I_{pCa} + I_{Cab} - 2I_{NaCa}\frac{A_{cap}}{2Fv_{myo}} - J\frac{v_{nsr}}{v_{myo}} + J_{Ca}\frac{v_{ss}}{v_{myo}} - [TRPN]_{max}CaTRPN), \quad (12)$$

where $[Ca^{2+}]_{int} \in \{c\}$ and $CaTRPN \in \{q\}$.

On the other hand, the calcium concentration needed by the excitation-contraction coupling model is obtained from the cell electrophysiology model, i.e. $\{q\}$ depends on $\{c\}$ specifically through the evolution of the calcium bound to troponin [49], in the form

$$\frac{dCaTRPN}{dt} = k_{TRPN}\left[(\frac{[Ca^{2+}]_{int}}{[Ca^{2+}]_{T50}})^{n_{TRPN}}(1 - CaTRPN) - CaTRPN\right], \quad (13)$$

where $[Ca^{2+}]_{int} \in \{c\}$ and $CaTRPN \in \{q\}$.

The electrophysiological and mechanical activity of the heart are bidirectionally coupled through active stress (from electrical diffusion to solid deformation) and the effect of deformation on diffusivity and stretch-activated ionic currents.

The relevance of this work is that Alya has the capabilities for solving highly complex, tightly coupled electro-mechanical models of the heart using HPC facilities in an efficient manner and taking into account all physiologically relevant boundary conditions. Linking Alya to subject specific data including genomics, protein structure and kinetics will be performed through MUSICO module, as a part of Task 5.4. Here, in the following section, we give just brief description how subject specific data will be incorporated into Alya (or PAK) finite element solver.

2.8. Solid Mechanics

The electrical activity of the cells is occurring in a solid domain that is deforming. In this way, the mechanical deformation of the tissue is as important as the electrical activity. When modelling the solid mechanics of the heart, two sources of stresses should be accounted, the passive and active portion. Passive stresses are a consequence of the structural properties of the cells and the connective tissues. Active stresses are a consequence of the electro-mechanical activity of the heart.

The final stresses produced in the tissue are obtained adding the passive stresses and the active stresses. A detailed description on the solid mechanics modelling currently working in Alya can be found in the published thesis by Alfonso Santiago.

To model solid mechanics we use the finite elasticity framework. The solid mechanics in the heartbeat problem should include the stresses produced by the material model, the boundary conditions, the fluid that is making pressure in the solid walls, and the active tension induced by the myocytes. The passive part is modelled as a slightly compressible invariant-type material [77]. The implementation has been published by Lafortune et al. [78]

Briefly, as an active stress formulation was used, the stress term is additively decomposed into passive and active terms, such that

$$\rho_0(X)\frac{\partial^2 u(X)}{\partial t^2} - \nabla_X \cdot [F(S_{pas} + S_{act})] = 0, in \Omega_0 \times (0,T]. \tag{14}$$

Here the active Second Piola-Kirchhoff stress tensor is defined as

$$\begin{aligned}\mathbf{S}_{\mathrm{act}} &= J\mathbf{F}^{-1}\boldsymbol{\sigma}_{\mathrm{act}}\mathbf{F}^{-\mathrm{T}} \\ &= J\mathbf{F}^{-1}\left[\frac{1}{J}\left((T_{\mathrm{act}}+\sigma_0)\frac{\mathbf{F}\mathbf{f}_0\otimes\mathbf{F}\mathbf{f}_0}{\lambda_{\mathrm{f}}^2} + k_{\mathrm{ort}\,1}T_{\mathrm{act}}\frac{\mathbf{F}\mathbf{s}_0\otimes\mathbf{F}\mathbf{s}_0}{\lambda_{\mathrm{s}}^2} + k_{\mathrm{ort}\,2}T_{\mathrm{act}}\frac{\mathbf{F}\mathbf{n}_0\otimes\mathbf{F}\mathbf{n}_0}{\lambda_{\mathrm{n}}^2}\right)\right]\mathbf{F} \\ &= (T_{\mathrm{act}}+\sigma_0)\frac{\mathbf{f}_0\otimes\mathbf{f}_0}{\lambda_{\mathrm{f}}^2} + k_{\mathrm{ort}\,1}T_{\mathrm{act}}\frac{\mathbf{s}_0\otimes\mathbf{s}_0}{\lambda_{\mathrm{s}}^2} + k_{\mathrm{ort}\,2}T_{\mathrm{act}}\frac{\mathbf{n}_0\otimes\mathbf{n}_0}{\lambda_{\mathrm{n}}^2},\end{aligned} \tag{15}$$

where k_{ort1} and k_{ort2} are activation parameters acting in the sheet and normal directions, respectively. These constants are taken as in [79], in which an orthotropic active stress tensor is assumed, considering that mechanical activation occurs differently in each local direction. It is important to point out that the pre-stress appears only in the fibre direction.

2.9. Boundary Conditions

2.9.1 0D Hemodynamics

Solving the fluid structure interaction problem to solve the hemodynamics is not always feasible or required for the specific purposes of the simulations being performed. Therefore, a methodology for incorporating the effect of hemodynamics in a less computationally costly manner was recently programmed in Alya. This approach provides the appropriate boundary conditions to represent the blood flow inside each ventricle. This was implemented through a state machine with four phases, one for each of the cardiac phases during a heart beat: isovolumetric contraction, ejection, isovolumetric relaxation and filling as follows:

Initiation. This phase is needed in order to bring the system to the end of diastole. The ventricular pressure applied to the endocardium is brought up to healthy left ventricular end-diastolic pressure linearly throughout the phase. In order to keep the volume constant during this phase, a pre-stress σ_0 is assumed to follow the fibre direction and is initialised at t = 0 with a relatively small value and is further adjusted during this phase. The pre-stress σ_0 is kept constant for the rest of simulation, at the converged value obtained in the last time step of this phase.

Ejection. When the ventricular pressure surpasses the arterial pressure, the aortic valve opens and the ejection phase begins, eventually leading to a reduction in ventricular volume. To model the blood pressure of the systemic circulation system during the ejection phase, the two element Windkessel model is used.

Isovolumetric relaxation. When the ventricular flow reverses, i.e. _Vendo > 0, the isovolumetric relaxation phase begins. In this phase, the ventricular pressure decreases while keeping the ventricular volume constant at the end-systolic volume (ESV). The pressure is therefore obtained analogously to the isovolumetric contraction phase.

Filling. The isovolumetric relaxation phase ends when the pressure drops below a specified threshold. Blood flows from the atria to the ventricle while the ventricular volume returns to its initial value (end-diastolic volume). In this phase, the ventricular pressure is modelled with the following a decay equation.

2.9.2 1D Arterial network

The complexity of these systems motivates simplifying models capable of reproducing the main characteristics of interest, i.e.: wave propagation in the cardiovascular circulatory system. Drastically reducing the computational cost, one-dimensional mathematical models are an option which has been extensively studied in application to blood circulation in arteries [80]. Following the work of Formaggia et al. [81] we have developed a one-dimensional finite element model capable of reproducing the main wave-propagation characteristics in the human arterial system. With the objective of being able to run patient-specific simulations in the limited time frames required by practitioners, the algorithm is fully parallelizable between tubular segments so that it will provide HPC-grade efficient simulations. Our code allows the prescription of time-dependent boundary conditions making possible to couple with three-dimensional models. In particular, we plan to couple the one-dimensional model to the fully coupled fluid-electromechanical model of the human heart developed by Santiago et al. [82] contained in Alya, the HPC multi-physics code developed at CASE, BSC [83].
The governing equations and numerical techniques for the one dimensional arterial network, are extensively described in [86]. Blood flow in large arteries can be modeled using the condensed 1D Navier-Stokes equations in compliant vessels, which comprise momentum and mass conservation as follows:

$$\begin{aligned} \frac{\partial Q}{\partial t} + \frac{\partial}{\partial x}\left(\alpha_m \frac{Q^2}{A}\right) + \frac{A}{\rho}\frac{\partial P}{\partial x} + \frac{2\pi R}{\rho}\tau_o = 0 \\ \frac{\partial A}{\partial t} + \frac{\partial Q}{\partial x} = 0, \end{aligned} \tag{16}$$

where A is the luminal area, R is the radius, Q is the flow rate, P is the mean pressure, ρ is the density and α_m is the momentum correction factor. The term τ_0 accounts for the viscous effects since and it has the following form:

$$\tau_o = \frac{f_r \rho U |U|}{8}, \tag{17}$$

where U is the mean velocity ($U = A/Q$) and fr is the Darcy friction factor corresponding to a fully parabolic velocity profile. 1D equations are analogous to the 3D versions where in 1D version we solve for Q and P and in 3D version for v and p. The fluid dynamic equations presented are complemented with a constitutive relation for the arterial wall induced pressure:

$$P = P_0 + \frac{Eh}{R_0}\left(\sqrt{\frac{A}{A_0}} - 1\right) + \frac{Kh}{R_0}\frac{1}{2\sqrt{A_0 A}}\frac{\partial A}{\partial t} \tag{18}$$

where index 0 refers to reference values, h is the wall thickness and E and K are the material parameters that characterise the elastic and viscoelastic material response respectively.

2.9.2.1 1D Coupling strategy

Both codes are coupled by a black-box decomposition approach previously proposed in [86]. For 3D-1D interface, information is exchanged at every iteration of the FSI problem (see Figure 30. The 1D arterial network is only directly coupled with the computational fluid dynamics (CFD) problem in the fluid-electro-mechanical model. This weakly coupled scheme is stable for relatively small time steps.

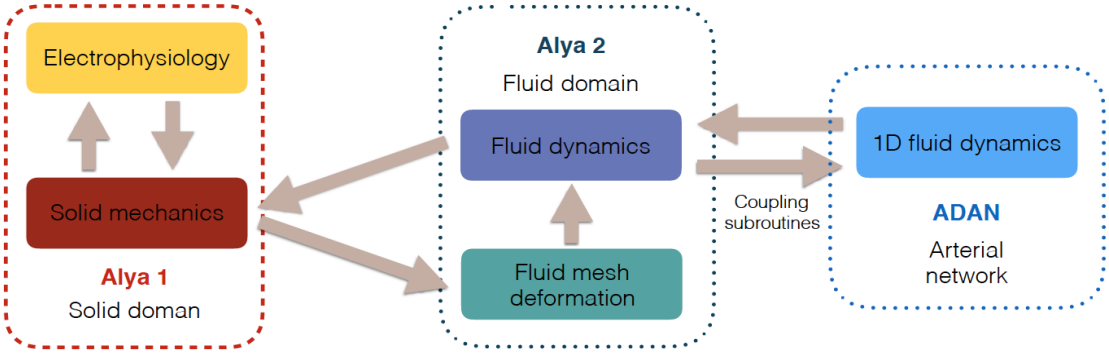

Fig. 13. Dimensionally heterogeneous model of the cardiovascular system. The scheme shows how the 1D arterial network model is coupled with the fluid-electro mechanical model. In this black-box approach the arterial model is only connected with the CFD problem.

At each time step, the 3D heart FSI problem is solved, computing the velocity field in the connecting boundary. To obtain the flow rate in the interface for the 3D model, the momentum is integrated and then divided by the area A of the boundary:

$$Q_{3D} = \frac{1}{\int_\Gamma d\Gamma} \int_\Gamma \rho u d\Gamma \tag{19}$$

This flow computed in the 3D heart problem is imposed in the arterial network. The 1D formulation is solved, and a pressure is computed for the connecting node. The pressure computed in the arterial network is weakly imposed in the boundary Γ of the 3D model as a forcing term:

$$f_p = \int_\Gamma P_i u d\Gamma \tag{20}$$

ror the 1D model, pressure and flow are degrees of freedom in each node of the 1D mesh. Following this statement, four unknowns are defined in the each nodal interface: Q1, Q2, P1 and P2, using the subindex to identify each model. But continuity of flow and pressure are enforced:

$$\begin{aligned} Q_i &= Q_1 = Q_2 \\ P_i &= P_1 = P_2 \end{aligned} \tag{21}$$

Additionally, not any combination of Qi and Pi is possible for each side of the interface: fixing Qi will automatically determine Pi in each one of the models. In this way, let be defined two equations that relates Qi and Pi in each node: $F_1(Q_i, P_i) = 0$ and $F_2(Q_i, P_i) = 0$. In this way, flow rate and pressure at the interface i corresponds to a state of the problem [74].

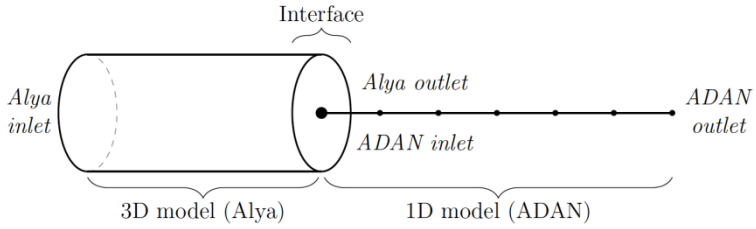

Fig. 14. Scheme of the model used in the first numerical test. A 3D cylinder was solved with Alya and a 1D cylinder was solved with ADAN.

2.9.3 Pericardium

The movement of the heart is modulated by the action of the surrounding tissues. In the computational solid mechanics, two different pericardial boundary conditions have been tested: the sliding pericardium and an elastic spring, which are used at the epicardium. The pericardium acts as a sort of sliding surface, avoiding normal displacements of the epicardium, but leaving the tangential direction almost free to move. Two studies have been performed using these approaches, one published by Alfonso Santiago [83], and the second one, will be published shortly. In the latter approach, the stiffness of the epicardium is being modelled as a Robin boundary condition.

The pericardial boundary condition as described in [83] attempts to reproduce a physiologic deformation of the ventricles, which includes a displacement of the valvular plane towards the apex of the ventricle, inducing apex-base shortening. In this way, articles that have reported results with excessively constrained boundary conditions like fixing the base of the heart, cannot reproduce at all the physiological movement of the ventricles. In [89, 90] authors from two different research groups propose a pericardium boundary condition as a frictionless contact problem. In [91] we propose a solution that with a different approach achieves a similar result, which is used in this work. We propose to restrict the normal displacements $d_i n_i = 0$ at the ventricular pericardium for the deformed configuration while allowing free displacements at the tangential planes, letting the boundary to slide. As a matter of fact, the "sliding pericardium" condition is not imposed in all of the pericardium, because we leave free the region near the valve plane to allow a more uniform and realistic movement. We acknowledge that this condition is a first order approach, because a better one should allow some normal movement but with a damper, combining a spring and a velocity-related viscous force (which has been now implemented and will be published in future work). In this work we show that even with the first order approach, the improvement is clear. The forces computed by the fluid mechanics are imposed in the endocardium. It is worth to remark that in our simulations, there is no other artificial endocardium boundary condition imposed. When used in the reviewed articles, such condition is applied on the normal direction (i.e. pressure) through a Windkessel function. Authors using this approach have the intention to model the work done by the fluid against the endocardium, as it is pumped out of the ventricles. However, when simulating single or bi-venticular geometries, applying this force requires to also fix the heart displacement somewhere else. As it is clearly shown in [96], when a pressure endocardium function is combined with fixing the base the resulting systolic movement is incorrect. In [91], although ventricles contract along their long-axis, the apex has a large displacement in apex-base direction and the base remains, of course, fixed. Although this can be visually corrected (quoting [91], "For visualization we shifted the deformed configuration such that the apex is fixed") this effect is not physiologically correct. On the other hand, we have observed that the pericardium and endocardium boundary conditions proposed in this work, produce a much more physiologically realistic movement.

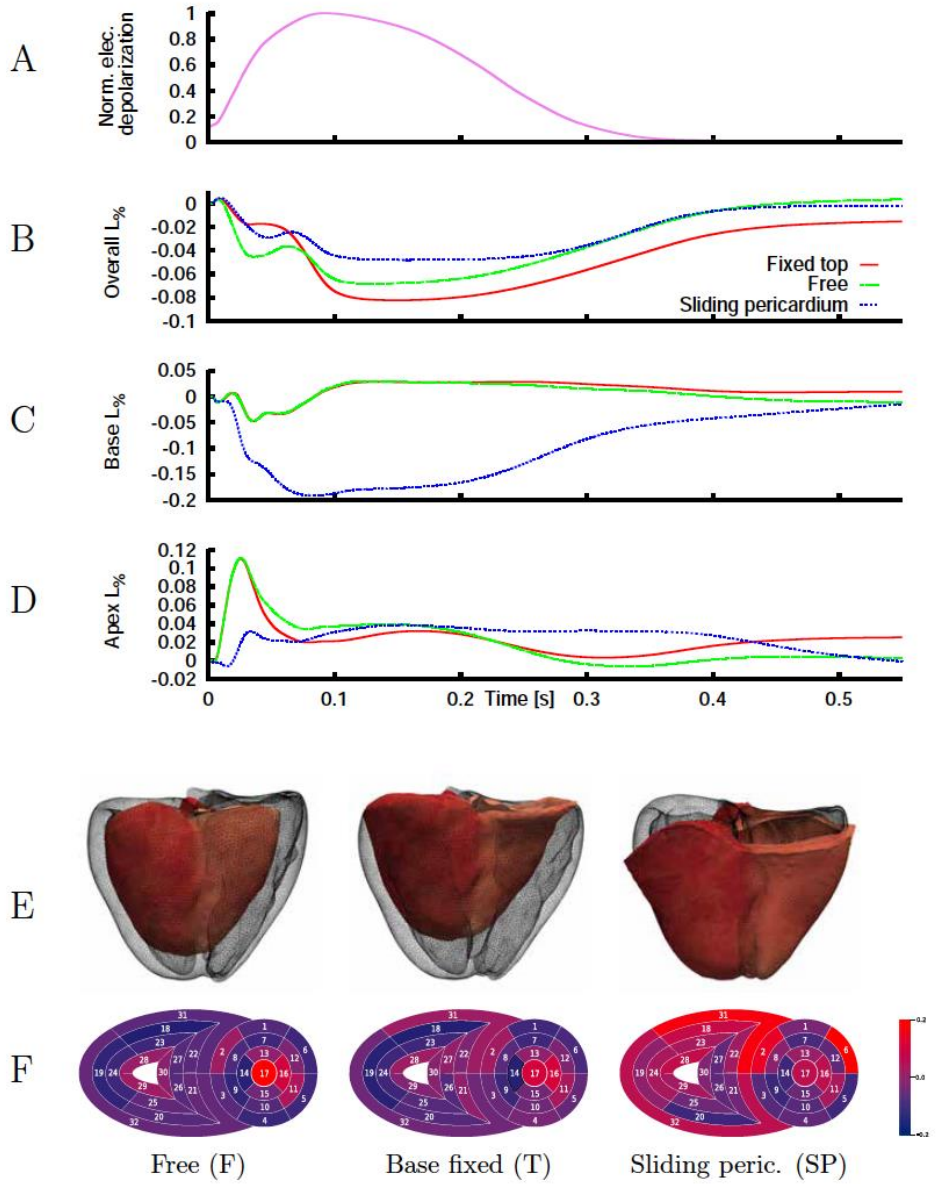

Fig. 15. Effect of pericardium boundary condition in a bi-ventricular geometry. Normalized electrical depolarisation is shown as a reference for the reader (A). The following three plots show overall (B), basal (C) and apical (D) longitudinal strain, respectively. Then (E), snapshots at maximum contraction for the three boundary conditions are shown. From left to right: Free(F), Based fixed (T) , and sliding pericardium (SP). Finally (F), the longitudinal strain is shown in the AHA plot segment-wise for each case.

2.9.4 Sensitivity analysis of mechanical parameters on physiologically-relevant biomarkers

A sensitivity analysis was performed to study which mechanical parameters have a strong influence on physiologically relevant biomarkers. These included ejection fraction (EF), which represents the amount of blood that is pumped during a heart beat; end-systolic pressure (ESP), which is the maximum ventricular pressure achieved in the left ventricle during a heart beat; longitudinal fractional shortening (LFS), which is a fractional version of the relative displacement between the endocardial apex and the base; and wall thickening (WT), which is the fractional version of the relative displacement between points in the endocardium and epicardium that are at the same position relative to the apico-basal axis.

Sampling-based approaches involve the generation and exploration of a mapping from the model parameters, for this study, the Latin Hypercube Sampling (LHS) was employed.

Ten mechanical parameters were included:

- Stiffness of the pericardium
- End-diastolic pressure
- Pressure at the start of ejection
- Windkessel capacitance
- Windkessel resistance
- Orthotropic stress parameter
- Active stress scaling parameter
- Fiber angle
- Bulk modulus
- Stress (linear) parameter in the sheet direction

Results showed that the relationships between parameters and biomarkers are monotonic (and nonlinear) in almost all of the cases. The parameter which affects the mechanical biomarkers more strongly is the active stress scaling parameter, with a particularly strong effect on EF. Results show that increasing the pressure at which the ejection phase is triggered increases the haemodynamic load of the left ventricle and delays the transition between isovolumetric contraction and ejection phases, directly affecting the maximum pressure obtained during a cardiac cycle. The results suggest that EF, ESP and LFS are mainly dominated by one or two parameters each: EF is dominated by the stress scaling parameter and inversely related to the orthotropic stress parameter; ESP is dominated by pressure at the start of ejection and inversely related to the orthotropic stress parameter; and LFS is dominated by the fibre angle and inversely related to the orthotropic stress parameter.

2.10. Computational Fluid Mechanics

2.10.1 Intraventricular CFD

The physics describing the fluid inside the ventricles are governed by the incompressible Navier Stokes equation. The discrete compact form for the Navier-Stokes equation can be rewritten by defining $v := v_i$ and let ϵ and σ be the velocity rate of deformation and the stress tensors respectively defined as:

$$\begin{aligned} \varepsilon(\mathbf{v}) &= \frac{1}{2}\left(\nabla \mathbf{v} + \nabla \mathbf{v}^T\right) = \left(\frac{\partial v_i}{\partial x_j} + \frac{\partial v_j}{\partial x_i}\right) \\ \sigma &= -p\mathbf{I} + 2\mu\varepsilon(\mathbf{v}). \end{aligned} \tag{22}$$

With this, we can define a vector with the unknowns $U = [v, p]^T$, a differential operator $L(U)$ and a force term F as:

$$\begin{aligned} \mathcal{L}(\mathbf{U}) &= \begin{bmatrix} \rho^f \left[\left(\mathbf{v} - \mathbf{v}^d\right) \cdot \nabla\right] \mathbf{v} - \nabla \cdot \left[2\mu\varepsilon(\mathbf{v})\right] + \nabla p \\ \nabla \cdot \mathbf{v} \end{bmatrix} \\ \mathbf{F} &= \begin{bmatrix} \rho^f \mathbf{f} \\ 0 \end{bmatrix}, \end{aligned} \tag{23}$$

where the domain velocity v^d becomes the mesh velocity v^m once the equation is discretized. If the matrix $M = diag(\rho^f I, 0)$, where I is the identity tensor, we can write the incompresible Navier-Stokes in the compact form:

$$\mathbf{M}\partial_t \mathbf{U} + \mathcal{L}(\mathbf{U}) = \mathbf{F}. \tag{24}$$

The numerical model is based on FEM, using the variational multiscale (VMS) method to stabilize convection and pressure. The formulation is obtained by splitting the unknowns into grid scale and a subgrid scale components, $U = U_h + \tilde{U}$. This subgrid scale $\tilde{U}$ is also modelled. Lets define $R(U)$ the Navier-Stokes residue as:

$$\mathcal{R}\left(\tilde{\mathbf{U}}\right) = \mathbf{F} - \mathbf{M}\partial_t \mathbf{U} - \mathcal{L}(\mathbf{U}). \tag{25}$$

Then the expression

$$\tilde{\mathbf{U}} = \tau \mathcal{R}\left(\tilde{\mathbf{U}}\right), \tag{26}$$

is considered for the stabilization where τ is a diagonal matrix, depending on the convection velocity. Solving strategy: the resulting system is solved through a velocity-pressure splitting strategy, already implemented in the Alya simulation code. Time discretization is based on second order backwards differences, and linearization is carried out using Picard method. At each time step, the system:

$$\begin{bmatrix} \mathbf{A}_{uu} \mathbf{A}_{up} \\ \mathbf{A}_{pu} \mathbf{A}_{pp} \end{bmatrix} \begin{bmatrix} \mathbf{u} \\ \mathbf{p} \end{bmatrix} = \begin{bmatrix} \mathbf{b}_u \\ \mathbf{b}_p \end{bmatrix}, \tag{27}$$

must be solved for velocity (**u**) and pressure (**p**) vectors. In order to solve this system efficiently in supercomputers, a split approach is used. The Schur complement is obtained and solved with an Orthomin (1) algorithm [72]. To do so, the momentum equation is solved twice using GMRES (Generalized Minimal Residual Method) and the continuity equation is solved with the Deflated Conjugate Gradient algorithm.

2.10.2 Fluid structure interaction

We need to compute the solution for the contact boundary (also called wet surface) Γ_c (see Figure 3). In this surface, the solid domain deforms the boundary and the fluid imposes forces due to the inertia, the pressure and the viscous stresses of the blood. In this part of the problem is where the multi-code approach described in Section 2.1 eases the implementation. Having two Alya instances solving the domain-specific problems, allows to easily implement the FSI relaxation strategies.
The main two families of methods to solve FSI problem are the following: the ALE and the immersed boundary (IB) methods [86]. The former deforms the fluid mesh following the solid wet boundary, and the latter tracks the wet surface in an Eulerian fluid mesh to enforce velocities in the fluid. The ALE method may require remeshing, but has a more precise solution. The IB method mesh requirements are more lenient, but the continuity equation may have convergence problems due to the spatial interpolation. Also, due to the same reason, the IB method lacks numerical precision. Alya already has efficient CSM and CFD solvers. In this way, reusing this codes to solve the FSI problem with the partitioned ALE method, is a natural way to proceed in our work. The FSI algorithm has been described in detail in [84,91], therefore results on biomedical applications will be described.

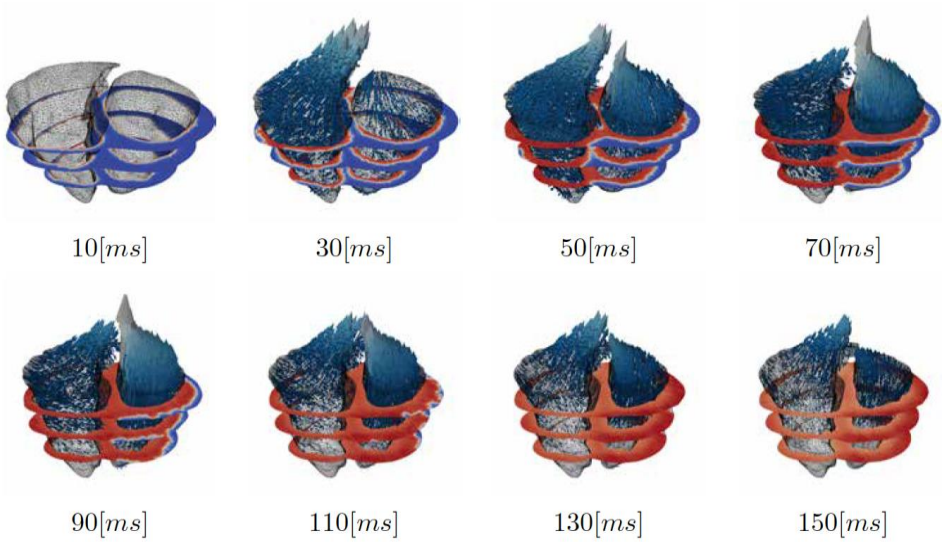

Fig. 16. Analysis of a healthy systole. Detail of the ventricular electrical depolarization, deformation and fluid dynamics.

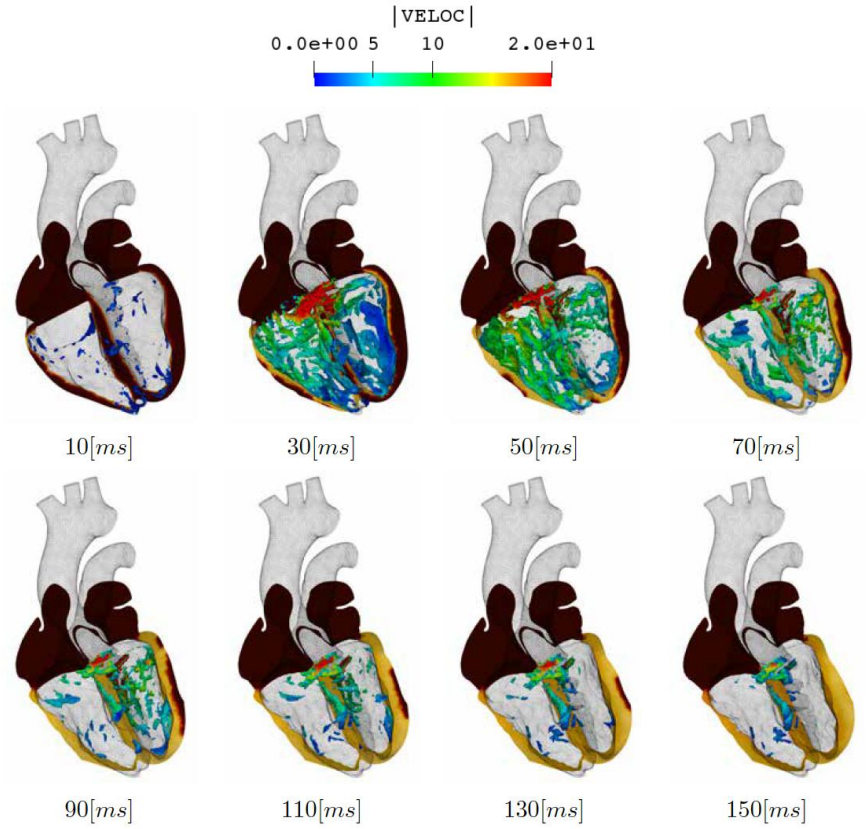

Fig. 17. Analysis of a healthy systole. Image sequence similar to Figure 31 but using Q-criterion isosurfaces at 50[s^{-2}]. Observe that the scale of the velocity module goes up to 20[cm/s].

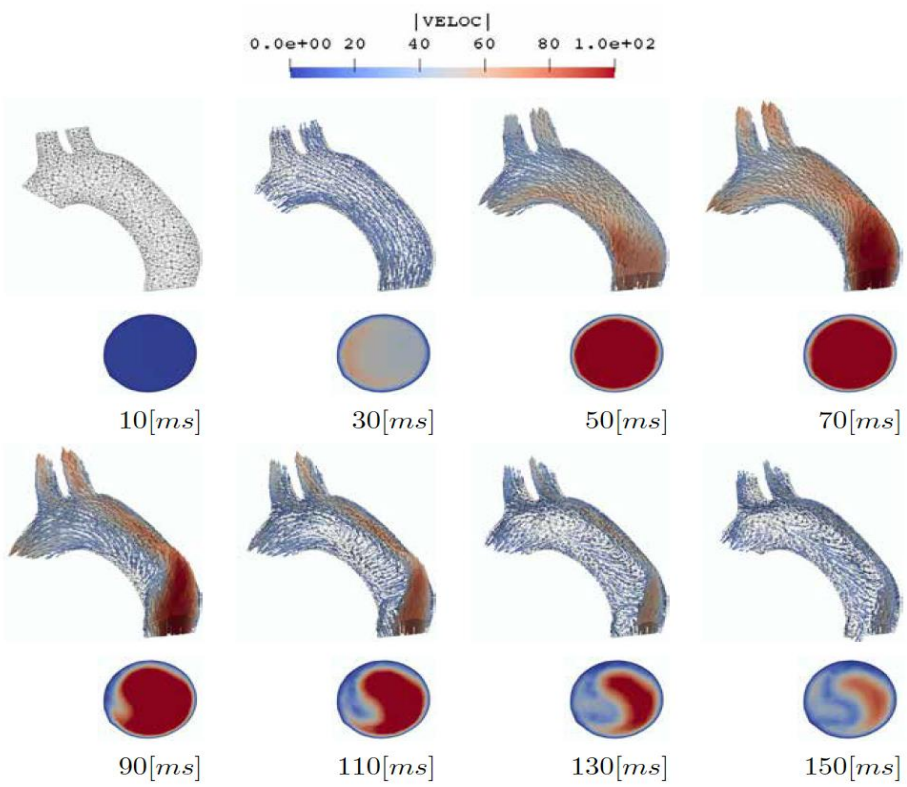

Fig. 18. Analysis of a healthy systole. Image sequence for the aorta showing the co-planar aortic arch output, the brachiocephalic output and the left common carotid artery output. Arrows and colors represents velocity. A short axis view for the aortic root is also shown. In this last view the helical pattern in the aortic root is clearly seen.

The ventricular fluid dynamics (in Figures 16, 17 and 18) features a fairly uniform and laminar flow, with maximum velocities of 9.8 [cm/s]. On the contrary, flow in Figure 41 features a more active pattern, with maximum punctual speeds above 80 [cm/s] (comparable with the 100 [cm/s] obtained with MRI measurements by [98]), with larger transversal gradients, and a slight backflow despite the net outflow condition. The aortic root section in Figure 18 shows a non-symetric flow, with a velocity pattern diverted to the lateral part of the aortic root. This flow pattern is also seen in experimental measurements [99, 100]. A similar study for the aortic root, comparing different imaging techniques with simulation results can be found in [100]. To finish the analysis for the healthy systole, in Figure 19 we compare a 4D flow MRI image [102] taken from [103] with the simulation results. Both figures show velocity path-lines, despite the chosen color scales are different. A high qualitative resemblance can be seen.

The results for the wholeheart fluid-electro-mechanical simulation model under normal conditions, at least for the systole, are similar to the experimental measurements, with a physiological behavior in most regions. This detailed analysis of the results also define a baseline for the following numerical experiments, where pathological conditions are modelled.

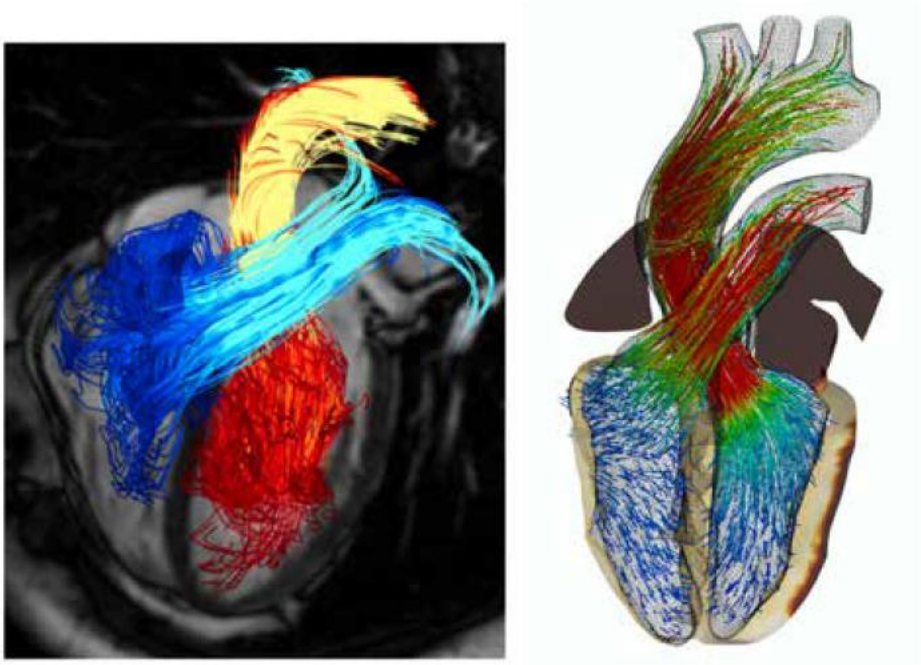

Fig. 19. Simulation of a healthy systole. Left: MRI 4D flow image taken from [103]. Right: simulation results with the whole heart model.

3. PAK

PAK [34] is high performance finite element analysis (FEA) software for solving complex coupled multi-physics / multi-scale problems. The software is written in Fortran 77/90/95. PAK consists of the two main modules: PAKSF, for solving coupled/decoupled solid-fluid problems including heart mechanics; and PAKT for modelling particulate or ionic mass transport and electrophysiology of the tissue in general, and also heart tissue. The PAK software includes: linear and geometrically and materially nonlinear structural analysis, linear and nonlinear particulate/molecule diffusive and convective transport, laminar flow of incompressible fluid with heat/mass transfer, solid fluid interaction, coupled ionic and electric transport, coupled mechanical deformations and ionic transport.

3.1 Electrophysiology module in PAK

Due to the enormous complexity of biological systems, it would be almost impossible to establish a detailed computational model of the electrical field, even for only a single organ (e.g. heart), including the entirety of cells comprising the neural network. In order to make computational models feasible for practical applications, we implemented the concept of smeared fields, which represents a generalization of the previously formulated multiscale smeared methodology for mass transport in blood vessels, lymph, and tissue (our recent references [50, 51, 52, 53, 54]). We demonstrated the accuracy of the smeared finite element computational models (CSFEM) for the electric field in numerical examples. The electrical field is further coupled with ionic mass transport within tissue composed of interstitial spaces extracellularly, and cytoplasm and organelles intracellularly. The proposed methodology, which couples electrophysiology and molecular ionic transport, is applicable to a variety of biological systems, including the heart.

3.1.1 A summary of the fundamental equations for gradient-driven physical processes and FE formulation

In this section we first summarize the gradient-driven problems related to mass transport in blood vessels and tissue, and electrophysiology. Then, we present a finite element formulation for these partial differential equations.

3.1.1.1 Fundamental equations for the gradient driven field problems

Flow through porous media. In case of incompressible fluid flow through a porous rigid medium, the governing relation is represented by the Darcy's law

$$v_i = -k_{Dij}\frac{\partial p}{\partial x_j},\ sum\ on\ j:\ \ j=1,2,3 \tag{28}$$

where v_i is the Darcy velocity (as fluid flux per unit area of the continuum) in direction x_i, p is fluid pressure and k_{Dij} is the Darcy tensor. The mass balance equation is

$$k_{Dij}\frac{\partial^2 p}{\partial x_i \partial x_j} + q_V = 0 \tag{29}$$

where q_V is a source term.

Diffusion. The constitutive law for diffusion is known as Fick's law,

$$Q_i = -D_{ij}\frac{\partial c}{\partial x_j} \tag{30}$$

and the mass balance equation is

$$-\frac{\partial c}{\partial t} - v_i\frac{\partial c}{\partial x_i} + \frac{\partial}{\partial x_i}\left(D_{ij}\frac{\partial c}{\partial x_j}\right) + q_V = 0, \quad sum\ on\ i,j:\ i,j = 1,2,3 \tag{31}$$

Here, c is concentration, Q_i flux and D_{ij} is the diffusion tensor. The generality is kept under the assumption that the diffusion tensor can be a function of concentration, i.e. it can be $D_{ij}=D_{ij}(c)$.

Electrostatics. The constitutive law is

$$J_i = -G\frac{\partial V_e}{\partial x_i} \tag{32}$$

where J_I is the electric flux, G is electric conductivity and V_e is electrical potential. The continuity equation for the current density can be derived from Maxwell equations in the form

$$\frac{\partial}{\partial t}\left(\frac{\partial D_i}{\partial x_i}\right) = -\frac{\partial J_i}{\partial x_i}, \quad sum\ on\ i,\ i = 1,2,3 \tag{33}$$

where the current density components D_i can be related to the potential V_e as

$$D_i = -\varepsilon\frac{\partial V_e}{\partial x_i} \tag{34}$$

where ε is the dielectric constant. Finally, the continuity equation is

$$\varepsilon\frac{\partial}{\partial t}\frac{\partial^2 V_e}{\partial x_i \partial x_i} = -G\frac{\partial^2 V_e}{\partial x_i \partial x_i} + q_V^e \tag{35}$$

where q_V^e is a volumetric source term (coming from ionic transport, [55]).

1D-conditions. For further presentation, we give the expressions for the 1D conditions. For the fluid flow the 1D conditions follow from the study of flow within pipes [56]. In case of a rigid pipe, the governing equation reduces to

$$k_{pipe}\frac{\partial^2 p}{\partial \overline{x}^2} = 0 \tag{36}$$

where $\overline{x}$ is the pipe direction and k_{pipe} is the pipe coefficient which can be derived from the so-called Hagen-Poiseuille law. Additional terms are present in the above equation for the case of deformable pipe [57], but will not be considered in this document.

In case of diffusion, the 1D conditions follow from equation (31). Hence, we have

$$-\frac{\partial c}{\partial t}-v\frac{\partial c}{\partial \bar{x}}+\frac{\partial}{\partial \bar{x}}\left(D\frac{\partial c}{\partial \bar{x}}\right)+q_V=0 \tag{37}$$

where $\bar{x}$ is the axis of propagation and *D* is diffusion coefficient. In the case of electrical conduction the governing equation has the form (36) with respect to the electric potential V_e, where instead k_{pipe} we have G_aA with A being the neural fiber cross-section.

The 1D electric current flow within neural fibers in case of impermeable fiber surface is given be eq. (36) where pressure *p* is replaced with electrical potential V_e, and the coefficient k_{pipe} is replaced with axial conductivity G_a. In case of permeable fiber surface, the current flow is governed by the so-called cable theory and will be described below.

Transport through membranes. Continuum domains of a composite media are often separated by membranes, or walls in case of blood vessels or neural fibers. For the presentation of the smeared methodology we give here the fundamental relations for transport through membranes. In case of fluid flow or diffusion we have

$$Q_w^p=k_w\left(p_{in}-p_{out}\right) \tag{38}$$

$$Q_w^c=D_w\left(c_{in}-c_{out}\right) \tag{39}$$

with the flux of fluid Q_w^p and mass due to diffusion Q_w^c oriented outward (from *in* to *out*); k_w and D_w are the wall hydraulic permeability and wall diffusivity, respectively. In the case of electrical field, the wall electrical flux relies on the so called cable theory, according to [58]. The outlet electrical flux (current density) I_m can be expressed as

$$I_m=G_m\left(V_e^{in}-V_e^{out}\right)+C_m\left(\frac{\partial V_e^{in}}{\partial t}-\frac{\partial V_e^{out}}{\partial t}\right) \tag{40}$$

where G_m is membrane conductivity and C_m is specific membrane (wall) capacitance.

3.1.1.2 Finite element formulation

The above governing equations can be transformed into the FE equations of balance by implementing a standard Galerkin weighting method [59]. The incremental-iterative balance equation for a single element, for a time step Δt and iteration *i*, can be derived in the form

$$\left(\frac{1}{\Delta t}\mathbf{M}+\mathbf{K}^v+\mathbf{K}\right)^{(i-1)}\Delta\boldsymbol{\Phi}^{(i)}=\mathbf{Q}^{ext}+\mathbf{Q}^V-\frac{1}{\Delta t}\mathbf{M}^{(i-1)}\left(\boldsymbol{\Phi}^{(i-1)}-\boldsymbol{\Phi}^t\right)-\left(\mathbf{K}+\mathbf{K}^v\right)^{(i-1)}\boldsymbol{\Phi}^{(i-1)} \tag{41}$$

where the matrices are

$$\begin{aligned}
M_{IJ}&=\int_V c_m N_I N_J dV\\
K_{IJ}^v&=\int_V v_i N_I N_{J,i} dV,\quad sum\ on\ i:\ i=1,2,3\\
K_{IJ}&=\int_V D_{km} N_{I,k} N_{J,m} dV,\quad sum\ on\ k,m:\ k,m=1,2,3\\
Q_I^V&=\int_V N_I q_V dV
\end{aligned} \tag{42}$$

Here **Φ** stands for pressure, concentration, or electrical potential as nodal variables; N_I are interpolation functions, V is element volume; c_m is mass coefficient (=0 for fluid flow, and =1 for diffusion); D_{km} for fluid is the Darcy tensor, while it is $G\delta_{ij}$ (δ_{ij} is the Kronecker delta symbol) for electrical field. For the case of Darcy's flow or no convection, the convection matrix $\mathbf{K}^v$ is equal to zero. For electrical potential we have that the "mass" matrix is

$$M_{IJ} = \varepsilon \int_V N_{I,k} N_{J,k} dV, \quad sum\ on\ k,\ k = 1,2,3 \tag{43}$$

and the convection matrix is equal to zero. Note that for 1D problems the equations have the same form as the above, with one index k and no summation; and that the element volume is $V=AL$, where A is cross-sectional area and L is the element length. Equation (41) assumes implicit integration scheme over time, i.e. all variables are evaluated at the end of time step and at the current equilibrium iteration. This integration scheme is unconditionally stable and provides the best accuracy [60].

For modeling transport through the membranes (walls) we have introduced connectivity 2-node elements for nodes at membranes [61] (Fig. 20a), by using double nodes at the same space position at the membrane, with one node belonging to one side and the other - to the other side of the boundary between two domains. The balance equation of the form (41) can be applied. The "mass" and transport matrices **M** and **K** can be written as

$$M_{11} = M_{22} = \frac{1}{3} c_{mm} A_m h_m, \quad M_{12} = M_{21} = \frac{1}{6} c_{mm} A_m h_m$$
$$K_{11} = K_{22} = -K_{12} = -K_{21} = D_w A_m \tag{44}$$

where A_m is the area of the surface belonging to the node, h_m is the membrane thickness; in case of diffusion D_w is the diffusion coefficient, while instead of D_w we have k_w and G_m for fluid flow and for electrical conduction, respectively; c_{mm}=0 for fluid flow and c_{mm}=1 for diffusion. For the case of electrical conduction the non-zero terms of the "mass" matrix are

$$M_{11} = M_{22} = A_m C_m . \tag{45}$$

3.1.2 Smeared model for field problems

To introduce the smeared methodology, we first consider a 'detailed model' of a composite medium. In Fig. 20a is shown a schematic of a medium composed of continuum domains-compartments and a network of fiber-like 1D domain. The continuum domains include extracellular space, cells and organelles. Capillaries and lymph as vessels, and neural fibers, are represented by 1D elements within extracellular space, while cells can contain organelles – hence the continuum domains have a hierarchical character. It is assumed that each domain has its own FE mesh of continuum elements, while 1D domains have their own 1D finite elements with the coordinate axes along the elements ($\bar{X}$ axis depicted at one of these fibers).

Connectivity elements are shown as A,B; C,D; E,F and enlarged at the top of the figure (the nodes C,D, also denoted as 1,2). The two nodes, 1 and 2, have nodal values representing the two domains (ϕ_{out} and ϕ_{in} in the figure). The connectivity elements assigned to the boundary common nodes, possess the following characteristics: transport coefficient according the membrane (or wall) material property, cross-section equal to the surface area A_m belonging to that node, and the length h_m equal to the membrane (wall) thickness.

From the detailed model description, it can be seen that significant effort is required to generate the model; and in case of a complex medium such as tissue, the model generation would be an impractical or even impossible task. This task would be much more demanding if instead of connectivity elements, continuum FEs are employed for membranes.

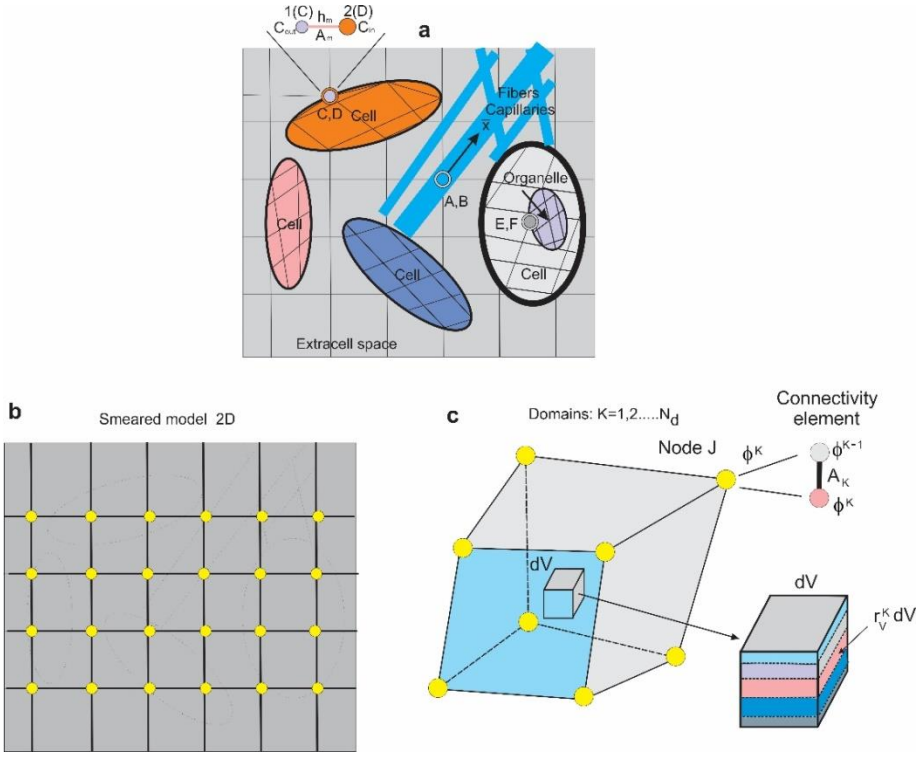

Fig. 20. Schematic of detailed model and smeared model. a) Detailed model of tissue as composite medium with continuum subdomains and capillaries/fibers, 2D representation, with continuum, 1D and connectivity elements; b) Smeared FE representation of the detailed model; c) Composite smeared finite element (CSFE) with subdomains and connectivity element at a FE node J.

We further introduce a smeared model by formulating a continuum composite finite element (CSFE) which includes all constituents (continuum and 1D) in a way that the true physical fields, corresponding to a detailed model, are represented in a smeared (a kind of average) sense, which should provide adequate accuracy. A schematic of the smeared model, for the same detailed model of Fig. 20a, is shown in Fig. 20b, with continuum elements present only. There are a few conceptual steps to formulate the CSFE element.

First, it is necessary to transform the 1D balance equations into the corresponding continuum format. The derivation of the Darcy and diffusion tensors is given in [50] while, for a general physical filed, the continuum transport tensor is derived in [53]. This tensor can be expressed as

$$D_{ij} = \frac{1}{A_{tot}} \sum_{K} D_K A_K \ell_{Ki} \ell_{Kj} \tag{46}$$

where

$$A_{tot} = \sum_{K} A_K \tag{47}$$

is the total area of 1D domains in a reference volume, surrounding a point in space, with cross-sectional areas A_K; D_K and ℓ_{Ki} are transport coefficients along the 1D elements and directional coefficients, respectively.

The next important statement in the CSFE formulation is that each domain has its own field within the corresponding volume of the CSFE. Hence, the FE node of the CSFE has a number of nodal

variables ϕ^K ('degrees of freedom') equal to the number of domains N_d, as shown in Fig. 20c. The domain volume V_K is related to the total element volume as

$$V_K = r_V^K V, \quad \text{and} \quad \mathrm{d}V_K = r_V^K dV \tag{48}$$

where r_V^K is the volumetric fraction.

Finally, we include connectivity elements to couple the corresponding domains. We introduce connectivity elements at each node of the CSFE, according to the above described connectivity elements in the detailed model. The cross-sectional area A_{JK} of a connectivity element at node J for the domain K can be expressed in the form

$$A_{JK} = \left(r_{AV}^K V_K\right)_J = \left(r_{AV}^K r_V^K V\right)_J \tag{49}$$

where r_{AV}^K is the area coefficient, i.e.

$$r_{AV}^K = \frac{A_K}{V_K} \tag{50}$$

and V_J is the volume of the total space of the continuum belonging to the node J. This volume can be evaluated as

$$V_J = \sum_{el} \int_{V_{el}} N_J dV_{el} \tag{51}$$

where summation *el* goes over all finite elements with the common node J. Note that all the surfaces, volumes and the volumetric and area ratios are assigned to nodes, which in practical applications is convenient for modeling of any non-homogenous property of the material system.

The finite element balance equations for continuum and connectivity elements are of the same form as in detailed model (equation (41)) with the matrices

$$M_{IJ} = \int_V c_m N_I N_J r_V^K dV$$

$$K_{IJ} = \int_V D_{ij} N_{I,i} N_{J,j} r_V^K dV, \quad sum\ on\ i, j:\ i, j = 1,2,3 \tag{52}$$

$$Q_I^V = \int_V N_I q_V r_V^K dV$$

where the material parameters are as in (42). In case of electrical field, the matrix **M** in (43) is now

$$M_{IJ} = \varepsilon \int_V N_{I,k} N_{J,k} r_V^K dV, \quad sum\ on\ k,\ k = 1,2,3 \tag{53}$$

and the source nodal vector due to ionic transport of a molecule m is [58]

$$Q_I^{mE} = \frac{DFz^m}{RT} \int_V N_I \frac{\partial}{\partial x_i} \left(c^m \frac{\partial V_e}{\partial x_i} \right) r_V^K dV \tag{54}$$

where D is diffusion coefficient, z^m is molecule valence, F is the Faraday constant, R is the gas constant, T is absolute temperature, and c^m is concentration. The surface areas entering into matrices of the connectivity elements are as given in [54].

3.1.3 Smeared model for electrical field

Here, the fundamental equations for electrostatics are summarized and then the smeared model is formulated in detail, following the general concept in the previous section.

First, consider electrical flow within nerve fibers. As schematically shown in Fig. 21a, the current flows along the axon, but there is also lateral flow through the axon wall due to so called spines shown schematically in Fig. 21a. The governing balance equation relies on the so-called cable theory. For the axial current flow along a nerve without lateral flow, the basic relation is

$$I_x = -G_a \frac{\partial V_e}{\partial x} \tag{55}$$

where I_x is the current density along the fiber axis x (as schematically represented in Fig. 21a) G_a is axial conductivity and V_e is electric potential. We will further use term "current" for current density (A/(unit area)). In case of large nerve fibers, there is practically only the axial flow, and the FE model consists of the 1D elements with a standard form (41) of balance equations [50].

The lateral flow can be expressed in the form (taking that current going out of the fiber is positive),

$$I_{mem} = G_m \left(V_e^{in} - V_e^{ext} \right) + C_m \left(\frac{\partial V_e^{in}}{\partial t} - \frac{\partial V_e^{ext}}{\partial t} \right) + I_{ion} \tag{56}$$

where G_m and C_m are wall conductivity and capacitance, respectively; V_e^{in} and V_e^{ext} are potentials within fiber and in the surrounding; and I_{ion} is ionic current due to flow of various charged molecules through the wall. The lateral flow is modeled by connectivity elements 1,2 at double nodes along fibers and on the cell membranes (Fig. 21b).

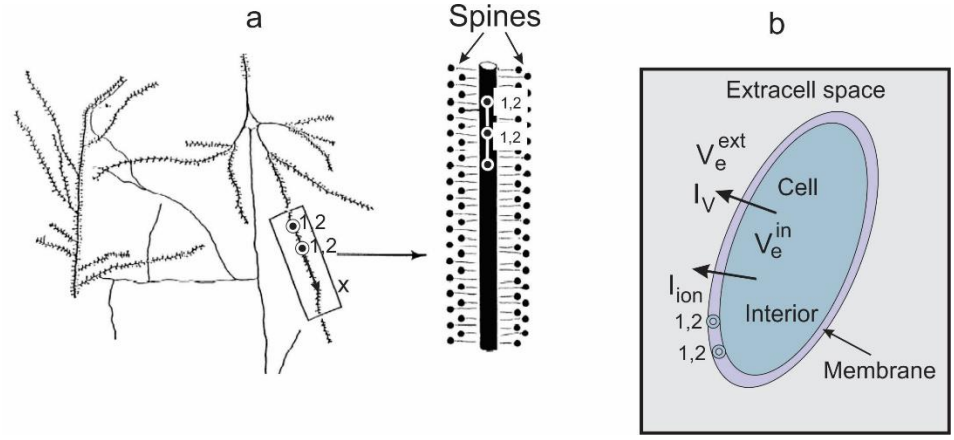

Fig. 21. Schematic of nerve fibers and cells. a) Dendritic tree and 1D finite elements along the fibers with connectivity elements 1,2; b) Cell with current I_V through membrane due to potential difference membrane, and ionic current I_{ion} due to molecule flow modeled by connectivity elements 1,2.

The balance equations for axial current flow along the fibers are transformed into the continuum format, with the conductivity tensor according to (46), i.e.

$$G_{ij} = \frac{1}{A_{tot}} \sum_K G_{aK} A_K \ell_{Ki} \ell_{Kj} \tag{57}$$

where G_{aK} are axial conductivities of individual fibers. The lateral flow from fibers and flow through cell membranes are modeled by connectivity elements, with balance equations of the form (41) and matrices (analogous to expressions (44)), i. e.

$$M^e_{11} = M^e_{22} = -M^e_{12} = -M^e_{21} = C_m A_{mem}$$
$$K^e_{11} = K^e_{22} = -K^e_{12} = -K^e_{21} = G_m A_{mem} \tag{58}$$

where A_{mem} is the surface area belonging to nodes 1,2, either from a fiber surface or from a cell membrane. This surface is related to the volumetric fraction of the domain according to (49). Additionally, there is a source term in the balance equation due to ionic current I_{ion} for a node J, as

$$Q^e_{VJ} = A_{memJ} I_{ionJ} . \tag{59}$$

Regarding the electrical potential within a continuous media, the fundamental continuity equation can be derived for electrostatics from Maxwell's equations as

$$-\varepsilon \frac{\partial}{\partial t}\left(\frac{\partial^2 V_e}{\partial x_i \partial x_i} \right) = G_i \frac{\partial^2 V_e}{\partial x_i \partial x_i} + q^V_e , \quad sum\ on\ i:\ i = 1,2,3 . \tag{60}$$

where ε is dielectric constant; G_i are conductivities in coordinate directions x_i; and q^V_e is a source term (due to ion flux). This equation can be transformed into the FE format [59] so that the balance equations has the following form

$$\left(\frac{1}{\Delta t} M_{IJ} + K_{IJ} \right) \Delta V^{(i)}_{eJ} = \left(\frac{1}{\Delta t} M_{IJ} + K_{IJ} \right) V^{(i-1)}_{eJ} + Q^V_{eI} + Q^{ext}_{eI} , \tag{61}$$

where Q^{ext}_{eI} are external effects to the element, and

$$M_{IJ} = \varepsilon \int_V \frac{\partial N_I}{\partial x_i} \frac{\partial N_J}{\partial x_i} r_V dV , \quad K_{IJ} = G_i \int_V \frac{\partial N_I}{\partial x_i} \frac{\partial N_J}{\partial x_i} r_V dV , \quad sum\ on\ i:\ i = 1,2,3 ,$$
$$Q^V_{eI} = \int_V N_I q^V_e r_V dV \tag{62}$$

In case of the continuity domain representing a network of small nerve fibers, we have:

$$M_{IJ} = 0, \quad K_{IJ} = \int_V G_{ij} \frac{\partial N_I}{\partial x_i} \frac{\partial N_J}{\partial x_j} r_V dV , \quad sum\ on\ i, j:\ i, j = 1,2,3 , \tag{63}$$

In summary, the main characteristics of the composite smeared finite element (and the corresponding FE model) for electrical potential within a biological system are as follows:

- Large nerve fibers (big axons) are modeled by 1D finite elements, connected to a network of small fibers
- Small fiber network is represented by a continuum with the corresponding volumetric fraction and conductivity tensor (57); the balance equation is (61) with the element matrices (63)
- Continuum domains include: extracellular space, different groups of cells, and organelles within cells. They occupy the volumetric fractions r_V-s of the element, and the balance equations (61) include matrices and source term (62)

- Lateral current flow from fibers and through membranes of cells and organelles is modeled by 1D connectivity elements with matrices (58) and source terms (59)

The data necessary for the smeared model consists of the geometrical part associated with the FE nodes: volumetric fractions r_V^J, area coefficients r_{AV}^J, volumes V^J belonging to nodes, wall or membrane thicknesses, geometric characteristics of the fiber network; and material data, which also can be associated with the FE nodes: conductivities - within fibers, through membranes and within continuum domains, dielectric constants, capacitances of walls and membranes, characteristics of the ionic currents through membranes.

3.1.4 Smeared model for ionic transport

Gradient driven transport of charged molecules (ions)/particles in a continuum space or through biological membranes is affected by the field of electrical potential. Also, the ions change the field of electrical potential, therefore there exists a coupling between ion transport and concentration, and the electrical field. Here, we first summarize the fundamental equations in this physical problem and then present a smeared FE methodology for computational modeling.

The mass flux J_i in direction x_i of ions m has a part corresponding to diffusion and, additionally, a part due to the electrical force based on the Nenrst-Plank equation; and can be expressed as [55]

$$J_i^m = -D\frac{\partial c^m}{\partial x_i} - \frac{Dz^m F}{RT} c^m \frac{\partial V_e}{\partial x_i}, \tag{64}$$

where D is diffusion coefficient, z^m is molecule valence, F is the Faraday constant, T is absolute temperature, and c^m is concentration. Then the mass balance equation is

$$\frac{\partial c^m}{\partial t} = \frac{\partial}{\partial x_i}\left[D\frac{\partial c^m}{\partial x_i} + \frac{Dz^m F}{RT} c^m \frac{\partial V_e}{\partial x_i} \right], \quad sum\ on\ i:\ i=1,2,3, \tag{65}$$

The FE balance equation which follows from this equation has the form (59) for the concentration field, with the source term due to electrical effects

$$Q_I^{mE} = \frac{DFz^m}{RT}\int_V N_I \frac{\partial}{\partial x_i}\left(c^m \frac{\partial V_e}{\partial x_i} \right) r_V^K dV, \tag{66}$$

This source term can be evaluated as follows:

$$Q_I^{mE} = Q_I^{mE1} + Q_I^{mE2}, \tag{67}$$

where

$$Q_I^{mE1} = \frac{DFz^m}{RT}\int_V N_I \frac{\partial c^m}{\partial x_i}\frac{\partial V_e}{\partial x_i} dV, \tag{68}$$

$$Q_I^{mE2} = \frac{DFz^m}{RT}\int_V N_I c^m \frac{\partial^2 V_e}{\partial x_i \partial x_i} dV = -\frac{1}{\varepsilon}\frac{DF^2 z^m}{RT}\int_V N_I c^m \left(\sum_m z^m c^m \right) dV. \tag{69}$$

In the last equation the electrostatic balance of charge due to ionic charge contribution is considered, according to reference [55]. Summation in the last equation includes all ion types involved in mass transport.

The source term in equation (62) due to presence of ions within the domain can be calculated as

$$q_e^V = \sum_m z_m F \frac{\partial c_m}{\partial t}, \tag{70}$$

Next, we present the fundamental relations for ionic transport through cell membranes, following [60],[61]. The relations given below are based on the Nernst equation

$$\frac{a_i}{a_o} = e^{-N}, \quad N = \frac{zFE}{RT}, \tag{71}$$

where a_i and a_o are molecular activities on the two sides of the membrane ('inside' and 'outside'). Assuming linear distribution of the gradient of electrical potential across the membrane thickness, the flux through the membrane can be expressed as

$$J = J_n + J_d = P_n(a_{on} - a_{in}) + P_d \frac{N}{e^N - 1}(a_{od} - a_{id}e^N) \tag{72}$$

where indices '*n*' and '*d*' stay for neutral and ionized forms of molecules for fluxes J_n and J_d, permeability coefficients P_n and P_d, and molecular activities. The steady state of the electrical field is assumed. Activations can be related to the concentration of molecules *c* as

$$a_n = f_n c, \qquad a_d = f_n k_{pH} c \tag{73}$$

where f_n and k_{pH} are material constants which take into account chemical and electrochemical characteristics of the transported molecules (details are given in [60],[61]). Substituting (73) into (72) and using material properties at both membrane sides, the expression for the molecular flux can be expressed as

$$J = P_n f_n (c_o - c_i) + P_d \frac{N}{e^N - 1} f_n (k_{pH}^o c_o - e^N k_{pH}^i c_i) \tag{74}$$

where k_{pH}^o and k_{pH}^i are constants at the two sides of the membrane.

The relation (74) leads to formulation of the diffusion matrix for the membrane connectivity element. The matrix terms in equation (63) are now

$$\begin{aligned} K_{11} = -K_{21} &= A_{mem}\left(P_n f_n + P_d \frac{N}{e^N - 1} f_n k_{pH}^0 \right) \\ K_{22} = -K_{12} &= A_{mem}\left(P_n f_n + P_d \frac{Ne^N}{e^N - 1} f_n k_{pH}^i \right) \end{aligned} \tag{75}$$

where A_{mem} is the membrane surface belonging to a FE node, according to eq. (66).

We note that the composite smeared finite element contains field of concentration of each ion and for each domain. A practical computational procedure in modeling the coupled problem

between electrical field and ionic concentration is implemented in our FE software package PAK [62] with the following steps:

1) Electric potential field is determined using concentration distribution from the end of previous step, for all ion types.
2) Concentration field of each molecule is calculated using the electrical potential from step 1.

Steps 1 and 2 are repeated until differences in solutions for both electrical potential and concentration of ions satisfy the adopted convergence criteria.

3.1.5 Discussion – reference to other computational models

In this section we compare the introduced smeared model with other computational models available in literature. Electrophysiology, as well as particulate/molecular transport, has long been the subject of experimental and theoretical research. Various numerical models, starting with analytical to today's modern computational models, have been formulated and implemented. Here we refer mainly to the models related to heart electrophysiology and emphasize novel features of our smeared models important for applications.

Initial models of cardiac electrophysiology rely on the seminal work of Hodgkin and Huxley [63]. In reviews [64,65] monodomain and bidomain models of tissue, connected to the basic cell models, are presented for heart electrophysiology. A critical analysis regarding practical applications of these models is given in [66], with particular reference to the format of data preparation, as CellML and software simulator Chaste [67]. The approach that most resembles our smeared models in principle, is the so-called bidomain model introduced decades ago [68-71] derived from discrete models by using homogenization procedures. The bidomain model was further extended to a model with two types of cells, called the extended bidomain model [72]. The governing balance equations of the three continuum domains (extracellular space and two cell types) in [72] are derived according to the ohmic conduction law using the conductivity/resistance characteristics of each domain. Additionally, the terms corresponding to membrane conduction and ionic currents I_{ion} between the three domains are included. These membrane terms take into account the membrane conduction and capacitance properties, and the corresponding area-to-volume ratios. The FE nodal variables consist of the potentials of the three continuum domains.

For purposes of comparison to our model, we show here the fundamental equations of reference [72] using our notation. For the three domains, cell group 1, cell group 2, and extracellular space, the equations are (terms not important for our analysis: stimulus current and gap effects, are omitted)

$$
\begin{aligned}
&-r_{AV}^{(1)}\frac{\partial}{\partial x_i}\left[C_m^{(1)}\left(\frac{\partial V_e^{(1)}}{\partial t}-\frac{\partial V_e^{(ext)}}{\partial t}\right)+I_{ion}^{(1)}\right]+\frac{\partial}{\partial x_i}\left(G^{(1)}\frac{\partial V_e^{(1)}}{\partial x_i}\right)=0\\
&-r_{AV}^{(2)}\frac{\partial}{\partial x_i}\left[C_m^{(2)}\left(\frac{\partial V_e^{(2)}}{\partial t}-\frac{\partial V_e^{(ext)}}{\partial t}\right)+I_{ion}^{(2)}\right]+\frac{\partial}{\partial x_i}\left(G^{(2)}\frac{\partial V_e^{(2)}}{\partial x_i}\right)=0\\
&\frac{\partial}{\partial x_i}\left(G^{(1)}\frac{\partial V_e^{(1)}}{\partial x_i}\right)+\frac{\partial}{\partial x_i}\left(G^{(2)}\frac{\partial V_e^{(2)}}{\partial x_i}\right)+\frac{\partial}{\partial x_i}\left(G^{(ext)}\frac{\partial V_e^{(ext)}}{\partial x_i}\right)=0
\end{aligned}
\qquad (76)
$$

where the upper indices 1 and 2 correspond to the first and second group of cells, while 'ext' stands for the extracellular space. These equations are then transformed to the FE format in a standard Galerkin weighting procedure used above [59], and integration is performed over the entire domain volume.

We further summarize differences between our smeared model and the bidomain or the extended bidomain model (called further as the previous models). Also, we emphasize our new formulations.

1. Considering electrophysiology, the first and fundamental difference between previous models and our smeared models is that the previous models are case sensitive, while ours are general. The previous models rely on the apparent material properties of the entire tissue, while our models use the true material parameters, independent on the tissue composition. This difference comes from the assumptions used in the derivation of the governing balance equations. In the previous models, these equations (e.g. equations (76)) are derived by homogenization over the entire tissue volume, including cell membranes, through the area factor r_{AV} and continuity conditions at the membranes [71]. Integration is therefore performed over the entire domain, without including the participation of volumetric fractions of the individual constituents (compartments). This represents a significant drawback which can be illustrated in the following simplified example: Assume we have a current flow to a closed domain composed of different types of cells and extracellular space, separated by membranes, with their own conductivities and dielectric constants. The electric charge and potential within each of the constituents must depend on their respective volumetric fractions. Therefore, the traditional models practically deal with the apparent material parameters which depend on the structural composition of the tissue. On the other hand, our smeared models consider the entire medium as a composite where a compartment *K* occupies the volume specified by volumetric fraction r_V^K, and the balance equations are set by using the true material parameters of that compartment. No additional condition is employed and the equations are independent of the tissue composition. The compartments considered here include: large vessels, large neural fibers, capillary network, small neural fibers, extracellular space, and different groups of cells composed of cytosol and organelles. The spatial numerical integration goes over the $r_V^K V$ occupied by the compartment *K*. For organelles, both in diffusion and in electrophysiology, the volume fraction has a hierarchical character, i. e. for a cell group *N*,

$$V_N^k = r_V^k r_V^N V \tag{77}$$

where r_N^k is the relative volume ratio of the organelle with respect to the cell volume, whose ratio r_V^N is related to the finite element volume *V*. Accuracy of our smeared models is assessed by comparison to the detailed FE models of a composite tissue, given here and in our previous publications [50,53,54].

2. A significant novelty of the smeared model is the representation of a 1D processes (e.g. fluid flow, diffusion, electric conduction within a fiber-like domains) by continuum equations with a consistent transport tensor (46); and integration goes over the CSFE volume occupied by the 1D network space. This approach was initially introduced in our cited references for convective and diffusive transport, along with the demonstration of the accuracy of solutions, and herein is applied to electrophysiology. The entire His-Purkinje system of the heart [71] can be modeled using our smeared continuum representation in a way analogous to modeling a capillary network [50]. Our model has a significant distinction with respect to,

for example, the model in [74] which is based on the bidomain formulation and averaging over the fiber cross section.

3. The electrostatic equations (60) used in our formulation are more general than those in (76), since they take into account the rate of change of the potential (the term on the left- hand side), which previous models omit.
4. Formulation of the connectivity elements between different physical fields is a unique feature of the smeared models. These elements are particularly suitable for including specificities of the membranes (cells, organelles) and vessel walls such as partitioning at the membrane/wall common surface with the continuum, or material nonlinearities in case of transport or electric conduction. The inclusion of gap junctions between cells, introduced in [72] and [75], or the condition that connections between Purkinje fibers and tissue occurs at the fiber ends, is straightforward by employing the appropriate connectivity elements. Also, ionic currents due to ion flow through membrane channels (I_{ion}) [76] can be included in these elements, as well as transport of specific molecules such as calcium. Geometrical terms related to the connectivity elements are described above (equations (48-50)). There are also important features of the connectivity elements regarding the convergence rate during equilibrium iterations at the global level – the matrices of these elements have a so-called tangent character for improved convergence [59]. These elements are also computationally efficient, since they do not require numerical integration (as needed in implementation of equations (76) in traditional models).
5. A 1D finite element is introduced to model current flow which includes current conduction along a neural fiber and lateral loss of electrical charge through the fiber surface. The FE formulation is based on cable theory and the element accuracy is assessed by comparison to analytical solutions; details provided in Appendix 8.1. This element is formulated for modeling electrical signal transmission along large axons, however it is also applicable for modeling smaller neural fibers such as in case of Purkinje network within the heart. Our concept is straightforward and simple (with demonstrated accuracy) when compared to ref. [74], where a complex homogenization procedure was employed to couple 1D signal propagation within the Purkinje network to a bidomain continuum model of the heart tissue.
6. Another novelty introduced is our procedure for bidirectional coupling of the ionic transport and electrical field. In the continuous domains (extracellular space, cell interior, organelles) this procedure relies on equation (65) which is transformed to the FE framework. Also, the coupling is included into our connectivity elements, following formulation given in [60]. The presented methodology is suitable and straightforward for general applications at the organ level, as demonstrated by the presented examples.

There are a number of issues, not mentioned above, that are important when considering electrophysiology and coupling to other physical fields in living organisms, for which the smeared methodology can be effectively applied. For example, procedures that improve computational efficiency of the monodomain and bidomain models, e.g. with specific solution algorithms, or analysis of stochasticity in the heart electric signal propagation dynamics, can be implemented into our smeared models. Finally, coupling electrophysiology to the mechanics of muscles, including multiscale muscle models, can be efficiently implemented into our smeared models.

3.1.6 Membrane currents according IORD model

Accumulated current density (IORd) in cell membrane is calculated according ORd model [36], and added to equation (40) of the FE solution procedure. Currents of ORd model which affects concentration of the Ca^{2+} in myoplasmic compartment are: I_{pCa}, I_{Cab} and $I_{NaCa,i}$; while current

which affects concentration of Ca^{2+} in the subspace compartment are I_{CaL} and $I_{NaCa,ss}$. Mean current density I_{Ca} for transport of the Ca^{2+} ions can be calculated as:

$$I_{Ca} = -\left(I_{pCa} + I_{Cab} - 2\cdot I_{NaCa,i}\right)\frac{V_{myo}}{V_{myo}+V_{ss}} - \left(I_{CaL} - 2\cdot I_{NaCa,ss}\right)\frac{V_{ss}}{V_{myo}+V_{ss}} \quad (78)$$

where V_{myo} and V_{ss} are volumes of the myoplasmic compartment and subspace compartment, respectively. Mean concentration in cells, $\left[Ca^{2+}\right]_{mean}$, is calculated as average concentration in cells composed of: myoplasmic (denoted by index "*i*"), subspace ("*ss*"), network SR ("*nsr*"), and junctional SR ("*jsr*") compartments, according to [36], i.e.

$$\left[Ca^{2+}\right]_{mean} = \left(\left[Ca^{2+}\right]_{i}\cdot V_{myo} + \left[Ca^{2+}\right]_{ss}\cdot V_{ss} + \left[Ca^{2+}\right]_{nsr}\cdot V_{nsr} + \left[Ca^{2+}\right]_{jsr}\cdot V_{jsr}\right)/V_{cell} \quad (79)$$

where $V_{myo} = 0.68\,V_{cell}$, $V_{ss} = 0.02\,V_{cell}$, $V_{nsr} = 0.0552\,V_{cell}$ and $V_{jsr} = 0.048\,V_{cell}$. Concentrations of Ca^{2+} in each compartement (*i*, *ss*, *nsr* and *jsr*) of ORd model are calculated according to equations provided in Suplementary of Reference [36].

3.1.7 Numerical examples

Several examples are selected, according ref. [43]. The purpose of these examples is to demonstrate applicability, accuracy and efficiency of the presented smeared modeling methodology. The basic idea is to show accuracy considering electrical signal transfer from nerve fibers to extracellular space and further to cells. The connection between nerve fibers and cells in the model goes via extracellular space which also represents the fiber-cell junctions present in the biological systems. The first example is designed with an electrical gradient across the field. Other examples assume a small isolated region of tissue with prescribed potentials within nerves. Isolated tissue domain means that gradients with respect to the surrounding domain are neglected. The last example includes ionic transport coupled with the field of electrical potential.

3.1.7.1 A tissue domain with electrical potential gradient

A square tissue domain is shown in Fig. 22. It is assumed that there is a nerve fiber network,

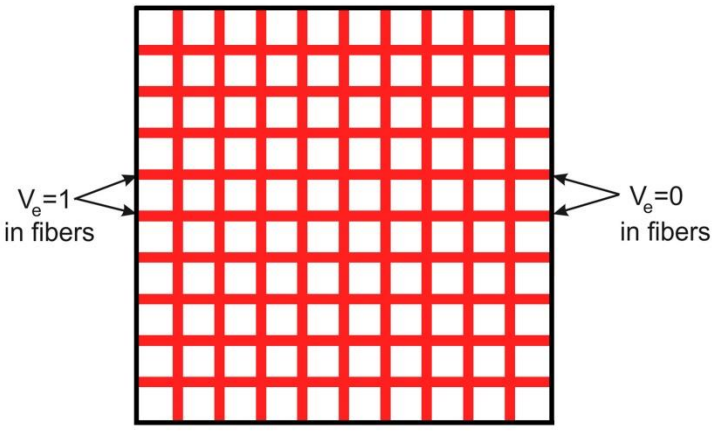

Fig. 22. A square tissue domain (10x10 mm) with network of nerves (in red) connected with tissue. Prescribed constant electrical potential at the two boundaries.

with given constant potential at two boundaries, while the lateral boundaries are impermeable both for tissue and fibers. The data used in the model are

Fiber diameter:	0.25 mm	Volume fraction: r_V=	0.35 (35%)
Membrane conductivity:	0.1 S/mm^2	Capacitance:	0.1 F/mm^2
Conductivity: Fibers:	1 S / mm	Tissue:	2 S / mm
Dielectric constant:	0.1 F/mm		

In Fig. 23 are shown mean potentials developed over time for the tissue and for the fiber domain, obtained by using the detailed model (1D elements for fibers, 2D elements for tissue, and connectivity elements for fiber lateral currents) and the corresponding smeared model (number of potentials at FE nodes is 2 - for fiber and tissue domain). There are some differences, as expected, due to gradients in both fiber and tissue domains. As will be seen in the subsequent examples, this difference is smaller when there is no gradient within fibers (which is physiologically more realistic). Also, the goal of the examples here is to demonstrate accuracy of transport from capillary system to cells or signal propagation from nerve network to cells. Effects of the gradients as in this example are dependent on the model size, which here are not further investigated.

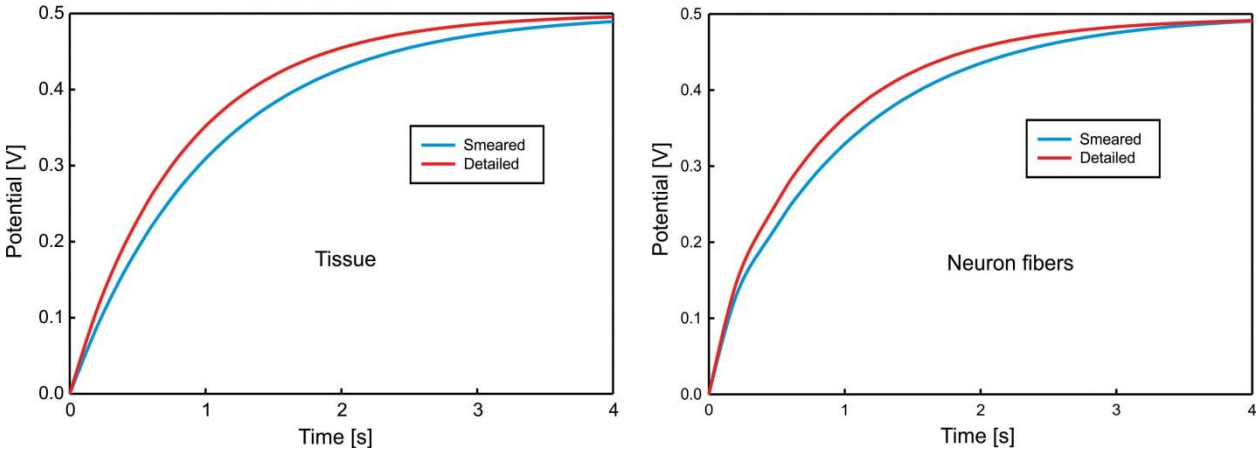

Fig. 23. Mean potential in nerve fibers (left panel) and in tissue (right panel) evolution over time. Prescribed potential in fibers at boundary (Fig. 22).

3.1.7.2 A tissue domain with cells and organelles

Here, we consider an isolated 2D tissue domain with two groups of cells and with three organelles within each group, shown in Fig. 24. Cells have different material parameters and volumetric fractions. It is assumed that six nerve fibers are present (normal to the 2D space), with prescribed potentials as function of time. Three cases of prescribed potential are used – constant, bolus, and as in Purkinje fibers in heart.

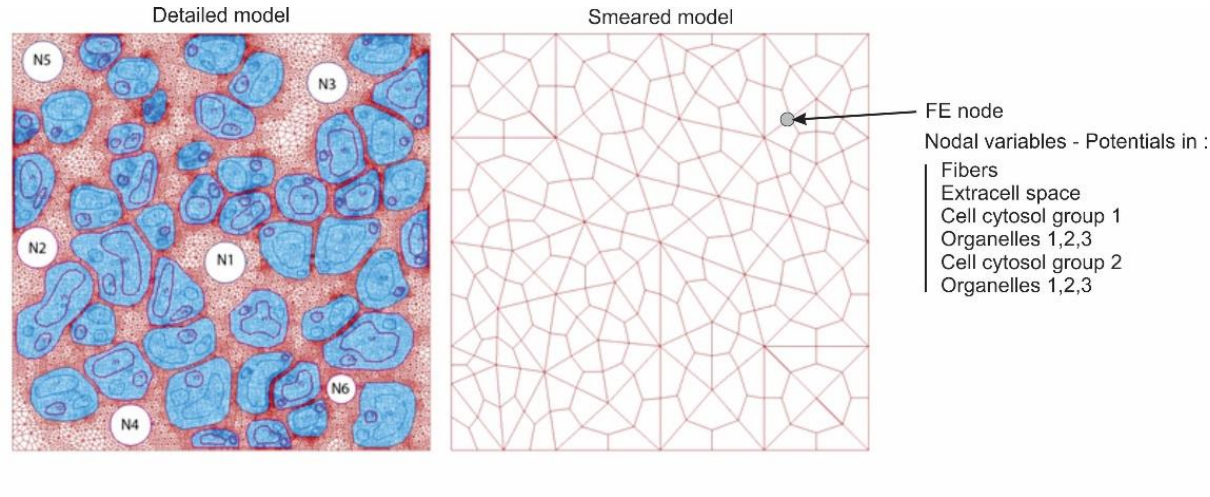

Fig. 24. A tissue domain of size (50 x 50 µm) with cells and nerve fibers (N1 to N6) normal to the plane. Detailed model with 2D elements (left panel) and smeared model (right panel).

The data used in the models are given below (units: length µm, potential V, conductivity S/µm, membrane conductivity S/µm^2, capacitance F/ µm^2):

Geometry

Nerve fibers	(33):	Mean diameter	4.76	Volumetric fraction	0.043
Cell group 1	(51)		6.30		0.307
Organelle 1			3.64		0.334
Organelle 2			1.16		0.334
Organelle 3			1.10		0.031
Cell group 2	(48)		6.16		0.260
Organelle 1			3.17		0.270
Organelle 2			1.39		0.051
Organelle 3			1.46		0.057

Material data

Extracell and fibers	Conductivity	10^{-7}	Membrane conductivity	$4{\cdot}10^{-12}$	Capacitance 10^{-14}
Cell 1 and organelles		10^{-7}		$4{\cdot}10^{-10}$	10^{-12}
Cell 1 and organelles		10^{-7}		$4{\cdot}10^{-12}$	10^{-14}

Initial values:

E=0 in extracellular space, -0.07 in cells, -0.05 in organelles

The detailed model consists of 2D elements used for all continuum domains and also for all membranes of cells and organelles, with prescribed potential at the surfaces of the nerve fibers. In the smeared model we have 2D elements only, which include nerve fibers, all continuum domains and membranes, with 10 nodal potentials as nodal variables (depicted in Fig. 24). Note that all membranes and the surface of the fibers are modeled by connectivity elements (with no additional nodal variables). For the insight into difference in model size of the two models we give the number of equations of the system to be solved: 69457 for detailed model, 1089 for smeared model. Besides the enormous difference in effort to prepare two models, the size of the models and therefore the computational difference is of the order of 10^2.

3.1.7.2.1. Constant potential in fibers

It is assumed that the potential within fibers is constant and equals to 0.08V. We use a small value for prescribed potential in order to detect differences in domains with micron size.

The potential fields for three different time points, for detailed and smeared model, are shown in Fig. 25. It can be seen that the uniform fields of the smeared model agree with the corresponding domains within the detailed model.

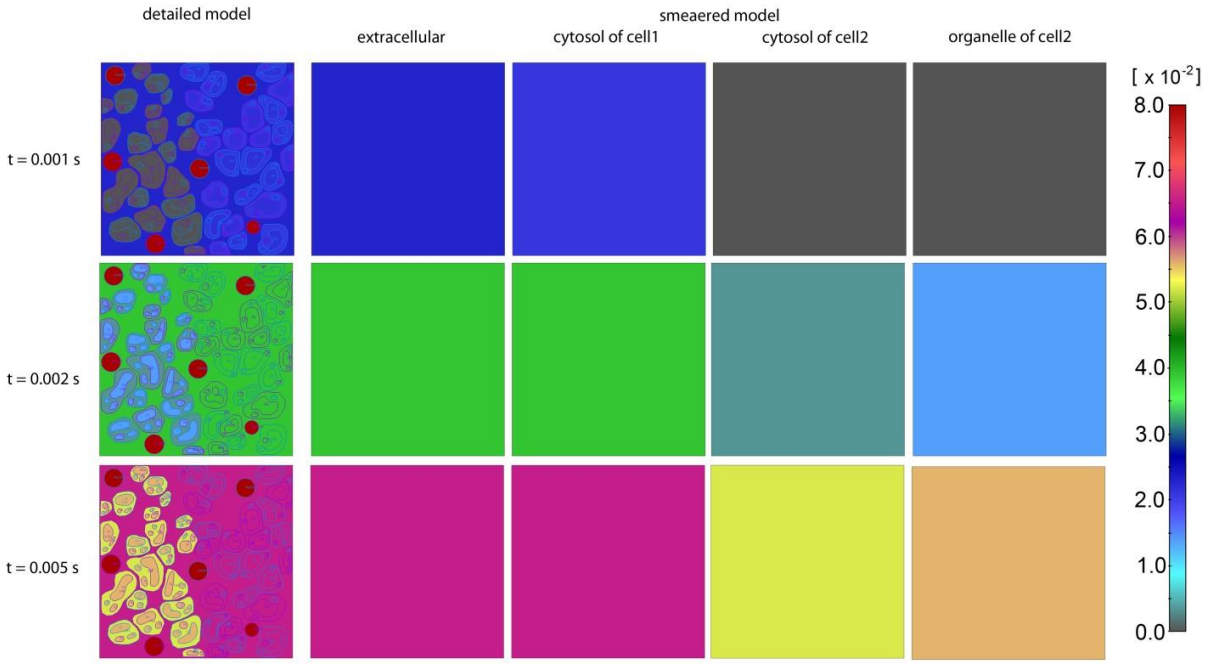

Fig. 25. Fields of electrical potential in case of constant potential of 0.08V within nerve fibers. Three time points (t = 0.001, 0.002 and 0.005s) and several domains, detailed and smeared model (extracellular space, cytosols of cell 1 and cell 2, and organell of cell 2).

The evolution of the mean potential for several domains is shown in Fig. 26, demonstrating very high degree of agreement. This is expected since the potential fields in the detailed model are practically uniform for each spatial domain. Some delay can be noticed in potential evolution within cells, and particularly within organelles in the cell group 2 due to smaller membrane conductivity for this organelle.

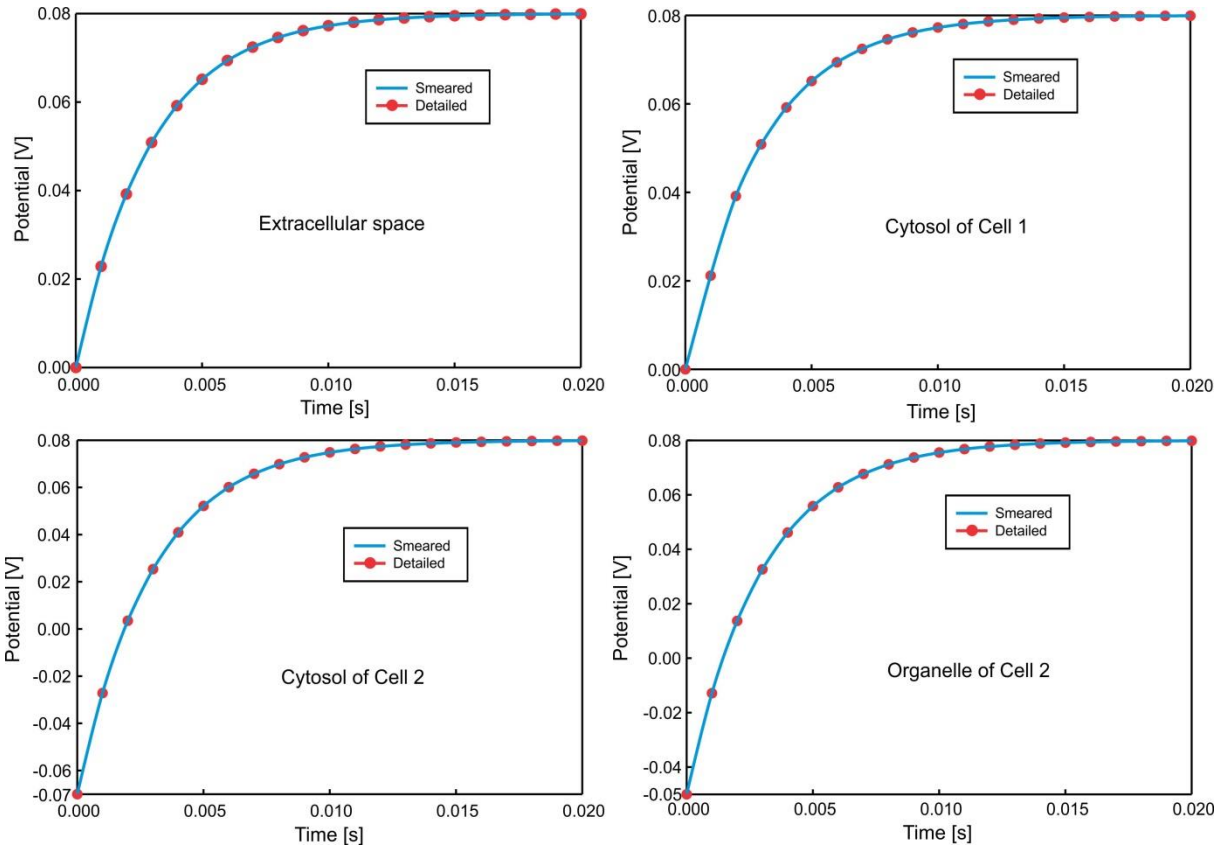

Fig. 26. Evolution of the mean potential in case of constant potential of 0.08V within nerve fibers. Four domains, detailed and smeared model.

3.1.7.2.2. A bolus function for potential in fibers

It is assumed that a bolus-type function is given within nerve fibers, as shown in Fig. 27.

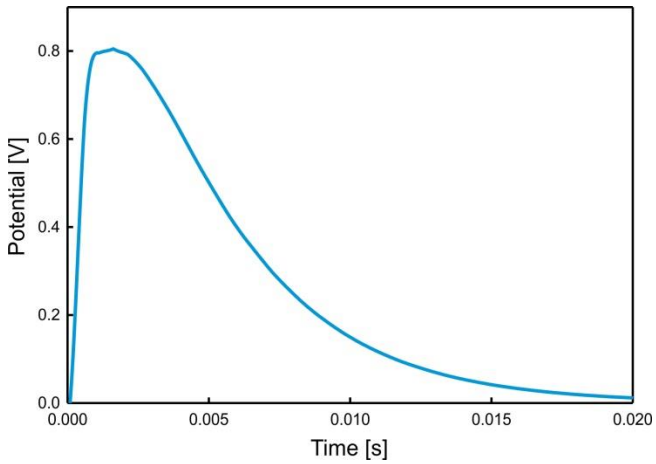

Fig. 27. A bolus-type prescribed electric potential in nerve fibers

The evolutions of the potential within different domains computed by either model are practically the same, Fig. 28. As in the case of constant potential, there is a small time delay and difference from the prescribed potential within nerve fibers, due to membrane resistances.

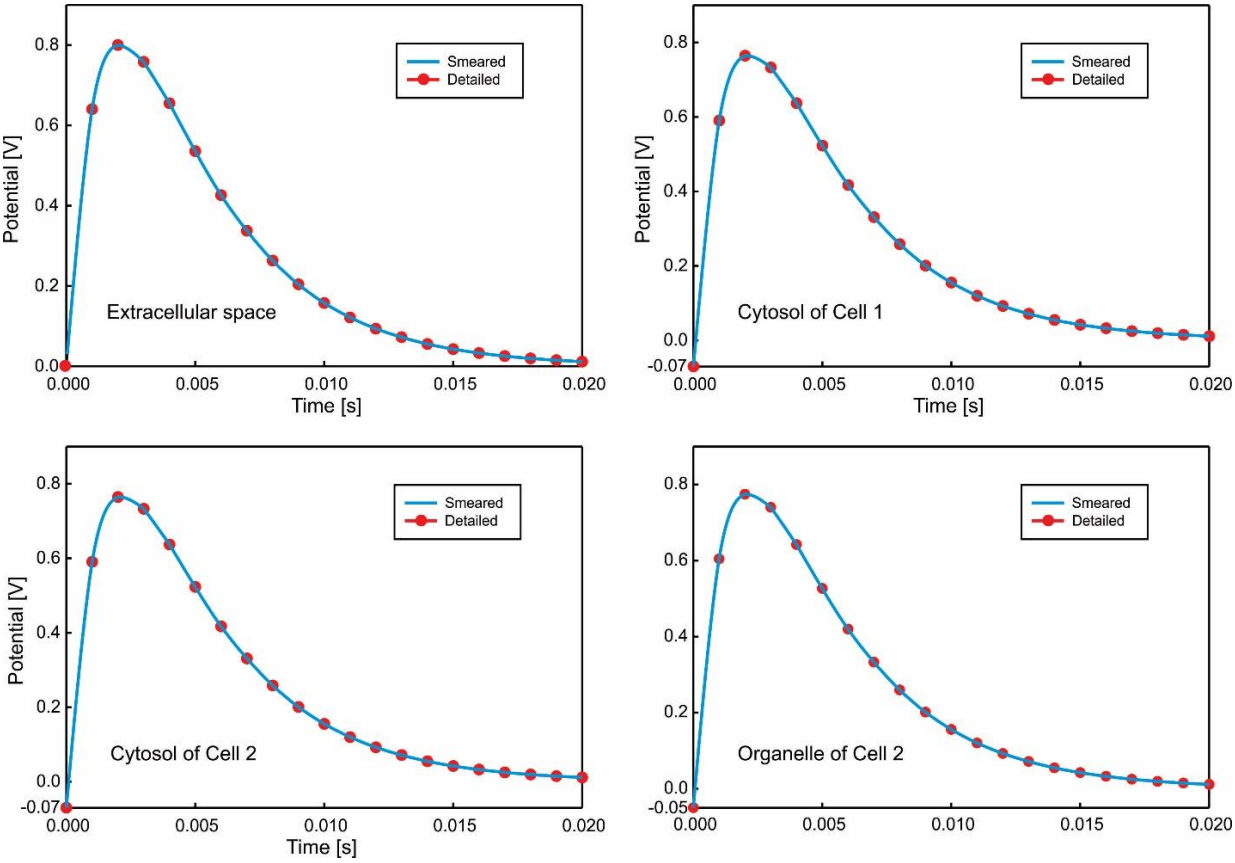

Fig. 28. Electric potential vs. time for detailed and smeared model within different domains for bolus function in Fig. 20 within fibers.

4.3.7.2.3. A function as in Purkinje fibers

Finally, here we use the function for prescribed potential as in the Purkinje fibers of the heart [76]. Due to the high value of the potential within the fibers, the potentials in all domains are practically as in the fibers, and are the same when using either one of the two models. The evolution of the potential in any of the domains is as shown in Fig. 29.

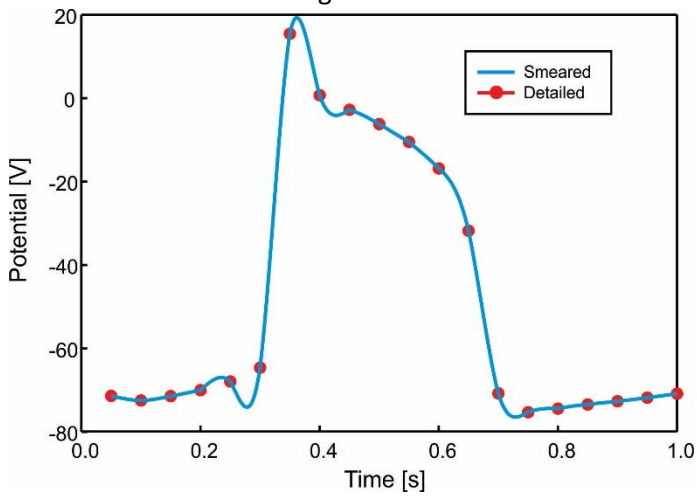

Fig. 29. Electrical waveform within Purkinje fibers of the heart [15]

4.3.7.2.4. Model with potassium and sodium currents included

Here we include into the model currents through cell membranes due to potassium and sodium flow through the membranes (in eq. (56)). Details of the calculation of these currents are given in the

Appendix 8.2. We use values of potential corresponding to the last equilibrium iteration, hence it is an Euler backward integration scheme. It is assumed that the potential in nerve fibers is constant and equal to 0.08V.

Electrical potential field for four time points and for the detailed model is shown in the first row of Fig. 30. It can be seen that the potentials in the interior of cells are different in the two groups due to different material properties. In the second row we display the potential field for cell interior of group 2. It can be seen that there is agreement between the two models.

Graphs for the change of the mean potentials over time within different domains are shown in Fig 31. The effect of ionic currents can be noted – the ultimate values of potentials are: 0.6V for extracellular space, 0.08V for cells (as is prescribed in fibers). The potential within extracellular space is higher than in cells due to outward net ionic current flow.

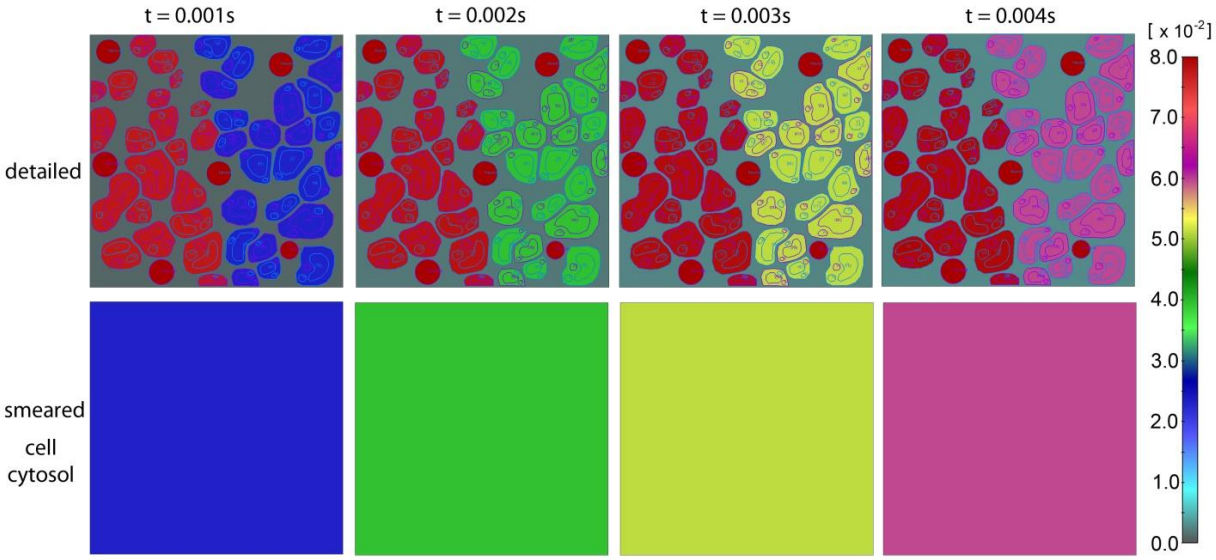

Fig. 30. Fields of electrical potential in case of ionic currents of potassium and sodium included; detailed model – upper panel, smeared model –lower panel.

Graphs for the change of the mean potentials over time within different domains are shown in Fig. 31. The effect of ionic currents can be noted – the ultimate values of potentials are: 0.6V for extracellular space, 0.08V for cells (as is prescribed in fibers). The potential within extracellular space is higher than in cells due to outward net ionic current flow.

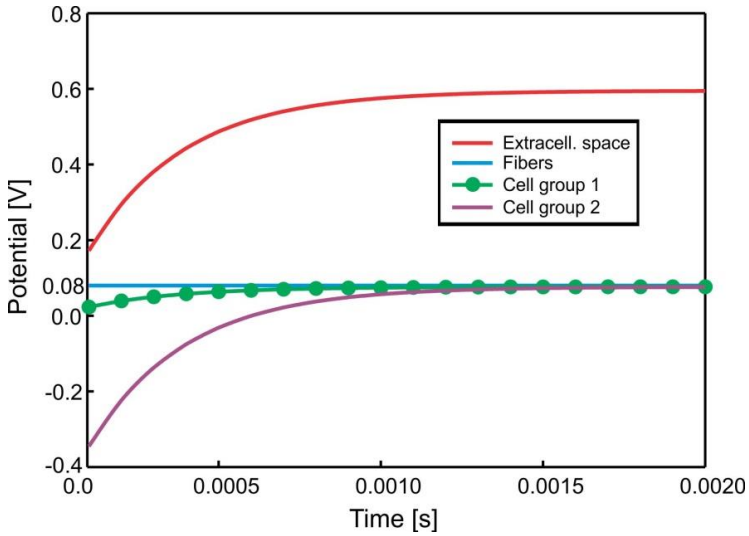

Fig. 31. Evolution of the mean potential in extracellular space and cells, with ionic currents of potassium and sodium included. Solutions for detailed and smeared model are practicaly the same.

3.1.7.3 Model with coupled diffusion of ions and electrical flow

In this final example, we consider coupled electrical and concentration fields. The same model as in Fig. 24, but now additionally with five capillaries C1…C5, are shown in Fig. 32. Nodal variables include concentrations in all domains except in nerve fibers, while the potential field is present in all domains except in capillaries. Here, a structural mesh is used for the smeared model to demonstrate that this simple mesh can also provide accurate results. Number of equations for detailed model is 72458 and for smeared model is 1200.

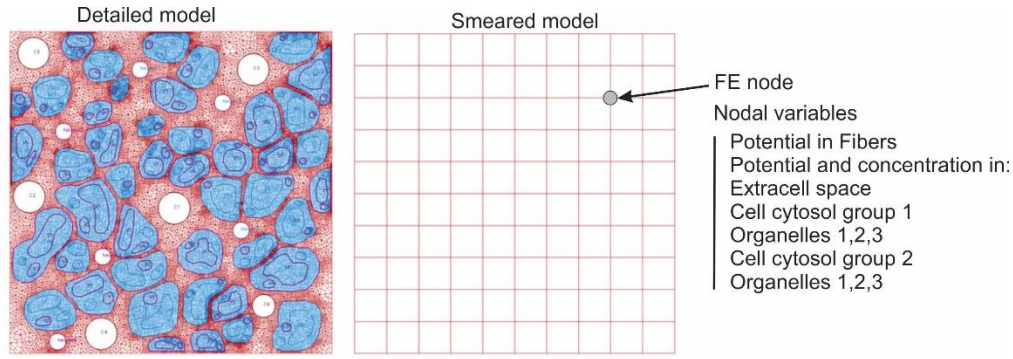

Fig. 32. Detailed and smeared model for coupled electrical flow and ionic diffusion.

The same data as for Example 3.1.7.2 is used for the electrical field, while for diffusion the material data are as follows:

Diffusion coefficient is the same for all continuum domains: 10^3 μm^2/s

Diffusion coefficients for membranes are also the same for all continuum domains: 10^3 μm/s,

Partitioning coefficients: P = 10 at cell membrane of cell group 2, and P = 10 at organelle membrane of cell group 2.

Coefficients P_n, P_d, k_{pH}^o , k_{pH}^i and f_n are equal for all cells and organelles: $P_n = P_d = 1$, $k_{pH}^o = k_{pH}^i = 10^{-6}$, $f_n = 1.2382$.

Bolus-type function is used as in Fig. 27 for both electrical potential (maximum is 0.8 V) within nerve fibers and for concentration in capillaries (maximum is 10^{-4} mg/μm^3).

Concentration and electrical potential field, obtained by the detailed model, at time 1s, is shown in Fig. 33. Differences in concentration between the two groups of cells are notable due to partitioning P=10 for cell group 2. Mean concentration and electrical field evolution, obtained by the two models, are shown in Figs. 34 and 35, respectively. It can be seen, as in previous examples, that there is good agreement between the two models. Some differences are expected due to very non-uniform concentration and electrical potential fields. We have specified some extreme conditions within the model: two cell groups are located in separate spatial domains and with different material properties – it is taken that there is partitioning for cell and organelle membranes of cell group 2.

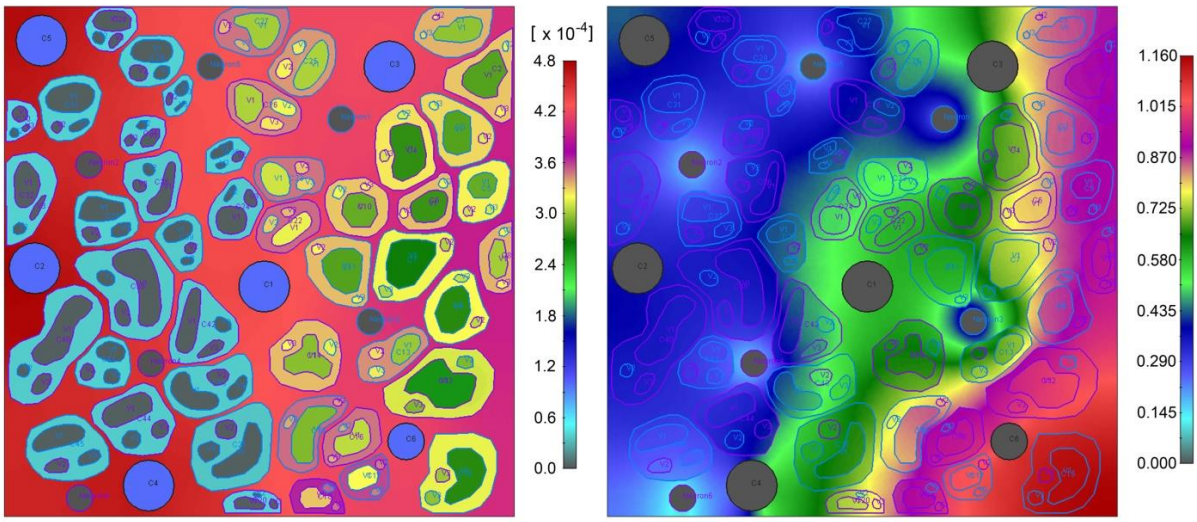

Fig. 33. Concentration (left panel) and electrical potential fields (right panel) at time t=1s, coupled diffusion and electrical flow, detailed model.

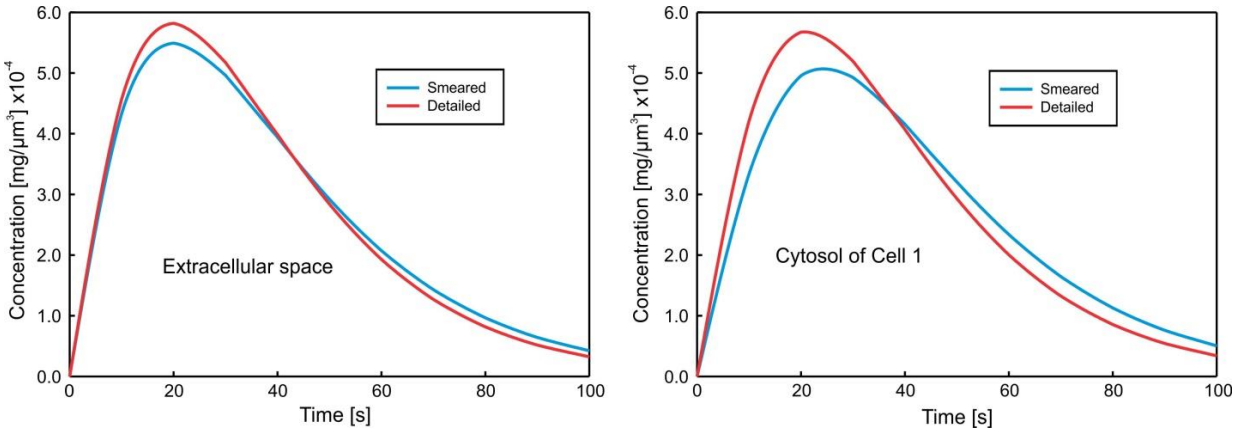

Fig. 34. Mean concentration vs. time for coupled problem, detailed and smeared model solutions, within extracellular space (left panel) and cytosol of cell type 1 (right panel).

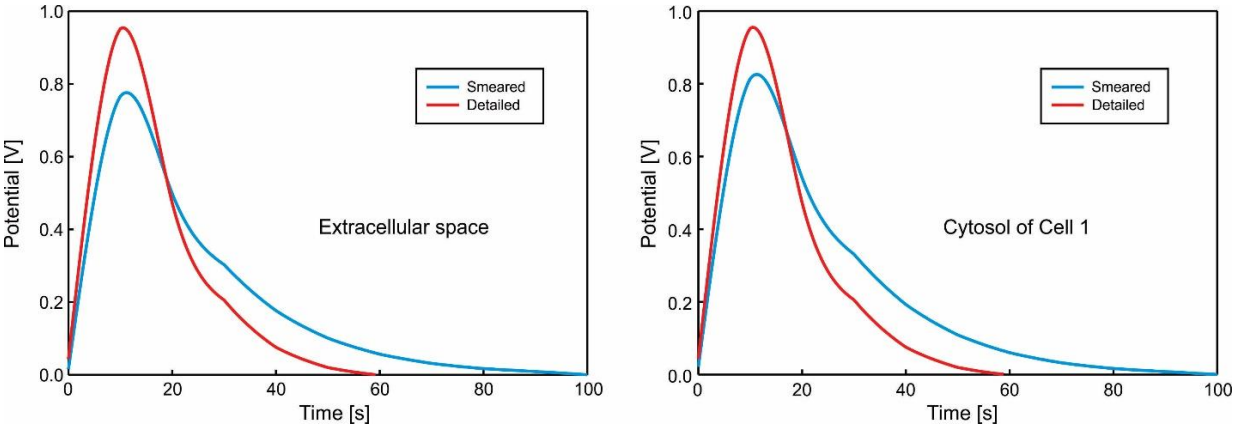

Fig. 35. Mean electrical potential vs. time for coupled problem, detailed and smeared model solutions, within extracellular space (left panel) and cytosol of cell type 1 (right panel).

3.2 Solid mechanics module in PAK

Muscle contraction occurs from the generation of active stress according to equation (55), where concentration of calcium is evaluated by our transport models (detailed and smeared). The mechanical response is calculated using the equation of motion.

3.2.1 Coupling electrophysiology and muscle mechanics

Muscles (here assumed skeletal muscles) in the body are activated by electrical signals transmitted from the central nervous system to muscle cells. The signals trigger muscle activation since they produce a change in cell membranes potentials, which further leads to flow through membrane of ions vital for cell functioning, such as potassium, sodium, calcium and others [79,80,81]. The ion flow is bidirectional through various biological mechanisms. There are a number of mathematical models which connect the membrane potential change with activation of muscles. For example, for cardiac muscle, the mathematical expressions for generation of the so-called active stress along the muscle fiber, which produces the muscle contractile force, the membrane potential is used directly [82] or through the concentration of calcium Ca^{2+} within the muscle cell [65,83,84]. The calcium Ca^{2+} is the crucial molecule which catalyzes the biochemical cycle of conformational change of muscle fiber molecules, and therefore transformation of chemical into mechanical energy. Hence, in modeling muscle mechanical action it is necessary for these models to have the calcium concentration change within muscle cells over time. We will use a widely accepted relation [83],

$$\sigma_{act} = \frac{\left[Ca^{2+}\right]^n}{\left[Ca^{2+}\right]^n + C_{50}^n}\sigma_{\max}\left[1+\eta\left(\lambda-1\right)\right] \tag{80}$$

where σ_{act} is the active stress along the fiber, Ca2+ is calcium concentration; and C_{50}^n, $\sigma_{\max}$, η and λ are material parameters.

We use velocity formulation, i.e. the nodal variables are velocities – convenient to couple solid and fluid mechanics, while stresses in solids are calculated from strains or stretches. The balance equation of a finite element can be written in the form [85]

$$\left(\frac{1}{\Delta t}\mathbf{M} + \Delta t\mathbf{K}\right)\Delta\mathbf{V}^{(i)} = \mathbf{F}^{ext} - \mathbf{F}^{\text{int}(i-1)} - \frac{1}{\Delta t}\mathbf{M}\left(\mathbf{V}^{(i-1)} - \mathbf{V}^{t}\right) \tag{81}$$

where the mass and stiffness matrices M and K have a standard form [85], and V and Vt are nodal velocities at the current (or previous) iteration and at start of time step, respectively; Fext and Fint are external and internal nodal forces. Specific to muscle deformation is that, besides the material stress dependent on the state of deformation, there exists the active stress σ_{act} entering into the internal force vector as noted above.

3.2.2 Example: Electrophysiological and mechanical model of the heart wall

In order to investigate accuracy of our CSFE model, a small sample of heart wall tissue is selected (Fig. 36) following data in [65]. From this model we extract the first layer of muscle cells in myocardium, which is close to sub-endocardium: the domain which includes the Purkinje fibers. The presented example is according to reference [86].

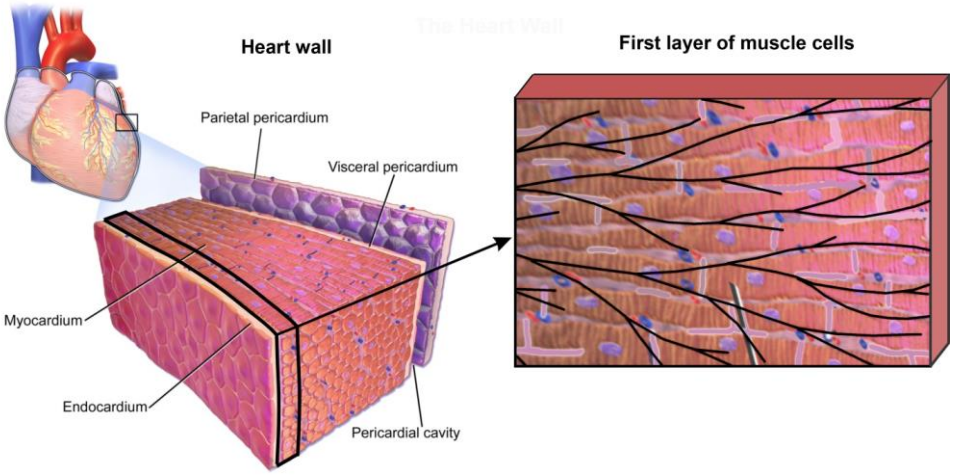

Fig. 36. Small domain of heart wall tissue taken from [65] (left panel), and first layer of muscle cells close to sub-endocardium with mesh of Purkinje fibers projected on it (right panel).

According to the image in Fig. 36b, the detailed 2D model is generated (Fig. 37a), which consists of the mesh of 1D Purkinje fibers and 25 cells. Dimension of the model is 230 x 150 μm, volume fraction of cells is r_V = 0.71 and area/volume ratio of cell is r_{AV} = 0.18. Based on the detailed model, we also generated the smeared model (Fig. 37b). Both models are used for calculation of electrical potential, calcium current and concentration. FE nodes of 1D Purkinje fibers are connected with 2D FE nodes of extracellular space domain using connective 1D elements. As shown in Fig. 37, it is assumed that left vertical boundary of the tissue is constrained to displacements in *x* direction, and lower horizontal boundary is constrained to displacements in *y* direction. We assumed that muscle fibers have longitudinal direction with respect to the muscle cells, i. e. they are aligned to the *x* direction.

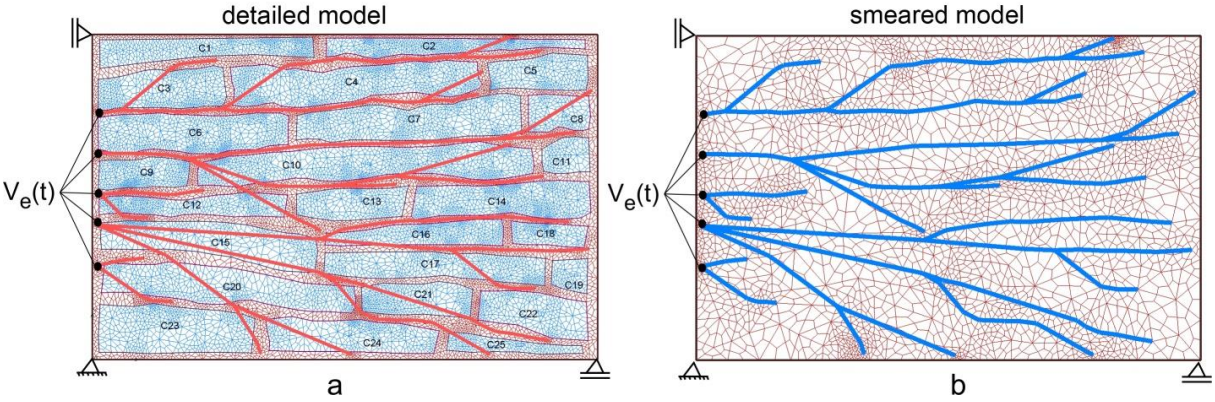

Fig. 37. a) The detailed heart wall model with cells and a network of Purkinje fibers; b) Smeared model with tissue and Purkinje fibers associated to nodes of the CSFEs in a smeared manner.

Data used in the model are: electric conductance (G_i, $i=x,y,z$) of extracellular space (further called tissue), cells and in neural fibers, is 1000 [$AV^{-1}m^{-1}$]; specific membrane conductance (C_m) of Purkinje fibers is 1000 [$S/\mu m^2$]; specific membrane capacitance of Purkinje fiber's membrane and cell membrane is 1000 [$AsV^{-1}\mu m^{-2}$], and G_m=0 for the fiber membrane. Diffusion coefficient of Ca^{2+} for tissue and cell is assumed to be 1000 [$\mu m^2/s$], while it is assumed that there is no diffusive transport though cell membrane. We used linear elastic model for heat cells and extracellular space with Young's module of 1000 MPa and Poisson ration of 0.499. Material parameters of the muscle mechanical model (eq. (53)), used in this example, are: n = 0.4, $C_{50}^n = 0.5$, $\eta = 0.2$ and $\sigma_{\max} = 100$ kPa.

The function of the electric potential is consisted of two identical cycles and is prescribed at inlet nodes of the Purkinje mesh ($V_e(t)$ in Fig. 37). We assumed constant potential inside cells (V_e = -

20 mV). Accumulated current density (I_{ORd}) in cell membrane is calculated according ORd model [81], and added to equation (40) of the FE solution procedure. For these conditions, change of mean electric potential within tissue is shown in Fig. 38a. Results are almost identical for both detailed and smeared model. Mean current density I_{Ca} for transport of the Ca^{2+} ions can be calculated as in (78). Change with time of mean current density obtained by using detailed and smeared model is shown in Fig. 38b, where I_{ca} for the detailed model is calculated as average over all cells.

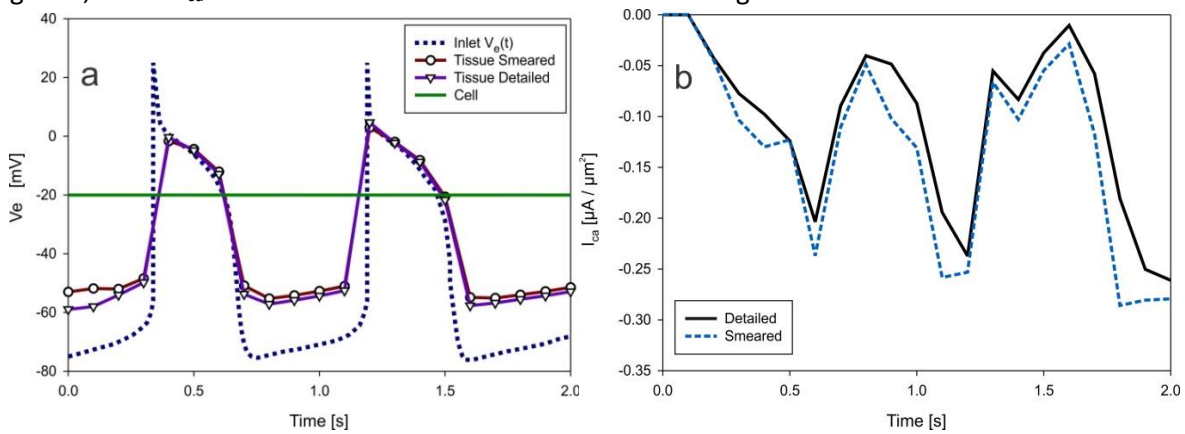

Fig. 38. a) Change of electric potential over time in extracellular space (tissue) domain - detailed and smeared model, with prescribed Ve(t) at inlet nodes of Purkinje fibers and prescribed Ve = -20V within cells (green). b) Change of mean current density Ica [μA/μm²] which affects transport of Ca2+ through cell membrane, according to detailed and smeared model.

Change of the mean concentration within cells (cell domain), for both detailed and smeared model, is shown in Fig. 39a. Muscle contraction occurs from the generation of active stress according to equation (55), where concentration of calcium is evaluated by our transport models (detailed and smeared). The mechanical response is calculated using the equation of motion (56). Mean contraction (displacement) of the right vertical tissue boundary is shown in Fig. 39b. The largest contractions occur at t = 0.9s and 1.6s, which are in accordance with the Ca^{2+} concentration within cells.

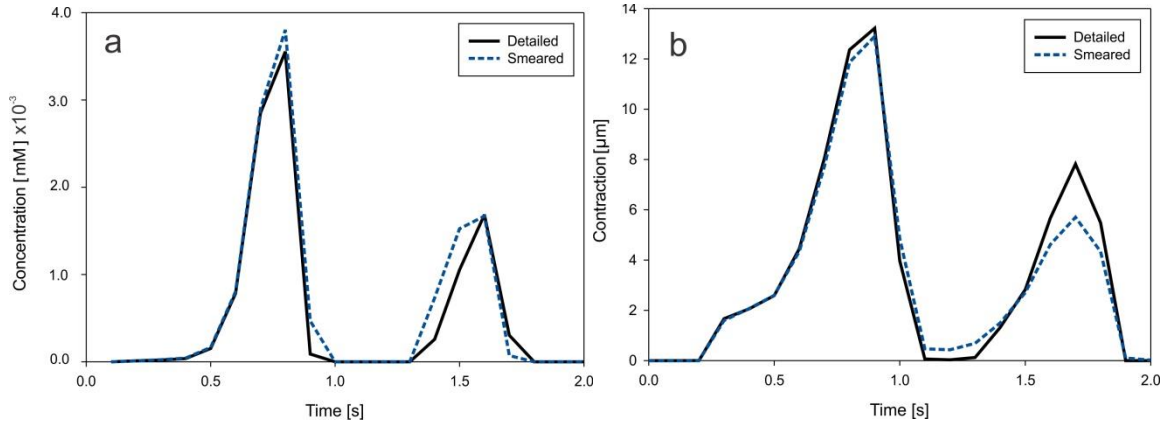

Fig. 39. a) Concentration change of Ca^{2+} in cells due to cell membrane currents. b) Mean contraction (displacement) of the right vertical boundary of heart tissue segment, due to Ca^{2+} change in muscle cells.

Effective contraction (modulus of the displacement vector) field of the tissue for the first cycle of action potential function Ve(t) is shown in Fig. 40. It can be seen that the largest contraction occurs at t = 0.9s. Good agreement is observed between the results of the two models.

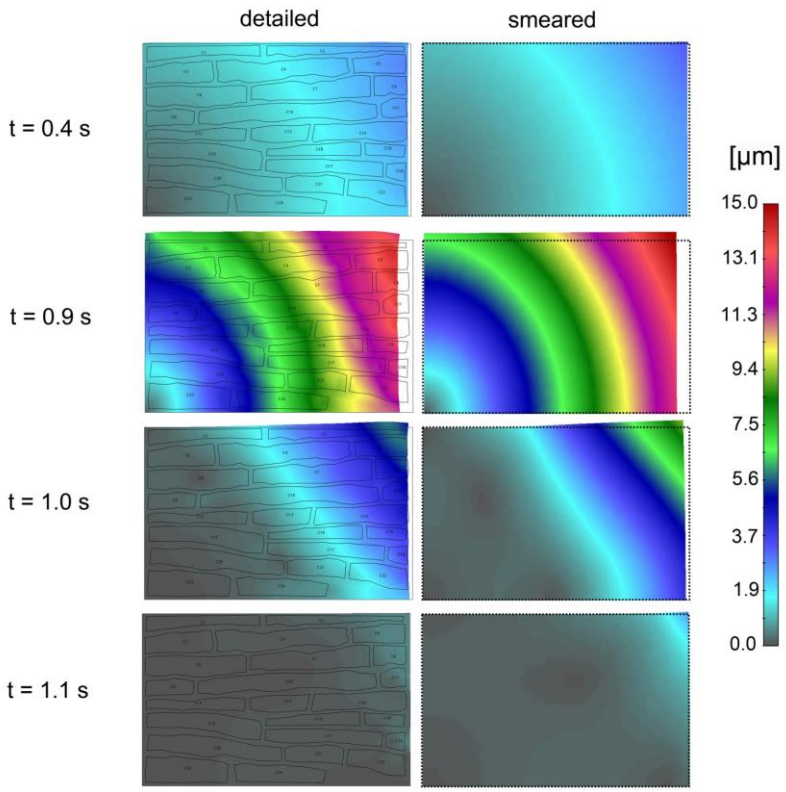

Fig. 40. Effective contractions (displacements) according to the detailed model (left panel) and smeared model (right panel) for four time points (0.4, 0.9, 1.0 and 1.1s) of first cycle of action potential function (inlet Ve(t) in Fig. 35a).

Electric field potentials within extracellular space for four time points, according to detailed and smeared model, is shown in Fig. 41. Potential within cells is kept constant Ve = -20 mV. Agreement between solutions of the two models is noted.

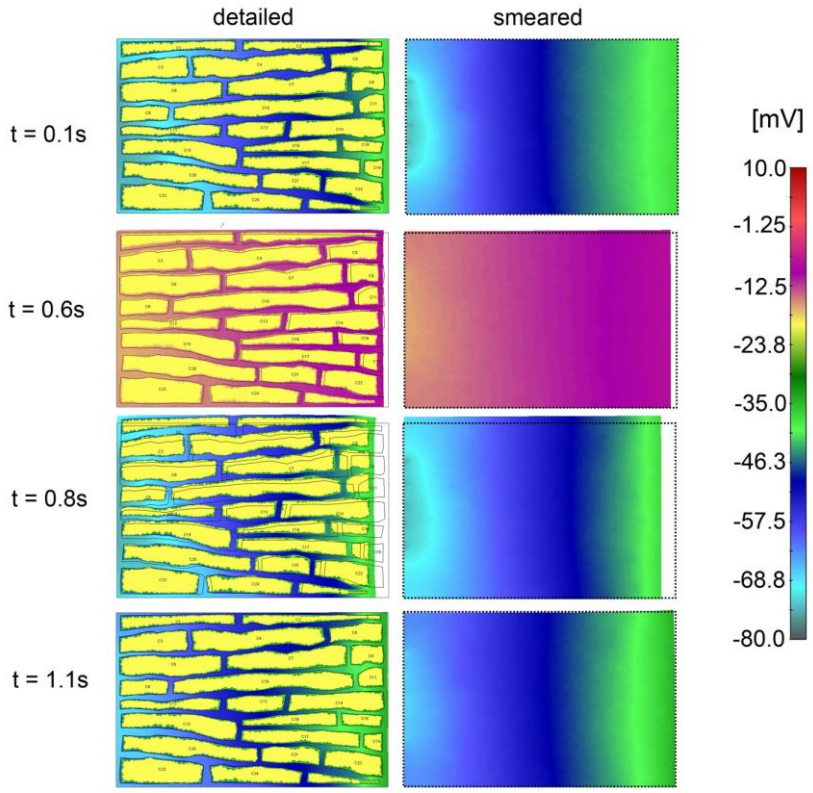

Fig. 41. Electric potential according to detailed model (left panel) and extracellular space of smeared model (right panel) for four time moments (0.4, 0.9, 1.0 and 1.1s) of the first cycle of action potential function.

4. Linking Alya and PAK to subject specific data

MUSICO module is an essential part of the SILICOFCM platform with a role to make a connection between genetic data obtained from gene analysis and their consequences on heart behavior (muscle fibres or modulated heart function) that is simulated using Alya or PAK finite element solver. Genetic data, extracted by the use of various bioinformatics tools (bioinformatics pipeline variant annotation pipeline), will be given as inputs to simulations of modulated muscle function (Task 5.3). MUSICO input parameters for the particular genetic variant are read from the predefined lookup table, and further used in simulations of muscle fibers behavior or modulated hearth function. Lookup table that maps genetic variants to the related MUSICO parameters will be obtained by fitting MUSICO results with a number of experiments performed on modulated tissues.
Within Alya's or PAK's incremental-iterative numerical algorithm, MUSICO module is used to calculate instantaneous material properties in each integration (Gaussian) point of each finite element (FE) in the muscle geometry mesh, as shown in the Figure 42.

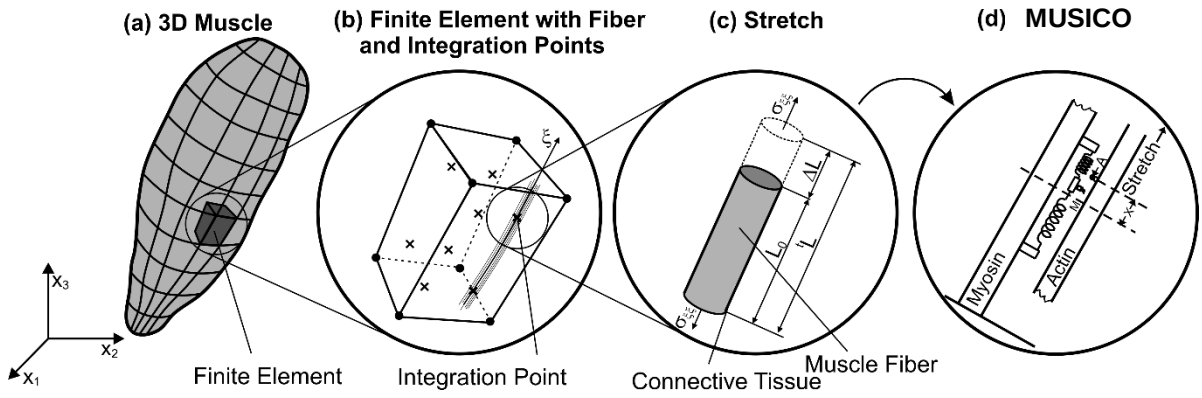

Fig. 42. Finite element muscle model

Unfortunately, due to inherent computing complexity of MUSICO, such massive calls from FE solver would lead to unacceptable calculation duration for the simulation of even one hearth beat. Therefore, it is not realistic that MUSICO can be directly coupled with FE solvers (Task 5.4). For these purposes MUSICO will be replaced with a less calculation demanding modules based on mass-action laws or surrogate models built using machine learning techniques. In the first case, MUSICO will be used as a reference software for the calibration of mass-action models to ensure that their results well enough fit more realistic MUSICO simulations. In second case, MUSICO will be used as a generator of a number of input-output pairs, sufficient to teach an adequate regression surrogate model. Moreover, in order to speed-up simulations, the platform is provided with parallelized computational algorithm.

5. FEA solvers in SILICOFCM platform

Both ALYA and PAK FEA solver are part of the SILICOFCM cloud platform and serve as simulation tools inside it. The provided FEA simulation tools are high CPU expensive solvers. As reported in the Deliverable D1.2 the infrastructure requirements for these solvers are depicted below:

ALYA FEA solver

Requirement	Specification
CPUs (cores)	2000
GPUs	Not required
Memory (GiB)	1.8 per core
Storage (GiB)	90

PAK FEA solver

Requirement	Specification
CPUs (cores)	250-500
GPUs	Not applicable
Memory (GiB)	16-64 per core
Storage (GiB)	2000-4000 in total

In order for the tools to be integrated into the platform two ways will be adopted. The first refers to the internal integration where dedicated VMs will be created. In these VMs the solvers will be installed in an automated way through a provided executable scripting. Such a procedure is an Install Wrapper package which is created using scripting language. The objective of the aforementioned procedure is to ensure the solvers will be fully deployed in the target VMs in an unattended manner. The provided wrappers will check for the Pre / Post-requisites in order to achieve a successful installation.

The second alternative will rely on the fact that the solvers will reside out of the SILICOFCM infrastructure. The abovementioned alternative will exploit external HPC infrastructures where both tools could be deployed and executed. For this purpose, the REST API technology can be utilised in order for the SILICOFCM platform to communicate externally with the solvers and executed through predefined execution scripts. The necessary inputs, BC and parameters will be sent to the target HPC machines and when the simulation will be end the results will be transferred safely to the SILICOFCM premises. Since the results for such simulations need big file size in order to overcome communication bottlenecks only selected attributes and data will be transferred for visualisation and assessment by the end user. The latter will be accomplished through automatic predefined executable scripts. For security reasons all the communication will be encrypted through TLS encryption protocols which is a straight forward way to accomplish secure interconnections.

6. Deviation from the work plan

No delay, change or deviation from the work plan has occurred.

7. Conclusions

The Barcelona Supercomputer Center has been continuously upgrading and testing their code Alya in order to comply with the necessary requirements to create electromechanical simulations of the hypetrophic cardiomyopathic human heart. The future work will be to couple the reduced MUSICO library to the finite element code Alya to create tightly coupled electro-mechanic simulations of HCM patients.

R&D Center for Bioengineering BioIRC made efforts to upgrade code regarding implementation of CSFEM. A general smeared methodology for field problems, as a generalization of the previously published applications for diffusion within tissue, is extended to include the electrical potential field. This expanding model also incorporates membrane ionic transport, particularly important in muscle and heart electromechanics. The concept is further enhanced by including ionic transport in tissue so that the concentration and electrical potential fields are coupled. Also, a composite cable finite element (CCFE) is introduced for electrical signal propagation within axons and its accuracy is verified. Selected examples demonstrate accuracy and efficiency of the smeared method. The composite smeared finite element (CSFE) is a continuum element which contains all domains within the biological system. The domains occupy volumetric fractions of the element and have their own physical fields, hence the nodal variables include all fields. Moreover, the complex 1-D gradient driven fields are substituted by a continuum representation using the corresponding transport tensors. The physical fields within the CSFE are coupled by connectivity elements (spatially fictitious) at nodes which take into account size and properties of membranes (walls) which physically separate the domains. Besides the good solution accuracy (in comparison with detailed models), the smeared models are easy to generate when simulating processes within complex structures and geometrical shapes of biological systems. Furthermore, the smeared models are orders of magnitude smaller in the number of equations when compared to detailed models. Thus, we conclude that the presented FE models based on the smeared concept offer a novel computational tool for practical applications in biomedical investigations.

8. Appendix: Aditional details about PAK

8.1 FE model of electric conduction in nerves based on the cable theory, formulation of the composite cable finite element (CCFE)

We formulate a 1D finite element for electric conduction using the fundamental equation for electric conduction along fibers according to the so-called cable theory; this specific finite element is called Composite Cable Finite Element (CSFE). The theory was initiated William Thomson in 1850s who developed mathematical models of signal decay in telegraphic cables. Later, these models were implemented and experimentally verified in neuroscience.

Analytical solution. In accordance with equations (55) and (56), the cable equation in which both axial and lateral currents are taken into account, can be written as

$$G_a \frac{\partial^2 V_e^{in}}{\partial x^2} = G_m \left(V_e^{in} - V_e^{ext} \right) + C_m \left(\frac{\partial V_e^{in}}{\partial t} - \frac{\partial V_e^{ext}}{\partial t} \right) + I_{ion} \tag{A.1}$$

In order to compare numerical solution using our composite cable finite element (CCFE), we will omit the ionic current I_{ion} and assume that the external potential is V_e^{ext} is equal to zero. These assumptions do not reduce the proof of the validity and accuracy of the CCFE. Hence, the equation (A.1) can be written as

$$\frac{1}{r_l} \frac{\partial^2 V_e^{in}}{\partial x^2} = c_m \frac{\partial V_e^{in}}{\partial t} + \frac{V_e^{in}}{r_m} \tag{A.2}$$

were r_m (Ω·mm) and c_m (F/mm) are membrane resistivity and capacitance, respectively, and r_l (in Ω/mm) is the longitudinal intracellular resistance per unit length; they can be expressed as

$$r_m = \frac{R_m}{2\pi r} = \frac{1}{2\pi r G_m} \tag{A.3}$$

$$c_m = C_m 2\pi r \tag{A.4}$$

$$r_l = \frac{\rho_l}{\pi r^2} = \frac{1}{G_a \pi r^2} \tag{A.5}$$

where G_m is specific membrane conductance (Siemens/mm^2), inverse of R_m; ρ_l (Ω·mm) is electrical resistance of the axoplasm; G_a is the nerve conductance (in Siemens/mm).

Further, a length constant λ can be introduced as a parameter that indicates how far a stationary current will influence the voltage along the cable. The length constant can be specified as

$$\lambda = \sqrt{\frac{r_m}{r_l}} \tag{A.6}$$

The first term at the right-hand side of (A.2) affects the rate of change of the potential, which tends to a steady state distribution with time increase (theoretically – infinite time, practically – enough large time period). The steady state condition corresponds to c_m = 0, so that (A.3) reduces to

$$\lambda^2 \frac{d^2 V_e^{in}}{dx^2} = V_e^{in} \tag{A.7}$$

A general solution of this equation is

$$V_e^{in} = C_1 e^{x/\lambda} + C_2 e^{-x/\lambda} \tag{A.8}$$

Constants C_1 and C_2 can be determined from boundary conditions. We will further use the conditions as in our numerical solutions: x=0, V=V_0; x=L, V_L=0, where L is the length along the cable. Then, the solution is

$$V_e^{in} = \frac{V_0}{e^{L/\lambda} - e^{-L/\lambda}} \left(e^{\frac{L-x}{\lambda}} - e^{-\frac{L-x}{\lambda}} \right) \tag{A.9}$$

Composite Cable Finite element. A 1D finite element model for a nerve fiber is schematically shown in Fig. A1.

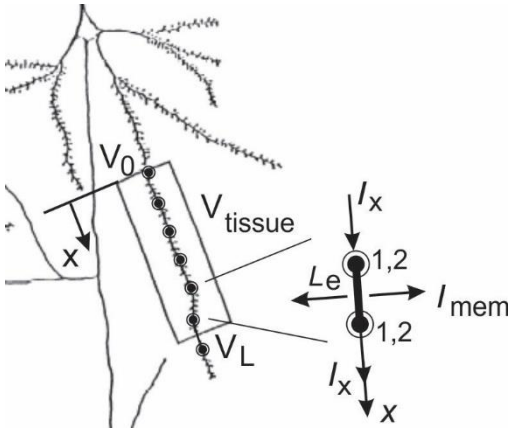

Fig. A1. Composite Cable Finite Element (CCFE). The element includes axial conduction along the element axis (current I_x) and lateral between the fiber and the surrounding tissue (current I_{mem}). The axial conduction is modeled by the 1D conductivity FE terms, while the lateral part is modeled by the connectivity elements 1,2 at each node.

The axial conduction balance equation, for the equilibrium iteration *i*, of the CCFE is represented in a standard form, which, for the 2-node element with nodes *I* and *J*, is

$$K_{IJ}^a \Delta V_e^{in\,J(i)} = I_I^{ext} - K_{IJ}^a V_e^{in\,J(i-1)}, \quad I, J = 1,2;\ sum\ on\ J \tag{A.10}$$

where I_I^{ext} is the current coming from the neighboring elements (the I_I^{ext} cancel for all internal nodes of the FE system), and the matrix terms are

$$K_{11}^a = K_{22}^a = -K_{12}^a = -K_{21}^a = \frac{\pi r^2}{L_e} G_a \tag{A.11}$$

where L_e is the element length.

The lateral electric flow is modeled by connectivity elements 1,2. The connectivity element represents the electric flow through the surface belonging to the element. For a node *J* the size of this surface is

$$A_J = 2r\pi L_J \tag{A.12}$$

where L_J is the length belonging to the node. Then, the balance equation for the element 1,2 at the node *J* is

$$\left(\frac{1}{\Delta t}M_{IJ}^{m}+K_{IJ}^{m}\right)\Delta V_J^{(i)}=-\left(\frac{1}{\Delta t}M_{IJ}^{m}+K_{IJ}^{m}\right)V_J^{(i-1)}+\frac{1}{\Delta t}M_{IJ}^{m}V_J^{t} \qquad \text{(A.13)}$$

where V_1 and V_2 are potentials in the fiber V_e^{in} and the surrounding tissue V_e^{ext}, respectively; V_J^t is potential at start of times step; and the matrices are given by equation (58) where the surface area A_{mem} is evaluated according to (A.12).

Numerical results. The goal is to validate accuracy of the CCFE element by comparing numerical results with the analytical solution (A.9). Data used in numerical FE model are:

V_0= 1 mV; V_L=0; L=10mm (length of the domain), cable diameter r = 0.5mm,

Ranges of values used in numerical solutions are:

- G_a = [1, 100] [S/mm]
- G_m = [1, 100] [S/mm²]
- c_m = [0, 1, 100] (F/mm²)

FE model consists of 1D composite cable finite elements (CCFEs), and surrounding continuum with prescribed V = 0 at all nodes (Fig. A2). Dimension of the continuum is 10 x 1 mm, and FE division is 100 x 2. There are also 100 CCFEs.

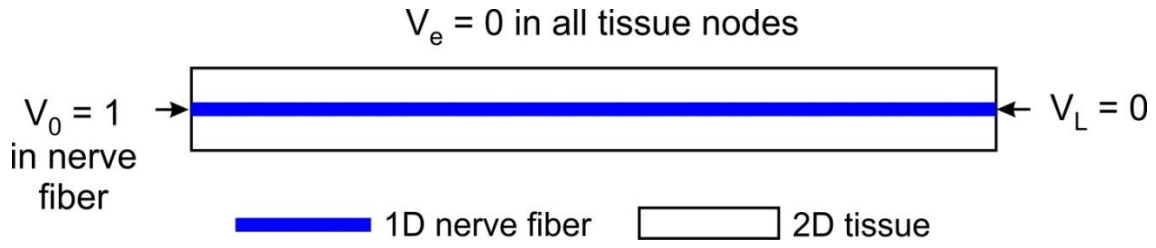

Fig. A2. FE model of nerve fiber (CCFE elements) with surrounding 2D tissue.

Distribution of electrical potential in 1D fiber, for three values of the nerve conductance G_a, is shown on Fig. A3. It can be seen how the electrical signal propagation increases with G_a.

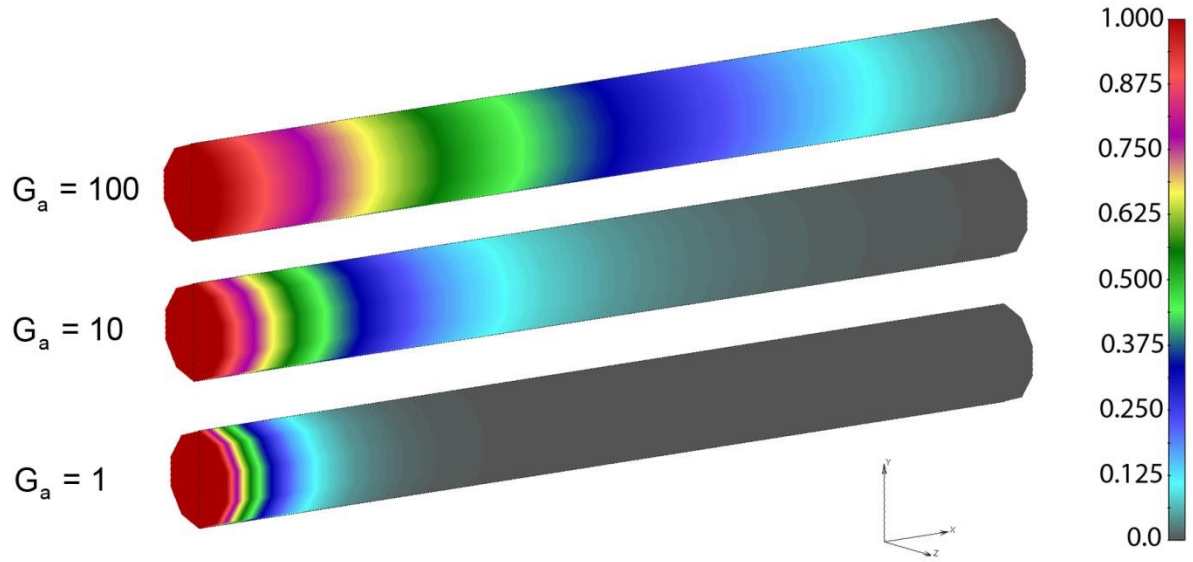

Fig. A3. Distribution of electrical potential in in the nerve fiber at stationary state, for case with: G_a = 1, 10, 100 [S/mm], and G_m = 1 [S/mm²], c_m = 1 [S/mm²].

We have selected several material data sets to illustrate how the material parameters affect the solutions. The data sets, and the values of length constant, λ, are (G_a [S/mm], G_m [S/mm^2], c_m [S/mm^2]):

G_a = 1,	G_m = 1,	r = 0.5,	λ = 0.5
G_a = 100,	G_m = 1,	r = 0.5,	λ = 7.07
G_a = 1,	G_m = 100,	r = 0.5,	λ = 0.0707
G_a = 100,	G_m = 100,	r = 0.5,	λ = 0.71

Diagrams of electric potential distribution along nerve fiber in the stationary state are shown in Fig. A4. There is evident agreement between the numerical and analytical solutions. It can be seen that solutions G_a = 1, G_m = 1 and G_a = 100, G_m = 100 are the same, while increase of G_m leads to decrease of the electrical propagation length.

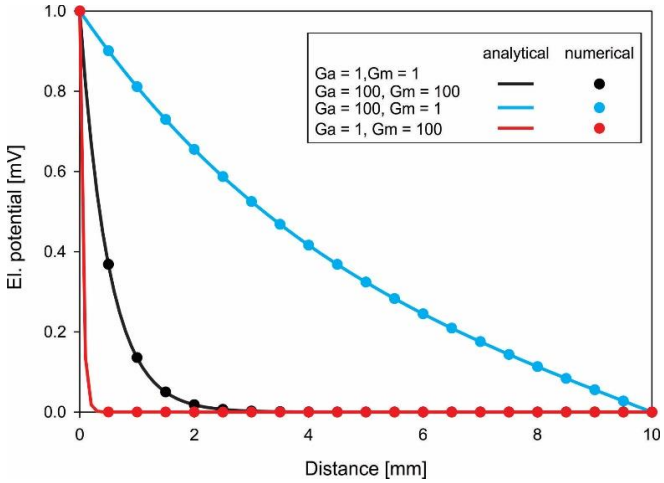

Fig. A4. Electrical potential vs. length of nerve (analytical and numerical solution) for stationary state for various (G_a, G_m) values, c_m=1.

Change of the potential profiles over time, for G_a = 100, G_m = 1, c_m = 10, is shown in Fig. A5. It can be seen from this figure how the profiles approach to the stationary shape. The stationary profile is reached after 20s, since after that time the profiles remain practically the same (changes of potential in all points become very small).

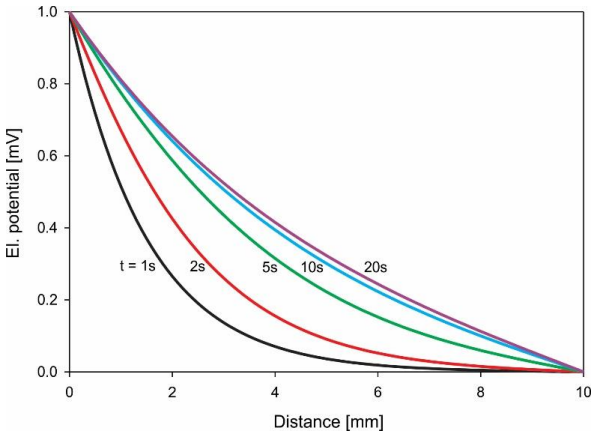

Fig. A5. Electrical potential profiles for several time moments during transient states. Data: G_a = 100, G_m = 1, c_m = 10. The stationary profile is reached at t=20s.

Finally, we show in Fig. A6 how time for reaching the stationary state depends on the specific capacitance of membrane c_m. It can be seen that dependence is linear.

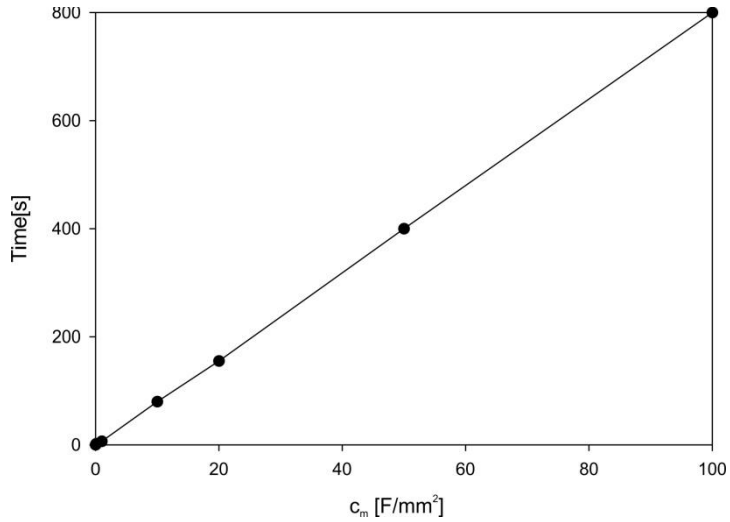

Fig. A6. Time of reaching the stationary state vs. specific capacitance of membrane (c_m), for G_a = 1, G_m = 1.

8.2 Computation of the ionic currents through cell membranes

Here are presented the fundamental relations for calculation of membrane currents of potassium and sodium according to [77], and further implementation of these relations into the incremental-iterative FE form. These relations are experimentally determined for Purkinje fibers.

The potassium current I_K is expressed as (in μA/cm^2)

$$I_K = (g_{K1} + g_{K2})(V_m - V_K) \tag{B.1}$$

where g_{K1} and g_{K2} are membrane conductivities, V_m (in mV) is the membrane potential (defined as the difference between potentials inside and outside of cell, and V_K is equilibrium potential (in [77] taken to be -100mV); dimension of g_{K1} and g_{K2} is [μA/(cm^2 mV)]. According to experimental measurements, the expressions for the conductivities are:

$$g_{K1} = 1.2\exp\left[(-V_m - 90)/50\right] + 0.015\exp\left[(V_m + 90)/60\right] \tag{B.2}$$

$$g_{K2} = 1.2n^4$$

where

$$\frac{dn}{dt} = \alpha_n(1-n) - \beta_n n \tag{B.3}$$

where

$$\alpha_n = \frac{0.0001(-V_m - 50)}{\exp\left[(-V_m - 50)/10\right] - 1}, \quad \beta_n = 0.002\exp\left[(-V_m - 90)/80\right]$$

For sodium current density I_{Na} the expression is

$$I_{Na} = g_{Na}(V_m - V_{Na}) \tag{B.4}$$

where V_{Na}=40mV and

$$g_{Na} = 400m^3h + 0.14 \tag{B.5}$$

Expressions for parameters *m* and *h* are as follows:

$$\frac{dm}{dt} = \alpha_m (1-m) - \beta_m m \tag{B.6}$$

where

$$\alpha_m = \frac{0.1(-V_m - 48)}{\exp\left[(-V_m - 48)/15\right] - 1}, \quad \beta_m = \frac{0.12(V_m + 8)}{\exp\left[(V_m + 8)/5\right] - 1} \tag{B.7}$$

and

$$\frac{dh}{dt} = \alpha_h (1-h) - \beta_h h \tag{B.8}$$

where

$$\alpha_h = 0.17 \exp\left[(-V_m - 90)/20\right], \quad \beta_h = \left[\exp\left(\frac{-V_m - 42}{10}\right) + 1\right]^{-1} \tag{B.9}$$

We further integrate equations (B.3) and (B.6) within time step. Equation (B.3) can be written as

$$\frac{dn}{dt} = \alpha_n - (\alpha_n + \beta_n) n$$

Implicit integration scheme is used within time step Δt, so that

$$n^{t+\Delta t} = \frac{1}{(\alpha_n + \beta_n)} \left\{ \alpha_n - \left[\alpha_n - (\alpha_n + \beta_n) n^t \right] \exp\left[-(\alpha_n + \beta_n) \Delta t \right] \right\} \tag{B.10}$$

where the right-upper indices *t* and $t + \Delta t$ refer to the start and end of time step.
The analogous expression can be obtained for the parameters *m* and *h*:

$$\begin{aligned} m^{t+\Delta t} &= \frac{1}{(\alpha_m + \beta_m)} \left\{ \alpha_m - \left[\alpha_m - (\alpha_m + \beta_m) m^t \right] \exp\left[-(\alpha_m + \beta_m) \Delta t \right] \right\}, \\ h^{t+\Delta t} &= \frac{1}{(\alpha_h + \beta_h)} \left\{ \alpha_h - \left[\alpha_h - (\alpha_h + \beta_h) h^t \right] \exp\left[-(\alpha_h + \beta_h) \Delta t \right] \right\}. \end{aligned} \tag{B.11}$$

With these coefficients determined for the end of time step, the conduction coefficients can be determined and the currents specified in (B.1) and (B.4) can be calculated. We calculate coefficients in (B.7) and (B.9) using the corresponding mean values of membrane potential V_m

$$V_m = \frac{1}{2}\left(V_m^t + V_m^{t+\Delta t}\right) \tag{B.12}$$

9. References

[1] Hunter P.J., A.D. McCulloch, ter Keurs H.E.D.J. Modelling the mechanical properties of cardiac muscle. Progress in Biophysics and Molecular Biology. 1998 Mar; 69(2-3):289-331.

[2] Land et al. A model of cardiac contraction based on novel measurements of tension development in human cardiomyocytes. Journal of Molecular and Cellular Cardiology (2017).

[3] M. Kojic, M. Milosevic, V. Simic, E.J. Koay, J.B. Fleming, S. Nizzero, N. Kojic, A. Ziemys , M. Ferrari, A composite smeared finite element for mass transport in capillary systems and biological tissue, Comp. Meth. Appl. Mech. Engrg., 324, 413–437, https://doi.org/10.1016/j.cma.2017.06.019, 2017.

[4] M. Kojic, M. Milosevic, V. Simic, E. J. Koay, N. Kojic, A. Ziemys, M. Ferrari, Extension of the Composite Smeared Finite Element (CSFE) to Include Lymphatic System in Modeling Mass Transport in Capillary Systems and Biological Tissue, J. Serb. Soc. Comp. Mech., Vol 11, No.2, 108-120, 2017.

[5] M. Milosevic, V. Simic, B. Milicevic, E.J. Koay, M. Ferrari, A. Ziemys, M. Kojic, Correction function for accuracy improvement of the Composite Smeared Finite Element for diffusive transport in biological tissue systems, Comp. Meth. Appl. Mech. Engrg., https://doi.org/10.1016/j.cma.2018.04.012

[6] Milos Kojic, Smeared concept as a general methodology in finite element modeling of physical fields and mechanical problems in composite media, J. Serb. Soc. Comp. Mech., Vol 12, No.2, 1-16, 2018.

[7] M. Kojic, M. Milosevic, V. Simic, A. Ziemys, N. Filipovic, M. Ferrari, “Smeared multiscale finite element model for electrophysiology and ionic transport in biological tissue”, Comput. Biol. Medicine, Volume 108, May 2019, Pages 288-304.

[8] J. Schaff, C.C. Fink, B. Slepohenko, J.H. Carson, L.M. Loew, A General Computational Framework for Modeling Cellular Structure and Function, Biophysical Journal, 73 (1997) 1135-1146.

[9] Thomas O’Hara, László Virág, András Varró, and Yoram Rudy. Simulation of the undiseased human cardiac ventricular action potential: Model formulation and experimental validation. PLoS Computational Biology, 7(5), 2011.

[10] Guillaume Houzeaux, Mariano Vázquez, R Aubry, and José M Cela. A massively parallel fractional step solver for incompressible flows. Journal of Computational Physics, 228(17):6316–6332, 2009.

[11] Mariano Vázquez, Ruth Arís, Guillaume Houzeaux, R Aubry, and P Villar. A massively parallel computational electrophysiology model of the heart. International journal for numerical methods in biomedical engineering, 2011.

[12] Mariano Vazquez, Guillaume Houzeaux, Seid Koric, Antoni Artigues, Jazmin Aguado-Sierra, Ruth Aris, Daniel Mira, Hadrien Calmet, Fernando Cucchietti, Herbert Owen, Ahmed Taha, and Jose Maria Cela. Alya: Towards Exascale for Engineering Simulation Codes. pages 1–20, 2014.

[13] E. Casoni, a. Jérusalem, C. Samaniego, B. Eguzkitza, P. Lafortune, D. D. Tjahjanto, X. Sáez, G. Houzeaux, and M. Vázquez. Alya: Computational Solid Mechanics for Supercomputers. Archives of Computational Methods in Engineering, 2014.

[14] Benjamin Uekermann, Juan Carlos Cajas, Bernhard Gatzhammer, Guillaume Houzeaux, Miriam Mehl, and Mariano Vazquez. Towards Partitioned Fluid-Structure Interaction on Massively Parallel Systems. 11th World Congress on Computational Mechanics (WCCM XI), (Wccm Xi):1–12, 2014.

[15] George Karypis and Vipin Kumar. A Fast and High Quality Multilevel Scheme for Partitioning Irregular Graphs. SIAM Journal on Scientific Computing, 20(1):359–392, 1998.

[16] Zygote Media Group Inc. Zygote Solid 3D heart Generation II Developement Report. Technical report, 2014.

[17] Taras Usyk and Andrew D Mcculloch. Relationship Between Regional Shortening and Asynchronous Electrical Activation in a Three-Dimensional Model of Ventricular Electromechanics. Journal of Cardiovascular Electrophysiology, 14(s10):S196–S202, 2003.

[18] Roy C. P. Kerckhoffs, Owen P. Faris, Peter H. M. Bovendeerd, Frits W. Prinzen, Karel Smits, Elliot McVeigh, and Theo Arts. Timing of Depolarization and Contraction in the Paced Canine Left Ventricle:. Model and Experiment. Journal of Cardiovascular Electrophysiology, 14(s10):S188–S195, 2003.

[19] Ling Xia, Meimei Huo, Qing Wei, Feng Liu, and Stuart Crozier. Analysis of cardiac ventricular wall motion based on a threedimensional electromechanical biventricular model. Physics in Medicine and Biology, 50(8):1901–1917, 2005.

[20] Hiroshi Watanabe, Seiryo Sugiura, Hidenobu Kafuku, and Toshiaki Hisada. Multiphysics simulation of left ventricular filling dynamics using fluid-structure interaction finite element method. Biophysical journal, 87(3):2074–2085, 2004.

[21] L Geerts, P Bovendeerd, K Nicolay, and T Arts. Characterization of the normal cardiac myofiber field in goat measured with MR-diffusion tensor imaging. Am J Physiol Heart Circ Physiol, 283(1):H139–145, 2002.

[22] Irvin Teh, Rebecca A.B. Burton, Darryl McClymont, Rebecca A. Capel, Daniel Aston, Peter Kohl, and Jürgen E. Schneider. Mapping cardiac microstructure of rabbit heart in different mechanical states by high resolution diffusion tensor imaging: A proof-of-principle study. Progress in Biophysics and Molecular Biology, 121(2):85–96, 2016.

[23] Jason D. Bayer, Robert C. Blake, Gernot Plank, and Natalia A. Trayanova. A novel rule-based algorithm for assigning myocardial fiber orientation to computational heart models. Annals of Biomedical Engineering, 40(10):2243–2254, 2012.

[24] Sergey F Pravdin, Vitaly I Berdyshev, Alexander V Panfilov, Leonid B Katsnelson, Olga Solovyova, and Vladimir S Markhasin. Mathematical model of the anatomy and fibre orientation field of the left ventricle of the heart. BioMedical Engineering OnLine, 12(1):54, 2013.

[25] Jonathan Wong and Ellen Kuhl. Generating fibre orientation maps in human heart models using Poisson interpolation. Computer Methods in Biomechanics and Biomedical Engineering, 17(11):1217–1226, 2014.

[26] Rubén Doste, David Soto-Iglesias, Gabriel Bernardino, Rafael Sebastian, Sophie Giffard-Roisin, Rocio Cabrera-Lozoya, Maxime Sermesant, Antonio Berruezo, Damián Sánchez-Quintana, and Oscar Camara. A rule-based method to model myocardial fiber orientation for simulating ventricular outflow tract arrhythmias. In International Conference on Functional Imaging and Modeling of the Heart, pages 344–353. Springer, 2017.

[27] Daniel D. Streeter and David L. Bassett. An engineering analysis of myocardial fiber orientation in pig's left ventricle in systole. The Anatomical Record, 155(4):503–511, 1966.

[28] Anter E, Tschabrunn CM, Buxton AE, Josephson ME. High-resolution mapping of postinfarction reentrant ventricular tachycardia: Electrophysiological characterization of the circuit. Circulation. 2016;134:314-327.

[29] Pashakhanloo F, Herzka DA, Mori S, Zviman M, Halperin H, Gai N, Bluemke DA, Trayanova NA, McVeigh ER. Submillimeter diffusion tensor imaging and late gadolinium enhancement cardiovascular magnetic resonance of chronic myocardial infarction. J Cardiovasc Magn Reson. 2017;19:9.

[30] Wu MT, Tseng WY, Su MY, Liu CP, Chiou KR, Wedeen VJ, Reese TG, Yang CF. Diffusion tensor magnetic resonance imaging mapping the fiber architecture remodeling in human myocardium after infarction: Correlation with viability and wall motion. Circulation. 2006;114:1036-1045.

[31] Scollan DF, Holmes A, Winslow R, Forder J. Histological validation of myocardial microstructure obtained from diffusion tensor magnetic resonance imaging. Am J Physiol. 1998;275:H2308-2318.

[32] Pashakhanloo F, Herzka DA, Ashikaga H, Mori S, Gai N, Bluemke DA, Trayanova NA, McVeigh ER. Myofiber architecture of the human atria as revealed by submillimeter diffusion tensor imaging. Circ Arrhythm Electrophysiol. 2016;9:e004133.

[33] Ferreira PF, Kilner PJ, McGill LA, Nielles-Vallespin S, Scott AD, Ho SY, McCarthy KP, Haba MM, Ismail TF, Gatehouse PD, de Silva R, Lyon AR, Prasad SK, Firmin DN, Pennell DJ. In vivo cardiovascular magnetic resonance diffusion tensor imaging shows evidence of abnormal myocardial laminar orientations and mobility in hypertrophic cardiomyopathy. J Cardiovasc Magn Reson. 2014;16:87.

[34] M. Kojic, R. Slavkovic, M. Zivkovic, N. Grujovic, N. Filipovic, M. Milosevic, PAK - Finite Element Program for Linear and Nonlinear Analysis, Univ Kragujevac and R&D Center for Bioengineering, Kragujevac, Serbia, 2010.

[35] K.H.W.J. ten Tusscher, D Noble, P J Noble, and A V Panfilov. A model for human ventricular tissue. AJP - Heart and Circulatory Physiology, 286(4):H1573–H1589, 2004.

[36] Thomas O'Hara, László Virág, András Varró, and Yoram Rudy. Simulation of the undiseased human cardiac ventricular action potential: Model formulation and experimental validation. PLoS Computational Biology, 7(5), 2011.

[37] Blanca Rodríguez, James C Eason, and Natalia Trayanova. Differences between left and right ventricular anatomy determine the types of reentrant circuits induced by an external electric shock. A rabbit heart simulation study. Progress in biophysics and molecular biology, 90(1- 3):399–413, 2006.

[38] Martyn P. Nash and Alexander V. Panfilov. Electromechanical model of excitable tissue to study reentrant cardiac arrhythmias. Progress in Biophysics and Molecular Biology, 85(2-3):501–522, 2004.

[39] E J Vigmond, R Ruckdeschel, and Natalia Trayanova. Reentry in a morphologically realistic atrial model. Journal of cardiovascular electrophysiology, 12(9):1046–54, sep 2001.

[40] R H Clayton, O Bernus, E M Cherry, H Dierckx, Flavio H Fenton, L Mirabella, Alexander V. Panfilov, F B Sachse, Gunnar Seemann, and H Zhang. Models of cardiac tissue electrophysiology:

progress, challenges and open questions. Progress in biophysics and molecular biology, 104(1-3):22–48, jan 2011.

[41] E. Passini, O. J. Britton, H. R. Lu, J. Rohrbacher, A. N. Hermans, D. J. Gallacher, R. J. H. Greig, A. Bueno-Orovio, and B. Rodriguez, Human in silico drug trials demonstrate higher accuracy than animal models in predicting clinical pro-arrhythmic cardiotoxicity, Frontiers in Physiology, 8 (2017).

[42] Mariano Vázquez, Ruth Arís, Guillaume Houzeaux, R Aubry, and P Villar. A massively parallel computational electrophysiology model of the heart. International journal for numerical methods in biomedical engineering, 2011.

[43] Pierre Lafortune, Ruth Arís, Mariano Vázquez, and Guillaume Houzeaux. Coupled electromechanical model of the heart : Parallel finite element formulation. International journal for numerical methods in biomedical engineering, 28:72–86, 2012.

[44] Steven A Niederer, Eric Kerfoot, Alan P Benson, Miguel O Bernabeu, Olivier Bernus, Chris Bradley, Elizabeth M Cherry, Richard Clayton, Flavio H Fenton, Alan Garny, et al. Verification of cardiac tissue electrophysiology simulators using an n-version benchmark. Phil. Trans. R. Soc. A, 369(1954):4331–4351, 2011.

[45] D Sung, R W Mills, J Schettler, S M Narayan, J H Omens, and A D McCulloch. Ventricular filling slows epicardial conduction and increases action potential duration in an optical mapping study of the isolated rabbit heart. J Cardiovasc Electrophysiol, 14(7):739–749, 2003.

[46] Steven A. Niederer and Nicolas P. Smith. An improved numerical method for strong coupling of excitation and contraction models in the heart. Progress in Biophysics and Molecular Biology, 96(1-3):90– 111, 2008.

[47] Martyn P. Nash and Alexander V. Panfilov. Electromechanical model of excitable tissue to study reentrant cardiac arrhythmias. Progress in Biophysics and Molecular Biology, 85(2-3):501–522, 2004.[48] Steven A. Niederer and Nicolas P. Smith. An improved numerical method for strong coupling of excitation and contraction models in the heart. Progress in Biophysics and Molecular Biology, 96(1-3):90– 111, 2008.

[48] John Jeremy Rice, Fei Wang, Donald M Bers, and Pieter P de Tombe. Approximate model of cooperative activation and crossbridge cycling in cardiac muscle using ordinary differential equations. Biophysical journal, 95(5):2368–90, 2008.

[49] Sander Land, So-jin Holohan, Nicolas P. Smith, Cristobal G. dos Remedios, Jonathan C Kentish, and Steven A Niederer. A model of cardiac contraction based on novel measurements of tension developement in human cardiomyocites. Journal of Molecular and Cellular Cardiology, 2017.

[50] M. Kojic, M. Milosevic, V. Simic, E.J. Koay, J.B. Fleming, S. Nizzero, N. Kojic, A. Ziemys , M. Ferrari , A composite smeared finite element for mass transport in capillary systems and biological tissue, Comp. Meth. Appl. Mech. Engrg., 324, 413–437, https://doi.org/10.1016/j.cma.2017.06.019, 2017.

[51] M. Kojic, M. Milosevic, V. Simic, E. J. Koay, N. Kojic, A. Ziemys, M. Ferrari, Extension of the Composite Smeared Finite Element (CSFE) to Include Lymphatic System in Modeling Mass Transport in Capillary Systems and Biological Tissue, J. Serb. Soc. Comp. Mech., Vol 11, No.2, 108-120, 2017.

[52] M. Milosevic, V. Simic, B. Milicevic, E.J. Koay, M. Ferrari, A. Ziemys, M. Kojic, Correction function for accuracy improvement of the Composite Smeared Finite Element for diffusive transport in biological tissue systems, Comp. Meth. Appl. Mech. Engrg., https://doi.org/10.1016/j.cma.2018.04.012.

[53] Milos Kojic, Smeared concept as a general methodology in finite element modeling of physical fields and mechanical problems in composite media, J. Serb. Soc. Comp. Mech., Vol 12, No.2, 1-16, 2018

[54] M. Kojic, M. Milosevic, V. Simic, A. Ziemys, N. Filipovic, M. Ferrari, "Smeared multiscale finite element model for electrophysiology and ionic transport in biological tissue", Comput. Biol. Medicine, Volume 108, May 2019, Pages 288-304.

[55] J. Schaff, C.C. Fink, B. Slepohenko, J.H. Carson, L.M. Loew, A General Computational Framework for Modeling Cellular Structure and Function, Biophysical Journal, 73 (1997) 1135-1146.

[56] M. Kojic, M. Milosevic, V. Simic, M. Ferrari, A 1D pipe finite element with rigid and deformable walls, J. Serb. Soc. Comp. Mech., 8 (2014) 38-53.

[57] R.L. Winslow, Theoretical Foundations of Neural Modeling, BME 580.681, The John Hopkins Univ. Sch. Medicine and Whiting Sch Engrg, Baltimore, 1992.

[58] M. Kojic, N. Filipovic, B. Stojanovic, N. Kojic, Computer Modeling in Bioengineering - Theoretical Background, Examples and Software, John Wiley and Sons, Chichester, England, 2008.

[59] M. Kojic, K.J. Bathe, Inelastic Analysis of Solids and Structures, Springer, Berlin,Heidelberg, New York, 2005.

[60] S. Trapp, R.W. Horobin, A predictive model for the selective accumulation of chemicals in tumor cells, Eur. Biophys. J., 34 (2005) 959–966.

[61] X. Zhang, K. Shedden, G.R. Rosania, A cell-based molecular transport simulator for pharmacokinetic prediction and cheminformatic exploration, Molec. Pharmaceutics, 3 (2006) 704-716.

[62] M. Kojic, R. Slavkovic, M. Zivkovic, N. Grujovic, N. Filipovic, M. Milosevic, PAK - Finite Element Program for Linear and Nonlinear Analysis, Univ Kragujevac and R&D Center for Bioengineering, Kragujevac, Serbia, 2010

[63] A.L. Hodkin, A.F. Huxley, A quantitative description of membrane current and its application to conduction and excitation in nerve, J. Physiology, 117 (1952) 500-544.

[64] R.H. Clayton, A.V. Panfilov, A guide to modelling cardiac electrical activity in anatomically detailed ventricles Progress in Bioph Molec. Biology 96, 96 (2008) 19–43.

[65] R.H. Clayton, O. Bernus, E.M. Cherry, H. Dierckx, F.H. Fenton, L. Mirabella, A.V. Panfilov, F.B. Sachse, G. Seemann, H. Zhang, Models of cardiac tissue electrophysiology: Progress,challenges and open questions, Progress Bioph. Molec. Biol. , 104 (2011) 22-48.

[66] J. Cooper, A. Corrias, D. Gavaghan, D. Noble, Considerations for the use of cellular electrophysiology models within cardiac tissue simulations, Progress Bioph. Molec. Biol., 107 (2011) 74-80.

[67] M.O. Bernabeu, R. Bordas, P. Pathmanathan, J. Pitt-Francis, J. Cooper, A. Garny, D.J. Gavaghan, B. Rodriguez, J.A. Southern, J.P. Whiteley, CHASTE: incorporating a novel multi-scale spatial and

temporal algorithm into a large-scale open source library, Phil. Trans. R. Soc. A, 367 (2009) 1907–1930

[68] B.J. Roth, J. J. P. Wikswo, A bidomain model for the extracellular potential and magnetic field of cardiac tissue, IEEE Trans. Biomed. Engrg., 33 (1986) 467-469.

[69] C.S. Henriquez, Simulating the electrical behavior of cardiac tissue using the bidomain model, Crit. Rev. Biomed. Engrg. , 21 (1993) 1-77.

[70] C.S. Henriques, A.L. Muzikant, C.K. Smoak, Anisotropy, fiber curvature, and bath loading effects on activation in thin and thick cardiac tissue preparations: Simulations in a three-dimensional bidomain model, J. Cardiov. Eiectrophysiology 7(1996) 424-444.

[71] J.P. Keener, A.V. Panfilov, A biophysical modelfor defibrillation of cardiac tissue, Biophysical Journal, 71 (1996) 1335-1345.

[72] A. Corrias, P. Pathmanathan, D.J. Gavaghan, M.L. Buista, Modelling tissue electrophysiology with multiple cell types: applications of the extended bidomain framework, Integr. Biol. , 4 (2012) 192–201.

[73] E.J. Vigmond, B.D. Stuyvers, Modeling our understanding of the His-Purkinje system, Progress Bioph. Molec. Biol., 120 (2016) 179-188.

[74] R.M. Bordas, K. Gillow, D. Gavaghan, B. Rodriguez, D. Kay, A bidomain model of the ventricular specialized conduction system of the heart SIAM J. Appl. Math. , 72 (2012) 1618–1643.

[75] D. Bruce, P. Pathmanathan, J.P. Whiteley, Modelling the effect of gap junctions on tissue-level cardiac electrophysiology, Bull. Math. Biol. , 76 (2014) 431–454.

[76] D. Noble, A modification of the Hodgkin-Huxley equations applicable to Purkinje fibre action and pacemaker potentials, J. Physiolology, 160 (1962) 317-352.

[77] Gerhard A Holzapfel and Ray W Ogden. Constitutive modelling of passive myocardium: a structurally based framework for material characterization. Philosophical transactions. Series A, Mathematical, physical, and engineering sciences, 367(1902):3445–75, 2009.

[78] Lafortune P et al. Coupled electromechanical model of the heart: parallel finite element formulation. International journal for numerical methods in biomedical engineering. 28 (1):72-86, 2012.

[79] T. Usyk, R. Mazhari, and A. McCulloch, Effect of laminar orthotropic myofiber architecture on regional stress and strain in the canine left ventricle, Journal of Elasticity, 61 (2000), pp. 143-164.

[80] Shi Y., Lawford P. and Hose R. (2011) Review of Zero-D and 1-D Models of Blood Flow in the Cardiovascular System, BioMedical Engineering OnLine, Vol 10, 1, p. 33. doi: 10.1186/1475-925X-10-33

[81] Formaggia L., Lamponi D. and Quarteroni A. (2003), One-dimensional models for blood flow in arteries, Journal of Engineering Mathematics, Vol. 47, Issue 3-4, pp. 251-276. https://doi.org/10.1023/B:ENGI.0000007980.01347.29

[82] Santiago A., Aguado-Sierra J., Zavala-Aké M., Doste-Beltran R., Gómez S., Arís, R., Cajas, J.C., Casoni, E. and Vázquez, M. (2018) Fully coupled fluid-electro-mechanical model of the human heart for supercomputers, Int J Numer Meth Biomed Engng, 34:e3140.

[83] Vázquez M., Houzeaux G., Koric S., Artigues A., Aguado-Sierra J., Arís R., Mira D., Calmet H., Cucchietti F., Owen H., Taha A., Dering Burness E., Cela J.M. and Valero M. (2016). Alya: Multiphysics engineering simulation toward exascale. Journal of Computational Science, Vol. 14, pp. 15-27.

[84] Alfonso Santiago. Fluid-Electro-Mechanical model of the human heart for supercomputers. 2018. PhD Thesis. Universitat Politécnica de Catalunya.

[85] Guillaume Houzeaux, R Aubry, and Mariano Vázquez. Extension of fractional step techniques for incompressible flows : The preconditioned Orthomin (1) for the pressure Schur complement. Computers and Fluids, 44(1):297–313, 2011.

[86] Yuri Bazilevs, Kenji Takizawa, and Tayfun E. Tezduyar. Computational Fluid-Structure Interaction. 2013.

[87] Pablo J Blanco, Jorge S Leiva, and Gustavo C Buscaglia. A blackbox decomposition approach for coupling heterogeneous components in hemodynamics simulations. International journal for numerical methods in biomedical engineering, 29(November 2012):408–427, 2013.

[88] Pablo J Blanco, Jorge S Leiva, Raul A. Feijóo, and Gustavo C. Buscaglia. Black-box decomposition approach for computational hemodynamics: One-dimensional models. Computer Methods in Applied Mechanics and Engineering, 200(13-16):1389–1405, mar 2011.

[89] Mathieu De Craene, Stéphanie Marchesseau, Brecht Heyde, Hang Gao, M Alessandrini, Olivier Bernard, Gemma Piella, AR Porras, Lennart Tautz, Anja Hennemuth, et al. 3d strain assessment in ultrasound (straus): A synthetic comparison of five tracking methodologies. IEEE transactions on medical imaging, 32(9):1632–1646, 2013.

[90] Thomas Fritz, Christian Wieners, Gunnar Seemann, Henning Steen, and Olaf Dossel. Simulation of the contraction of the ventricles in a human heart model including atria and pericardium: Finite element analysis of a frictionless contact problem. Biomechanics and Modeling in Mechanobiology, 13(3):627–641, 2014.

[91] Alfonso Santiago, Jazmin Aguado-Sierra, M. Zavala, Ruben Doste- Beltran, Samuel Gomez, Ruth Arís, Eva Casoni, and Mariano Vazquez. Fluid-electro-mechanical model of the human heart for supercomputers. International Journal for Numerical Methods in Biomedical Engineering (submitted), 2017.

[92] H. Dal, S. Göktepe, M. Kaliske, E. Kuhl, A fully implicit finite element method for bidomain models of cardiac electromechanics, Comput Methods Appl Mech Eng., 253 (2013) 323–336

[93] P.J. Hunter, A.D. McCulloch, H.E.D.J.t. Keurs, Modelling the mechanical properties of cardiac muscle, Progress Bioph. Molec. Biology, 69 (1998) 289-331.

[94] E. Berberoglu, H.O. Solmaz, S.Göktepe, Computational modeling of coupled cardiac electromechanics incorporating cardiac dysfunctions, Eur. J. Mech. Solids, 48 (2014) 60-73.

[95] M. Kojic, N. Filipovic, B. Stojanovic, N. Kojic, Computer Modeling in Bioengineering - Theoretical Background, Examples and Software, John Wiley and Sons, Chichester, England, 2008

[96] M. Kojic, M. Milosevic, V. Simic, V. Geroski, S. Nizzero, A. Ziemys, N. Filipovic, M. Ferrari, Smeared multiscale finite element models for mass transport and electrophysiology coupled to muscle mechanics, Computational and Mathematical Methods in Medicine, March 2019, *submitted*.

[97] Alfio Quarteroni, Toni Lassila, Simone Rossi, and Ricardo Ruiz-baier. Integrated Heart : Coupling multiscale and multiphysics models for the simulation of the cardiac function. Computational methods in applied mechanics and Engineering, 1, 2017.

[98] El-Sayed H Ibrahim, Kevin R Johnson, Alan B Miller, Jean M Shaffer, and Richard D White. Measuring aortic pulse wave velocity using highfield cardiovascular magnetic resonance: comparison of techniques. Journal of cardiovascular magnetic resonance : official journal of the Society for Cardiovascular Magnetic Resonance, 12(1):26, 2010.

[99] John Peder Escobar Kvitting, Tino Ebbers, Lars Wigström, Jan Engvall, Christian L. Olin, and Ann F. Bolger. Flow patterns in the aortic root and the aorta studied with time-resolved, 3-dimensional, phase-contrast magnetic resonance imaging: Implications for aortic valve-sparing surgery. Journal of Thoracic and Cardiovascular Surgery, 127(6):1602–1607, 2004.

[100] Michael Markl, Mary T. Draney, D. Craig Miller, Jonathan M. Levin, Eric E. Williamson, Norbert J. Pelc, David H. Liang, and Robert J. Herfkens. Time-resolved three-dimensional magnetic resonance velocity mapping of aortic flow in healthy volunteers and patients after valve-sparing aortic root replacement. Journal of Thoracic and Cardiovascular Surgery, 130(2):456–463, 2005.

[101] E. Soudah, J. Casacuberta, P. J. Gamez-Montero, J. S. Perez, M. Rodriguez-Cancio, G. Raush, C. H. Li, F. Carreras, and R. Castilla. Estimation ofWall Shear Stress Using 4D Flow Cardiovascular Mri and Computational Fluid Dynamics. Journal of Mechanics in Medicine and Biology, 17(03):1750046, 2017.

[102] Zoran Stankovic, Bradley D Allen, Julio Garcia, Kelly B Jarvis, and Michael Markl. 4D flow imaging with MRI. Cardiovascular diagnosis and therapy, 4(2):173–92, 2014.

[103] Michael Markl and Philip J Kilner. Comprehensive 4D velocity mapping of the heart and great vessels by cardiovascular magnetic resonance. Journal of Cardiovascular Magnetic Resonance, 13(1):7, 201136